# Spectropolarimetric investigations of the deep photospheric layers of solar magnetic structures

vorgelegt von
**Nilda Oklay**
aus Söke-Aydın, Türkei

Göttingen  2011

Cover figure: 2-D spectrum of Stokes $I/I_c$ (top panel) and Stokes $V/I_c$ (bottom panel). The lines used for the analysis are marked at the top of the spectrum.

*Dedicated to My Family...*
*Aileme ithaf edilmiştir...*

# Contents

# Summary

Solar surface magnetism manifests itself in a variety of structures with sizes often comparable to or even below the spatial resolution capabilities of modern telescopes (but see Lagg et al. 2010). Nevertheless, sub-resolution information about the intrinsic atmospheric structure can be obtained via indirect techniques. Since the small scale structures have magnetic origin, the usage of high spectral resolution spectropolarimetry allows us to measure the emerging polarization and spectral signatures of the magnetic components of the solar atmosphere. The observed polarization signal can be analyzed with special methods to extract the physical parameters of the atmosphere.

The main aim of this work is to investigate the temperature structure of the small scale magnetic elements and to expand our knowledge about the physics of the unresolved magnetic features of the deep photosphere. We would like to test a previously presented, spatial resolution independent technique of using Stokes $V$ line ratios as a temperature diagnostic tool (Solanki and Brigljević 1992). We also aim to extend previous results with better statistics, and compare the results of different methods (inversions, numerical simulations).

Simultaneous observations of Stokes $I$ and Stokes $V/I$ spectra of Fe I 5379.6 Å, C I 5380.3 Å, Ti II 5381.0 Å and Fe I 5383.4 Å were performed at the Istituto Ricerche Solari Locarno (IRSOL) with the Zurich Imaging Polarimeter II (ZIMPOL II, Gandorfer et al. 2004); this data set constitutes the basis of our analysis. We analyzed ratios of the observed Stokes $V$ amplitudes following the technique introduced by Solanki and Brigljević (1992). Then, we inverted the measured profiles using SPINOR (Stokes-Profile-INversion-O-Routines, Frutiger et al. 2000) to obtain the temperature stratification along the line-of-sight. The resulting Stokes $V$ amplitude values of the synthetic profiles are then compared to the measured ones. This allowed us to constrain the temperature structure of the magnetic elements down to deep photospheric layers, without suffering from limited spatial resolution. Afterwards, we computed synthetic observables of the spectral lines using snapshots computed by the MURaM code (MPS/University of Chicago Radiative MHD, Vögler 2003, Vögler and Schüssler 2003, Vögler et al. 2005). The obtained results are then compared with the results of the inversions.

This is an exploratory work using this amplitude ratio technique in combination with inversions as well as numerical simulations to demonstrate the analytic potential of the proposed method. The most important results are:

- The decrease in ratio of the Stokes $V$ amplitude of C I 5380.3 Å relative to the other

lines with increasing Stokes $V$ amplitude, i.e., increasing magnetic flux within the spatial resolution element, shows that the magnetic features in regions with little magnetic flux are on average hotter and brighter than in regions with higher flux. This confirms and extends the results of Solanki and Brigljević (1992) to a larger number of data points, at higher spatial resolution.

- Using inversion technique we quantified these qualitative results obtained from the observations. Even with rather simple approximations in the inversions, we managed to represent our observations and obtain results complementary to those from the pure line ratio technique. From the inversion results, the temperature stratification of the observed atmospheres are obtained. Magnetic contributions in regions with less magnetic flux are on average hotter and brighter than those in regions with higher flux. A factor of 2 difference in magnetic flux density implies a temperature difference of $\approx 250$ K at the continuum forming layers.

- We compared the results obtained from magnetohydrodynamic (MHD) simulations with the results obtained from the observations and from the inversions. A good agreement between the observations, inversions and MHD simulations was found in the Stokes $V$ amplitude ratios.

- Relations of temperature with amplitude ratios and temperature ratios with amplitude ratios are investigated. Linear relations are found both in the relations of temperature with amplitude ratios obtained from the iron line, and from the the titanium line. Power law relations are found for the temperature ratios and amplitude ratios in both spectral lines.

- Decreasing Stokes $V$ amplitude asymmetries are observed with increasing Stokes $V$ amplitudes, where there is no trend observed between area asymmetries and the amplitudes.

- Red-shifted, decreasing zero-crossing velocities with increasing amplitudes are observed in each spectral line, which indicates the motions are obstructed by the magnetic field strength.

- No relation is found between the Stokes $V$ asymmetries and zero-crossing velocities.

# 1 Introduction

In this chapter brief information about the Sun (Sect. 1.1), solar photosphere (Sect. 1.1.1) and the small-scale magnetic features of the photosphere (Sect. 1.1.2) are introduced. Later on the outline of the thesis is drawn (Sect. 1.2).

## 1.1 The Sun

The Sun is a normal star on the main sequence with no peculiarities. It is common, in size, in color, in effective temperature with average mass and luminosity. Comparison to the other stars is presented in the Hertzsprung-Russell (H-R) diagram (see Fig. 1.1). Yet, the Sun is the central star of our solar system and contains approximately 98% of the total mass of the solar system. It is the only star, where we can observe the surface with high spatial resolution. The Sun is a unique natural laboratory for astrophysics. We can use it in a variety of aspects to expand our knowledge about the physics of stars. Here we can develop observational instruments, techniques and physical methods, which can be applied to understand other stars. These astrophysical aspects make the Sun a very special star for us.

### 1.1.1 Solar photosphere

The solar photosphere is the deepest atmospheric layer of the Sun, around 500 km thick, with temperature decreasing from about 6000 K at its base to about 4000 K at the temperature minimum. The photosphere radiates most of the energy, which is generated in the solar interior by nuclear fusion, in the visible range. It is the layer, for which we possess the most sensitive diagnostics of temperature, velocity, and magnetic field. This is largely due to the richness of the visible solar spectrum and the relative simplicity of line-formation physics in this layer.

This layer represents the visible solar surface, and therefore has been studied since the observations of sunspots with naked eye, first mentioned in Chinese Chronicles. With the invention of the telescope by Galileo Galilei, Christoph Scheiner, Johannes Fabricius, and Thomas Harriot, regular observations of sunspots were started. Those regular observations resulted in new discoveries, like the solar rotation, the solar differential rotation (Scheiner's Rosa Ursina, published in 1630, contains evidence that the sunspot passage took a little longer at higher solar latitude than near the equator, although the interpretation in terms of a *differential rotation* of the Sun came only much later), the solar cycle (Schwabe 1844), etc.
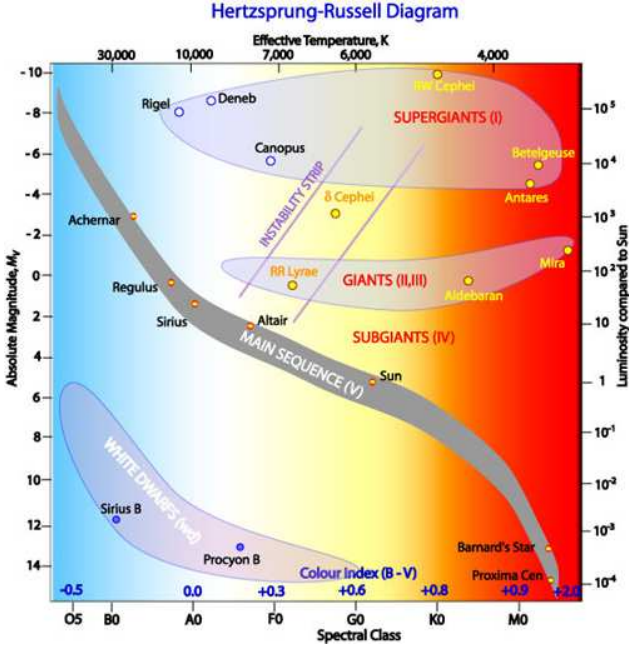
Figure 1.1: H-R Diagram (*from Australia Telescope Outreach and Education*).

Many photospheric structures at all scales have a magnetic origin, which can be observed by finding Zeeman effect induced splitting and polarization in spectral lines. The magnetic nature of sunspots was discovered by George Ellery Hale (Hale 1908). Magnetic field strengths are $1000\,G-2000\,G$ in the small-scale magnetic structures (Stenflo 1973) and $1000\,G-6000\,G$ in sunspots (Zwaan 1968, Livingston et al. 2006). With the improvement of the observational techniques, previously hidden magnetic structures became possible to study. The small scale magnetic structures (explained in Section 1.1.2) were first observed by Sheeley (1967) at the Kitt Peak National Solar Observatory. Afterwards, Stenflo (1973) measured magnetic field strengths on the order of kG in the photospheric network and in quiet regions. In the mean time modern instruments were built and new techniques were developed for the analysis of solar observations, but the small-scale magnetic structures still remained partly unresolved.

Nevertheless, information on the intrinsic atmospheric structure of even unresolved magnetic features can be obtained by an appropriate choice of diagnostics of spectropolarimetric data. Such indirect techniques were pioneered by Stenflo (1973), with the Stokes $V$ line ratio between Fe I 5250.2 Å and 5247.1 Å (see Solanki (1993) for an overview of Stokes-based diagnostic techniques) spectral lines. One quantity that is of consider-

able interest, not only for our understanding of magnetic features, but also to improve estimates of their contribution to solar irradiance variations (e.g. Unruh et al. 1999), is the thermal structure of the photosphere. This has been deduced from spectral (Chapman 1977, Walton 1987) and spectropolarimetric data (Solanki 1986, Keller et al. 1990, Zayer et al. 1990, Briand and Solanki 1995, Bellot Rubio et al. 2000). In general, these studies used spectral lines of Fe I and Fe II that are not very sensitive to the temperature in the deep photosphere near the important continuum forming layer. It was pointed out by Solanki and Brigljević (1992) that weak lines of C I provide an ideal extension to the deep layers of magnetic features (cf. Livingston et al. 1977, Elste 1987, Holweger and Müller 1974). One shortcoming of the work of Solanki and Brigljević (1992) is that it was restricted to two regions, so that is not clear how general the results of that study were. Another is that Solanki and Brigljević (1992) did not employ an inversion technique to extract information from the line profiles, but simply varied the temperature structure in an ad hoc manner.

With the present study we not only remove those shortcomings, but also extend that study in other ways. Thus we analyze data from a far larger number of solar surface locations than just the 2 studied by Solanki and Brigljević (1992). In addition, we also compare our data with synthetic profiles obtained from state-of-the-art numerical simulations. Here we use spectropolarimetric observations in the photospheric lines C I 5380.3 Å, Fe I 5379.6 Å, Ti II 5381.0 Å, and Fe I 5383.4 Å. This set of lines covers the atmospheric layers from the deep to the mid-photosphere. The weak C I line with a high-excitation potential is well suited to improve the determination of the temperature near the continuum forming layers of the magnetic elements.

### 1.1.2 Small-scale magnetic features of the solar photosphere

Outside active regions containing sunspots, the photospheric magnetic field is concentrated in pores, micropores and in plage regions. The small-scale magnetic features are formed mostly in the intra-network and inter-granular lanes. They can also be found in the intra-network of the quiet sun regions (Lites 2002), but with less number density. The resolved small-scale structures are mostly named according to their appearance as ribbons, flowers, etc. but the common denominator of all these features is their theoretical description as flux tubes. The concept of flux-tubes was theoretically explained by Spruit (1976, 1979).

The basic explanation of each magnetic feature is an isolated magnetic flux tube. 90% or more of the network magnetic field is in form of magnetic flux tubes with a field strength of the order of kG (Howard and Stenflo 1972, Frazier and Stenflo 1972) and typically a diameter of 100 km. They penetrate the surface in a roughly vertical direction with rapid expansion with height. Fig. 1.2 describes the magnetostatic fluxtube where the magnetic pressure causes a reduction of the gas pressure inside the tube to balance the outside gas pressure at all heights. The expansion of the tube with height is due to the exponential drop-off of the outside pressure. The lower gas pressure leads to a partial evacuation of the flux-tube atmosphere, which leads to a depressed iso-surface of the continuum optical depth in its inside. The relatively transparent flux-tube interior allows us to see deeper layers, leading to the Wilson depression of 200 km for pores of 1000 km
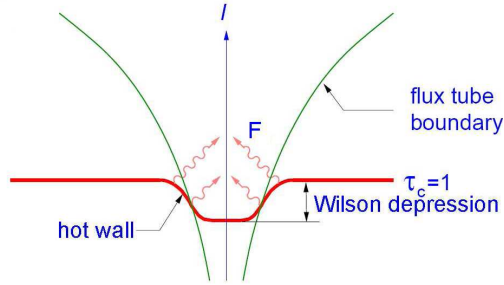
Figure 1.2: Schematic representation of a fluxtube *(modified from Steiner 2007)*.

diameter and 100-200 km for facular points (Spruit 1976). In Fig. 1.2, the wavy arrows represent sideways radiation by the walls which are hotter than the internal gas at certain heights due to a deficit in convective energy flux inside the flux-tube (vertical arrows). The first explanation of the "hot-wall" effect is presented by Spruit (1976). The hot walls excessively radiate into the flux tube (Spruit 1976), which causes the flux-tube atmosphere to be heated through radiative influx by $\delta T \approx 300\,K$ with respect to the surroundings at equal geometrical height (Steiner and Stenflo 1990). The standard models of flux-tube atmospheres were introduced by Solanki and Stenflo (1985), Solanki (1986), Solanki and Brigljević (1992). They provide the stratification of the physical parameters of the flux-tube atmosphere derived from spectral line profiles, especially from the Stokes $V$ profiles of Fe I lines.

These small scale magnetic structures play an important role in our understanding of solar magnetic fields and in the total brightness variations of the Sun, which have been found to correlate with the solar activity cycle (Willson and Hudson 1991). The total irradiance is on average 0.1% higher during activity maximum where there are more sunspots on the solar disk (Fröhlich 2000). The dark sunspots contribute to the darkening of the Sun, while small scale structures contribute to the brightening (Solanki and Unruh 1998). Over 90% of the net magnetic flux is concentrated in small flux tubes (Howard and Stenflo 1972, Frazier and Stenflo 1972). Even though the small scale kG structures occupy only a small fraction of the solar surface, they provide a significant part of the magnetic energy (Domínguez Cerdeña et al. 2006). The small scale magnetic elements probably affect the behavior of the global magnetic fields by their influence on the solar dynamo (Schüssler 1983, Schüssler 1992).

Additionally, solar magnetic elements have a significant influence on the bright structures and dynamical processes of the chromosphere and corona (Narain and Ulmschneider 1996). Indeed, they are the most likely channels for transporting the energy required to heat these layers (Spruit and Roberts 1983, Ulmschneider and Musielak 2003).

# 1.2   Outline of the thesis

This thesis mainly elaborates and uses a technique, which gives information about the temperature structure of the small scale magnetic features, independently of the spatial resolution. The outline of the thesis is as follows:

- The underlying data set consists of simultaneously recorded Stokes $I$ and Stokes $V/I$ profiles of C I 5380.3 Å, Fe I 5379.6 Å, Ti II 5381.0 Å and Fe I 5383.4 Å lines from an active region; it was obtained with ZIMPOL II at IRSOL. These lines are carefully selected to cover not only mid-photospheric but also deep photospheric layers. The observations and data reduction steps are explained in Chapter 3.

- The data are analyzed using different techniques: Techniques based on Stokes parameters. The investigated Stokes parameters are Stokes $V$ asymmetries, Stokes $V$ ratios, velocities calculated from Stokes $I$ and Stokes $V$, relation between zero crossing wavelength and Stokes $V$ asymmetries. Inversions are performed to obtain physical parameters of the atmosphere. The details of both methods and the results are presented in Chapter 4.

- Some snapshots resulting from realistic MHD simulations calculated with the MU-RaM code (MPS/University of Chicago Radiative MHD, Vögler 2003, Vögler and Schüssler 2003, Vögler et al. 2005) are investigated. We computed synthetic observables of the spectral lines. Stokes $V$ line ratios are investigated. The analysis of the synthetic data, and the comparison of the results with the observations and inversions are presented in Chapter 5.

# 2   Introduction to spectropolarimetry

Spectropolarimetry is a very powerful technique, which allows us to obtain information about magnetic structures of the sun. Therefore this technique represents the only way to retrieve information about the spatially unresolved magnetic structures of the solar atmosphere. The basic principles of spectropolarimetry are explained in this chapter introducing the Zeeman effect, polarized light, the Stokes parameters and the radiative transfer equation for polarized light.

Light can be polarized by reflection, refraction, dichroism, scattering, and magnetic fields. In this thesis, we concentrate on the light polarized by the existence of a magnetic field. We can get information about magnetism from Zeeman splitting of spectral lines, and the observation of the Zeeman pattern of spectral lines is done with spectropolarimetry.

## 2.1   Zeeman effect

In 1896 Pieter Zeeman discovered that in the presence of the magnetic field, spectral lines split into polarized components. Zeeman splitting of spectral lines in sunspots was first reported by Hale (1908) and this splitting provides information about the magnetic fields on the Sun.

In the case of a weak field, we apply the approximation of Russel-Saunders or LS coupling approximation introduced by Russell and Saunders (1925); $L, S, J$ and $M$ are the quantum numbers which define the state of an atom. Here, $L$ gives total orbital angular momentum of the electrons, $S$ the total spin angular momentum and, $J$ the total angular momentum ($|L - S| \leq J \leq |L + S|$) and M is the magnetic quantum number ($-J \leq M \leq J$). For a given $L$ and $S$, there are $(2L + 1) \times (2S + 1)$ possible states and the state of an atom is written as $^{2S+1}L_J$.

In the absence of a magnetic field, all M states are degenerated. In the case of a weak magnetic field (changes in energy are small as compared to the energy difference between different levels), the increment of energy is given by,

$$\Delta E = \frac{ehB}{4\pi m_e c} gM ,$$
(2.1)

where $e$ is the electron charge, $m_e$ is the electron mass, $c$ is the speed of light, $h$ is the Planck constant, $B$ is the magnetic field strength, $g$ is the Landé factor, $M$ is the magnetic quantum number, and $E$ is the energy of the state. The Landé factor is defined as,

$$g \equiv \frac{3}{2} + \frac{S(S+1) - L(L+1)}{2J(J+1)} \; , \tag{2.2}$$

where $S$ is the total spin angular momentum, $L$ is the total orbital angular momentum, and $J$ is the total angular momentum.

The Zeeman displacement of the spectral line from its original position $\lambda_0$ is

$$\Delta\lambda = \frac{eB\lambda_0^2}{4\pi m_e c^2} \, g^* \; , \tag{2.3}$$

where $g^*$ is the g factor for the transition ($g_{\text{lower}} M_{\text{lower}} - g_{\text{upper}} M_{\text{upper}}$).

Allowed (electric dipole) transitions are those with $\Delta L = 0, \pm 1$, $\Delta S = 0$, $\Delta J = 0, \pm 1$ and $\Delta M = 0, \pm 1$. The result is the Zeeman splitting. It consist of $\sigma$ and $\pi$ components.

- $\Delta M = 0 \rightarrow \pi$ component (linearly polarized)

- $\Delta M = +1 \rightarrow \sigma_{\text{blue}}$ (circularly polarized)

- $\Delta M = -1 \rightarrow \sigma_{\text{red}}$ (circularly polarized)

**Longitudinal Zeeman effect:** When the magnetic field is parallel to the line of sight. The observer is just able to see the $\sigma$ components, which are circularly polarized (Fig. 2.1).
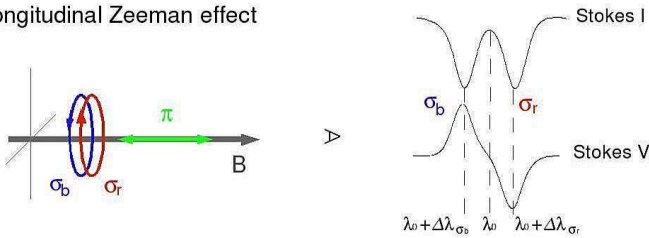


Figure 2.1: Schematic representation of the longitudinal Zeeman effect in absorption. $\sigma_b$ represents the circularly polarized blue component of a normal Zeeman triplet, while $\sigma_r$ represents the circularly polarized red component.

**Transverse Zeeman effect:** When the magnetic field is perpendicular to the line of sight, the observer can see both the $\pi$ component and the $\sigma$ components in absorption (Fig. 2.2).
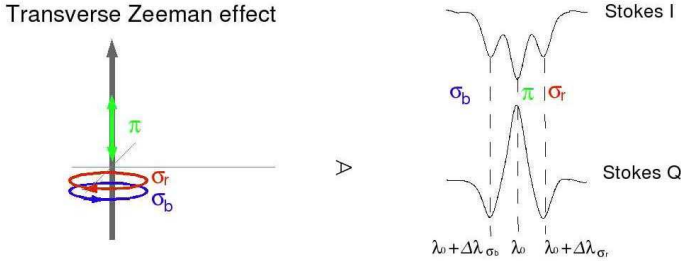


Figure 2.2: Schematic representation of the transverse Zeeman effect. $\pi$ represents linearly polarized light, $\sigma_b$ represents the circularly polarized blue component of a normal Zeeman triplet, while $\sigma_r$ represents the circularly polarized red component.

Since we aim to observe small scale magnetic structures at the disk center on the Sun, in this thesis we concentrate on the longitudinal Zeeman effect. Because at the disk center magnetic structures are assumed, to first order, to be vertical and therefore the magnetic field is parallel to the line-of-sight.

## 2.2 Polarized light and Stokes parameters

Polarized light was discovered with double refraction by Erasmus Bartholinus in 1669. Later on in 1690, Christian Huygens discovered polarization of light with the aid of two calcite crystals arranged in series. In the following, our understanding about polarized light was broadened, and optical devices for the observation of polarized light were developed.

Light can be described as a transverse wave with an electric and magnetic field, oscillating in planes perpendicular to each other and to the propagation direction. The Stokes parameters are a set of values that describe the polarization state of electromagnetic radiation. The mathematical formulation of these parameters was developed by George Gabriel Stokes in 1852. This representation has the advantage that the parameters are directly measurable, all have the same physical dimensions, shows all the states of the polarized light, and allow the radiative transfer equation to be written in a straightforward manner.

| | |
|---|---|
| **Stokes I:** | Intensity |
| **Stokes Q:** | Intensity difference between vertical and horizontal linear polarization |
| **Stokes U:** | Intensity difference between linear polarization at $\pm\,45°$ |
| **Stokes V:** | Intensity difference between right and left handed circular polarization |

In a plane perpendicular to the propagation direction, the tip of the electric vector ($E$) moves along an ellipse, whose components, with respect to the orthogonal axis $O_x$ and $O_y$, are:

$$E_x = A_x \cos(\omega t - kz)$$
$$E_y = A_y \cos(\omega t - kz + \phi)$$

where $A_x$ and $A_y$ are the amplitudes, $\phi$ is the phase difference between the electric field components.

From the transformation of these formulas Stokes parameters can be defined by:

$$I = A_x^2 + A_y^2$$
$$Q = A_x^2 - A_y^2$$
$$U = 2A_x A_y \cos(\phi)$$
$$V = 2A_x A_y \sin(\phi)$$

This is valid for monochromatic light but natural light is never perfectly monochromatic and fully polarized. Therefore if we consider light as superposition of wave packets, Stokes parameters are defined as the averages of these wave packets:

$$I = < A_x^2 + A_y^2 >$$
$$Q = < A_x^2 - A_y^2 >$$
$$U = 2 < A_x A_y \cos(\phi) >$$
$$V = 2 < A_x A_y \sin(\phi) >$$

For totally polarized light: $I^2 = Q^2 + U^2 + V^2$ while $I = 1$ and $Q = U = V = 0$ for unpolarized light. Since the light is only partially polarized and the unpolarized component is exist, degree of polarization is defined as:

$$P = \sqrt{\frac{Q^2 + U^2 + V^2}{I^2}} \ .$$

## 2.3 Radiative transfer equation for polarized light

Radiative transfer equation describes the transmission of the polarized light through the atmosphere, where the magnetic field exists, with taking into account the modification of the polarization state of light by the magnetic field.

The solution of the radiative transfer equation in the presence of a magnetic field was introduced by Unno (1956) and extended by Rachkovsky (1962) (named as Unno-Rachkovsky radiative transfer equations). Detailed information about the definition and solution of RTE can be find in del Toro Iniesta (2003). Here first we define the system of coordinates as shown in Fig. 2.3. The line of sight is oriented along the z axis.

The radiative transfer equation (RTE) for polarized light can be written as:

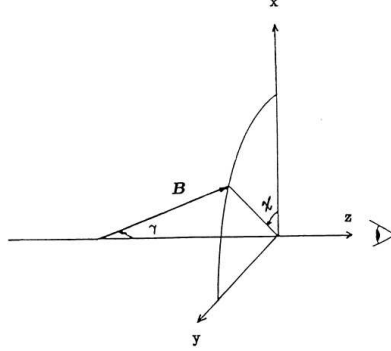$$\frac{d\mathbf{I}}{ds} = -\mathbf{KI} + \mathbf{j} \ , \tag{2.4}$$

Figure 2.3: Reference frame. The z-axis corresponds to the line of sight. $\gamma$ is the angle between $B$ and line-of-sight, where $\chi$ is azimuthal angle of $B$ *(from Solanki 1993)*.

where **I** is the Stokes vector [**I**=(I,Q,U,V)], s is height in the atmosphere, **K** is the total absorption matrix,

$$\mathbf{K} = \kappa_c \mathbf{1} + \kappa_0 \boldsymbol{\eta} \,, \tag{2.5}$$

and **j** is the total emission vector:

$$\mathbf{j} = \kappa_c S_c \boldsymbol{e}_0 + \kappa_0 S_L \boldsymbol{\eta} \boldsymbol{e}_0 \,. \tag{2.6}$$

Here **1** is the unit $4 \times 4$ matrix, $\boldsymbol{e}_0 = (1, 0, 0, 0)^T$, $\kappa_c$ is continuum absorption coefficient, $\kappa_0$ is the line center opacity, $S_c$ is the source function and $S_L$ is line source function. With LTE assumption the source function is equal to the Planck function at local temperature i.e. $S_c = B_\lambda(T_e)$ and $S_L$ depends only on the total populations of the upper and lower levels of the transition. Therefore, under the LTE assumption, $S_c = S_L$.

The line absorption matrix (propagation matrix) $\boldsymbol{\eta}$ is

$$\boldsymbol{\eta} = \begin{bmatrix} \eta_I & \eta_Q & \eta_U & \eta_V \\ \eta_Q & \eta_I & \rho_V & -\rho_U \\ \eta_U & -\rho_V & \eta_I & \rho_Q \\ \eta_V & \rho_U & -\rho_Q & \eta_I \end{bmatrix}, \tag{2.7}$$

where

$$\eta_I = \frac{1}{2}[\eta_p \sin^2 \gamma + \frac{1}{2}(\eta_b + \eta_r)(1 + \cos^2 \gamma)] \tag{2.8}$$

$$\eta_Q = \frac{1}{2}[\eta_p - \frac{1}{2}(\eta_b + \eta_r)] \sin^2 \gamma \cos 2\chi \tag{2.9}$$

$$\eta_U = \frac{1}{2}[\eta_p - \frac{1}{2}(\eta_b + \eta_r)] \sin^2 \gamma \sin 2\chi \tag{2.10}$$

$$\eta_V = \frac{1}{2}[\eta_b - \eta_r] \cos \gamma \tag{2.11}$$

19

and

$$\rho_Q = \frac{1}{2}[\rho_p - \frac{1}{2}(\rho_b + \rho_r)]\sin^2\gamma\cos 2\chi \qquad (2.12)$$

$$\rho_U = \frac{1}{2}[\rho_p - \frac{1}{2}(\rho_b + \rho_r)]\sin^2\gamma\sin 2\chi \qquad (2.13)$$

$$\rho_V = \frac{1}{2}[\rho_b - \rho_r]\cos\gamma \qquad (2.14)$$

Here $p$ represents the unshifted, $b$ represents the blue shifted and $r$ represents the red shifted components. Angles $\chi$ and $\gamma$ represent the direction of the magnetic field with respect to line-of-sight (Fig. 2.3). For different polarization states of the radiation field, $\eta_{I,Q,U,V}$ define the absorbing properties of the atmosphere, while $\rho_{Q,U,V}$ describe the coupling of the Stokes parameters due to anomalous dispersion effects. The Zeeman splitting manifests itself in the strengths and shifts of the $\eta_{p,b,r}$ and $\rho_{p,b,r}$ (magneto-optical effects) values.

The general absorption profiles $\eta_k$ and anomalous dispersion profiles $\rho_k$ are:

$$\eta_k = \eta_0 \sum_M S_M{}^k H(a, v + v_M{}^k + v_D) \qquad (2.15)$$

$$\rho_k = \eta_0 \sum_M S_M{}^k 2F(a, v + v_M{}^k + v_D) , \qquad (2.16)$$

where $k = p, b, r$, $S_M{}^k$ is the Zeeman strength, $\eta_0$ is line-to-continuum absorption coefficient ratio, $H$ is Voigt function, $F$ is Faraday function for a given abundance $a$, and at a given distance from the line center $v$, with taken into account the wavelength shifts due to macroscopic velocity in the direction of line-of-sight $v_D$ and shifts due to Zeeman splitting $v_M{}^k$.

# 3 Spectropolarimetry of the solar photosphere

In this chapter, the spectropolarimetric observations (Sect. 3.1) and the associated data reduction (Sect. 3.2) steps are presented. First, spectropolarimetric observations of the selected spectral lines are explained in detail with an introduction about the ZIMPOL II instrument (Sect. 3.1.1) at IRSOL. At the end, detailed data reduction (both polarimetric (Sect. 3.2.2) and CCD (Sect. 3.2.1)) steps are presented.

## 3.1 Instrumentation and observations

Simultaneous observations of Stokes $I$, Stokes $Q/I$ and Stokes $V/I$ spectra of C I 5380.3 Å, Fe I 5379.6 Å, Ti II 5381.0 Å and Fe I 5383.4 Å were performed at the Istituto Ricerche Solari Locarno (IRSOL, Table.3.1) on June $3^{rd}$ 2007 at around 15:00 UT with the 45 cm diameter (f=25 m) Gregory Coudé Telescope. The Zurich Imaging Polarimeter II (ZIMPOL II, Gandorfer et al. 2004) was used in combination with the Czerny-Turner spectrograph, which has a grating of 360 lines/mm (f=10 m). In order to avoid spectral overlap from other orders, a 1m Littrow predisperser is used in front of the spectrograph. A focal reducer is used to match the angular resolution to the pixel sampling on the detector. The spectrograph order was $10^{th}$ in the observational setup. Technical information about the observations is presented in Table 3.2. A sketch of the instrumentation and the polarization analysis system are presented in Fig. 3.1 and in Fig. 3.2, respectively.

Table 3.1: IRSOL

| Parameter | Value |
|---|---|
| Latitude | 46 ° 10 ′ 40 ".6 N |
| Longitude | 8 ° 47 ′ 22 ".9 E |
| Elevation | 506 m |
| Local Time | GMT$^{\star}$+1$^h$ |

[$\star$]*Greenwich Mean Time*

Polarized spectra were obtained with an exposure time of 0.5 s with 20 integrations at 5 different positions, marked in Fig. 3.3 [1], within active region (NOAA 10958) near solar disk center ($\mu \equiv \cos(\theta) = 0.95$, where $\theta$ denotes the heliocentric angle) avoiding both,

---

[1] (magnetogram from the Michelson Doppler Imager (MDI) on the Solar and Heliospheric Observatory (SOHO), Scherrer et al. 1995)

Table 3.2: Observations

| Parameter | Value |
|---|---|
| Reduction Optics | 3:2 |
| Spectrograph Order | $10^{th}$ |
| Slit Width | 50 micrometer |
| Slit Angle[*] | $12\,°.642$ |
| Spectral Sampling | 6.324 mÅ/px |
| Spatial Scale | 1".3/px |
| Polarimetric Sensitivity | $1.3 \times 10^{-3}$ of the continuum intensity[†] |

[*]*Angle between slit orientation and heliographic E-W.*
[†]*Under observing conditions.*

Table 3.3: Observed spectral lines

| Element | $\lambda_0$ (Å) | Transition | $\chi_{ex}$ (eV) | $\chi_{ion}$ (eV) | $\log(gf)$ | $g_{eff}$ |
|---|---|---|---|---|---|---|
| Fe I | 5379.574 | $b^1G_4 - z^1H_5^0$ | 3.69 | 7.87 | -1.480 | 1.096 |
| C I | 5380.323 | $s^1P_1^0 - p^1P_1$ | 7.68 | 11.26 | -1.616 | 1.0 |
| Ti II | 5381.015 | $b^2D_{3/2} - z^2F_{5/2}^0$ | 1.80 | 13.58 | -2.080 | 0.922 |
| Fe I | 5383.369 | $z^5G_5^0 - e^5H_6$ | 4.31 | 7.87 | 0.48 | 1.123 |

sunspot and pores. Typical noise levels are $1.8 \times 10^{-3}$ of the intensity, the spatial scale is 1".3/px, the spectral sampling is 6.3 mÅ/px, and the slit covers 182 " on the solar disk.

Characteristics of the observed spectral lines are presented in Table 3.3. Here, $\lambda_0$ denotes the central wavelength, $\chi_{ex}$ is the excitation potential, $\chi_{ion}$ the ionization potential of the relevant ion, $\log(gf)$ is the logarithmic, statistically weighted oscillator strength, $g_{eff}$ is the Landé factor. Atomic data are taken from NIST[2] (Ralchenko et al. 2008). Since the Carbon line has a high excitation potential we know that it gives access to continuum forming layers (see Sect. 4.3.1). Therefore, this set of spectral lines probes not only the mid-photosphere but also the deep photosphere.

Only simultaneously recorded Stokes $I$ and Stokes $V/I$ signals are analyzed and an example of an observed spectrum is presented in Fig. 3.4. The spectral lines used for the analysis are indicated by arrows. The reason not to use Stokes $Q/I$ measurements is that the flux tubes are oriented predominantly vertically to the surface (Schüssler 1986); when we observe near the disk center the magnetic field is close to parallel to the line of sight.

Polarimetric calibrations are necessary to obtain efficiencies for both, linear and circular polarizations. For these reasons, during the observations the polarimetric calibrations are done every half an hour, additionally dark current and flat field images are taken for the CCD reduction, with the same conditions as the observations.

100 flat field images are taken with smearing the solar disk center image by moving the telescope pointing during exposure, avoiding sunspots or pores and averaged. 10 dark images are taken with the shutter, which is integrated into the calibration box, and averaged. Both, flat field and dark current images, have the same exposure time as the observations.

---

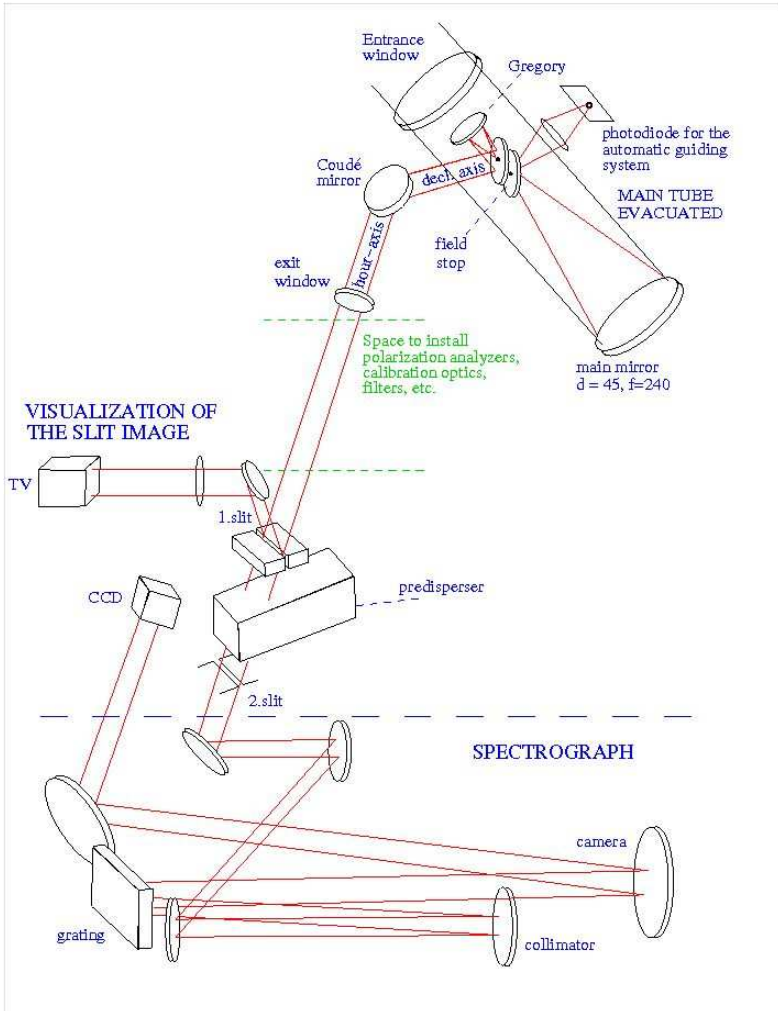[2]National Institute of Standards and Technology

Figure 3.1: Instrumentation

In order to determine the polarimetric efficiency of the instrument, polarimetric cal-ibrations are done in front of the polarimetric analysis system, with a combination of a linear polarizer and a quarter-wave retardation plate (Gandorfer et al. 2004, Gisler 2005).
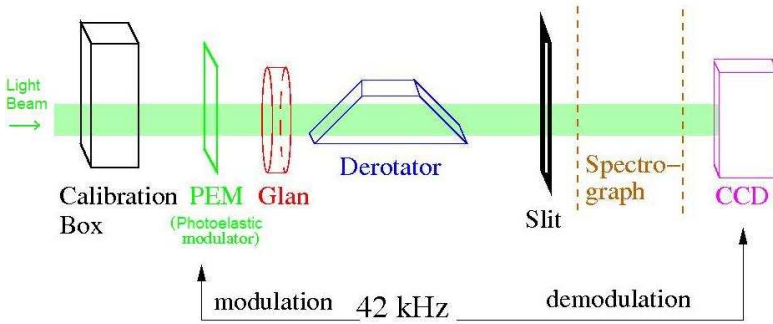
Figure 3.2: Polarization analysis system .
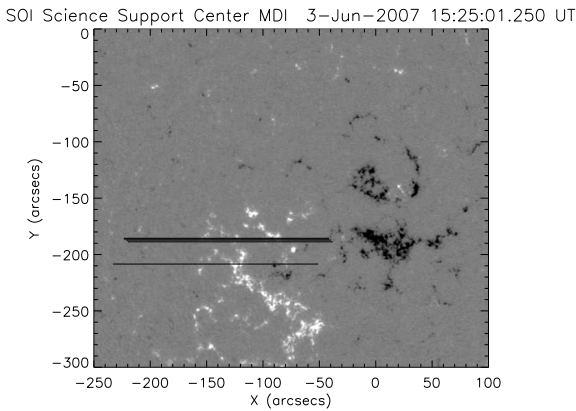


Figure 3.3: SOHO/MDI magnetogram of the observed active region NOAA 10958. Coordinates (0,0) indicate the center of the solar disk. Black lines represent the slit positions.

### 3.1.1   ZIMPOL II

ZIMPOL II is a unique instrument with fast modulation/demodulation for full Stokes recordings. The polarization of the incoming light is modulated in the kHz range by a photoelastic modulator (PEM) and subsequently converted into an intensity modulation by a Glan linear polarizer acting as analyzer. ZIMPOL II CCD is designed such that three of every four pixel rows are masked, which means they are not illuminated at any time.
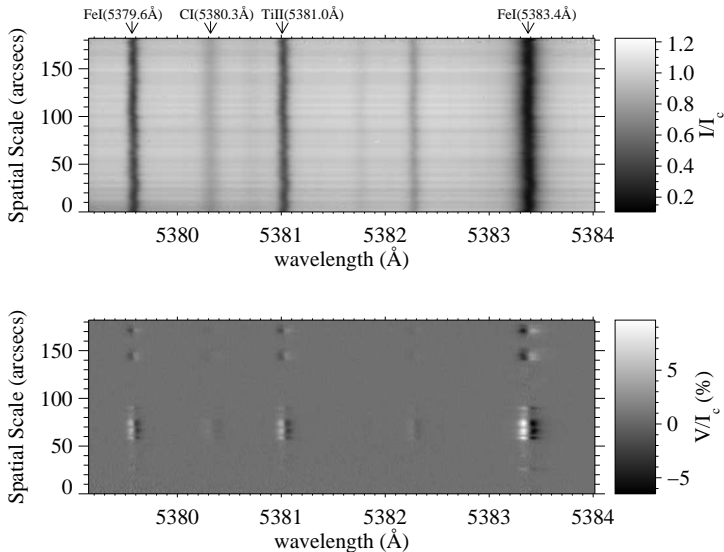
Figure 3.4: 2-D spectrum of Stokes $I/I_c$ (top panel) and Stokes $V/I_c$ (bottom panel). The lines used for the analysis are marked at the top of the spectrum.

Each illuminated pixel accumulates signal during a given modulation state and the charge package is then vertically shifted to the masked pixel synchronously to the modulation, without reading the chip (Fig. 3.5). If the modulation pattern is selected appropriately, the 4 Stokes parameters can be recorded simultaneously with a single CCD (Stenflo et al. 1992). Additionally, the ZIMPOL demodulation principle has the advantage that the fractional polarization images are absolutely free from gain table or flat field effects (Povel 1995, Gandorfer and Povel 1997).

## 3.2   Data reduction

The observed spectra are subject to effects introduced by the instrumentation and by the Earth's atmosphere. Therefore, for each observation, polarimetric calibrations, dark current, and flat field observations are performed to calibrate for these effects. In this section not only the basic polarimetric calibration and CCD reduction is explained, but also straylight, instrumental polarization and, an estimation of the seeing effects are discussed. The wavelength calibration and noise level determination are explained, and calculations of both spatial and spectral sampling are presented.

The data reduction is done with the *Interactive Data Language* (IDL) program. IR-SOL has its own ZIMPOL II IDL library for the polarimetric calibration and numerous useful tools to treat the data (Gisler 2005). Further calculations are done with self written
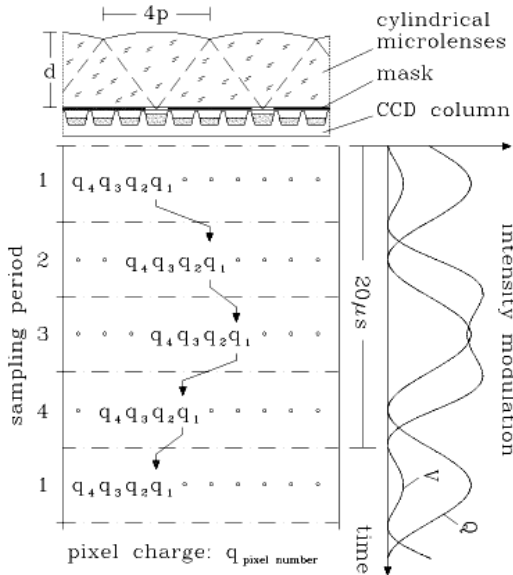
Figure 3.5: Principle of the demodulation scheme. Upper part: Cross section of the microlens array in a plane perpendicular to the pixel rows (this part will be removed from the image). The vertical scale is compressed. 4p is typically $90\,\mu$m (p is pixel size), d is on the order of 1 mm. Right part: Intensity modulation for Stokes $Q$ and $V$. The modulation period is $20\,\mu$s (corresponding to 50 kHz). Central part: Position of the charge packages during the four sampling periods. *This figure is taken from Gandorfer and Povel (1997).*

IDL procedures.

### 3.2.1   CCD images

In Fig. 3.6 we see an example raw spectra of Stokes $I$ (top panel) and Stokes $V/I$ (bottom panel). In the intensity image we see dark patches, bad pixels and inhomogeneous illuminated image. All CCD images need to be calibrated for bias, dark signal and gain table (flat field). Bias denotes here the zero level of the analog read-out chain, while dark current is caused by phonon-generated electrons. Flat field is the pattern of the individual photosensitivity of the CCD pixels.

In the calibration both, bias and dark current constitute the "dark frame". While the bias is common to all pixels, thermally induced charges are individual to every pixel; the dark frame is therefore subtracted pixel by pixel from the measurement frames. An example of flat-field and dark frame is presented on the top and bottom panels of Fig. 3.7 respectively.

CCD image corrections contain also the removal of "hot pixels". ZIMPOL II reduction
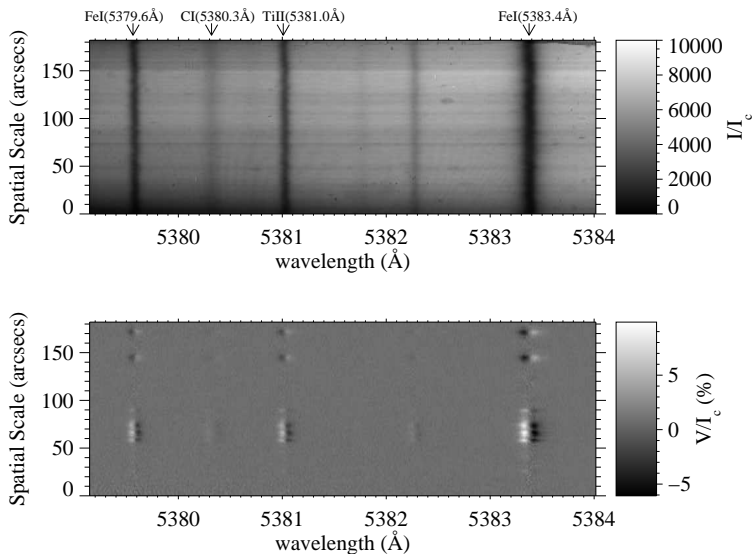
Figure 3.6: Raw spectra of Stokes *I* (top panel) and Stokes *V/I* (bottom panel).

routines have the option for a $3 \times 3$px median filter, and this option is used to remove hot pixels.

The normal CCD reduction procedure is:

$$\text{Reduced Data} = \frac{\text{Observed Data} - \text{Dark Frame Image}}{\text{Flat Field} - \text{Dark Frame Image}} . \qquad (3.1)$$

Reduced image is presented in Fig. 3.8.

The ZIMPOL II reduction routines deal with dark current corrections. Therefore, we only had to deal with flat-fielding of the observations.

The fractional polarization values obtained with ZIMPOL II are free from flat field effects. Therefore there is no need for flat-fielding of the polarization measurements. However, it is not true for Stokes *I* images. Therefore Stokes *I* images have to be divided by flat-field images.

The extraction of the flat-field was done with a flat fielding procedure, following Zakharov (2006). This routine deals with extraction of the flat field image, the spectral transmission curve, and the wavelength calibration.

To be able to use this reduction routine, the observed spectral range is extracted from the Fourier Transform Spectrometer (FTS) atlas (Brault and Neckel 1987). Wave numbers are converted to wavelengths, and the linear dispersion values of the first and the last spectral line of the observed spectrum are calculated according to the formula for the
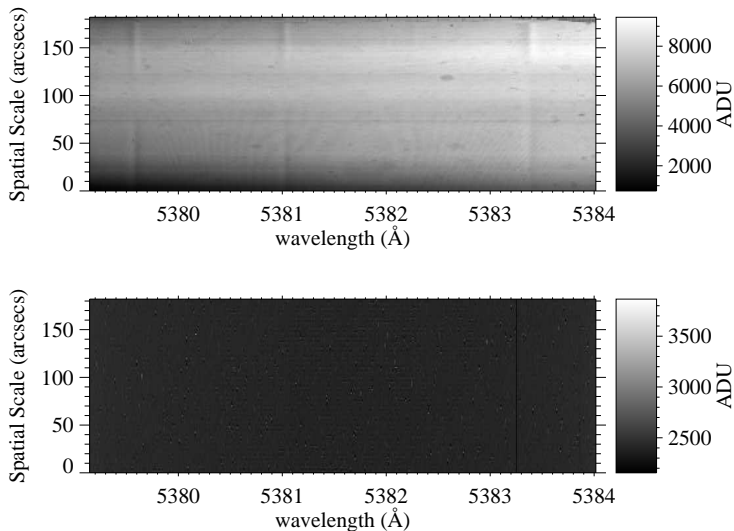
Figure 3.7: Flat-field (top panel) and dark frame (bottom panel) images.

linear dispersion:

$$\frac{dx}{d\lambda} = f_s \frac{d\beta}{d\lambda} \; , \tag{3.2}$$

where $f_s$ is the focal length and $d\beta/d\lambda$ is the angular dispersion given by

$$\frac{d\beta}{d\lambda} = \frac{m}{a\cos\beta} \; , \tag{3.3}$$

where $\beta$ is the blaze angle, $m$ is the spectrograph order, and $a$ is the grating constant in of grooves per mm. With this, the linear dispersion in the spectral plane is defined as:

$$\frac{dx}{d\lambda} = f_s \frac{d\beta}{d\lambda} = f_s \frac{m}{a\cos\beta} \; . \tag{3.4}$$

The linear dispersion at the position of Fe I (5379.5 Å) line is 5.0782 mm/Å and 5.0870 mm/Å at the Fe I (5383.4 Å).

The reduction procedure can be summarized as:

1. Compressing the flat field image in the spatial direction to create a 1-dimensional reference spectrum.

2. Obtaining the gain table of the CCD.
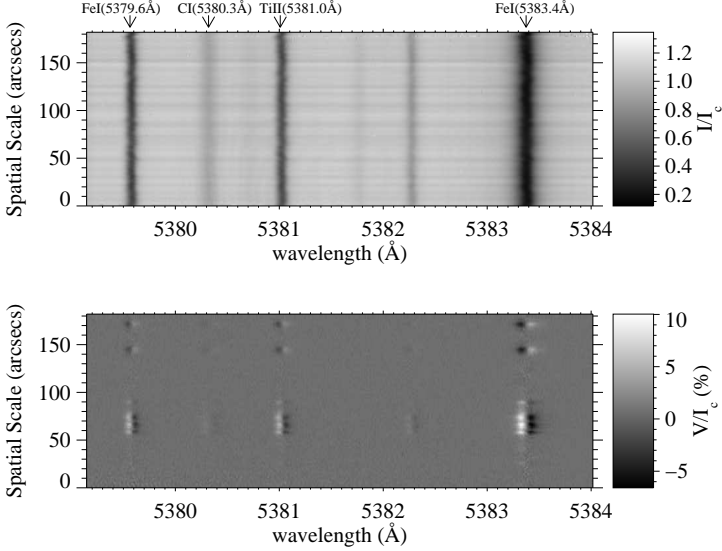
Figure 3.8: Fully reduced, flat-fielded spectra of Stokes $I/I_c$ (top panel) and Stokes $V/I_c$ (bottom panel).

3. Determining the spectral transmission curve.

4. Wavelength calibration.

The flat field image is compressed in the spatial direction in order to obtain a reference 1-dimensional spectrum. The spectra of all positions along the slit were co-aligned to the reference by cross-correlation and divided by it to obtain the CCD gain table. To linearize the linear dispersion, the observed data have been linearly interpolated between calculated values of linear dispersion (5.0782 mm/Å and 5.0870 mm/Å) on the whole observed spectral region and the spectra were destretched accordingly. The prefilter curve is calculated by dividing the 1-dimensional reference spectrum by the FTS intensity at these wavelengths and then second degree polynomially interpolated on the whole observed spectral domain.

A comparison of our mean flat-field profile with the FTS spectrum, which is assumed to be free of spectrally scattered light, enables us to estimate the scattered light in the data:

$$I_\lambda^{\text{observed}} = I_\lambda^{\text{FTS}} \otimes d_{\text{IRSOL}} + I_{\text{scatter}} , \qquad (3.5)$$

where $I_\lambda^{\text{observed}}$ is the observed intensity, $I_\lambda^{\text{FTS}}$ is the intensity from the FTS atlas, $d_{\text{IRSOL}}$ is the instrumental profile, and $I_{\text{scatter}}$ is the spectral scattered light. Here '$\otimes$' denotes convolution.

Figure 3.9: Wavelength calibration fit. The reference spectrum is presented in black, while the FTS spectrum is presented in red.
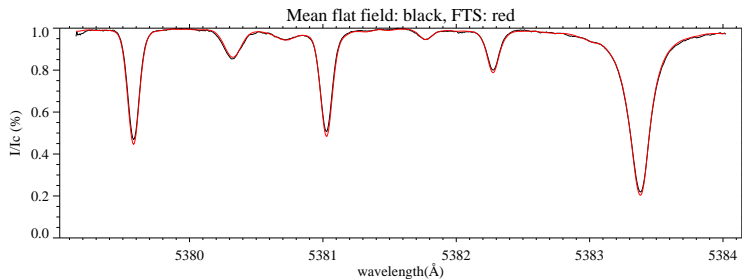
3% of stray-light is calculated, and the instrument profile is a Gaussian with a FWHM of 63 mÅ.

By varying the FTS spectral smearing by convolving with a Gaussian function and varying $I_{scatter}$ the optimum combination of these quantities was found, which showed the best coincidence with the observed 1-dimensional reference spectrum. From the correlation of the FTS and the mean observed spectrum the wavelength scale is produced. Therefore the spectral sampling determined 6.3 mÅ/px. Wavelength calibration is done with the FTS atlas because it is corrected for the Earth's rotation, Earth's orbital motion, and the solar rotation. We thus get rid of all the corrections during the wavelength calibration without extra calculation (Fig. 3.9). To compute the spectral transmission curve, continuum parts of the mean profile are selected. The filter curve is calculated by dividing the 1-D reference spectrum by the FTS intensity at these wavelengths and polynomial interpolation on the whole observed spectral range.

## 3.2.2   Polarization calibration

The efficiencies for linear and circular polarization were calibrated by inserting a combination of a Glan linear polarizer and an achromatic quarter-wave plate into the light beam before the polarization analysis system. The details about the polarimetric calibration can be found in Gandorfer et al. (2004), Gisler (2005).

## 3.2.3   Instrumental polarization

The polarization of the continuum should be zero at disk center. Any non-zero polarization signal arises from the telescope itself. The main effect of the instrumental polarization can be seen in the Stokes $V/I$ signal as an offset, which is $I \rightarrow V$ cross-talk. This value is typically 0.7% for our observations.

$$V_{obs} = V + k \times I_{obs} \,, \tag{3.6}$$

where $I_{obs}$ is the observed intensity, $V_{obs}$ is the observed Stokes $V$ signal, $V$ is the real Stokes $V$ signal and $k$ is the offset value (fraction of intensity).

In our observation Stokes $I$, $Q$, $V$ signals are recorded simultaneously. The Stokes $V/I$ signal is affected via Stokes $Q/I$ to $V/I$ crosstalk. Crosstalk calibration coefficients are obtained from IRSOL (R. Ramelli, private communication) and $Q \rightarrow V$ crosstalk is corrected according to:

$$\left(\frac{V}{I}\right)_{\text{corrected}} = \frac{V}{I} + 0.179 \times \frac{Q}{I} \; . \tag{3.7}$$

Crosstalk calibration measurements were done with a polarizing sheet installed in front of the telescope at IRSOL. Measurements are done with 3 different wavelengths (4861, 5876 and 6563 Å) with the Sun at different declinations. We fitted the results with a polynomial of $3^{\text{rd}}$ degree. The corrections are done with the coefficients of 5876 Å which is calculated for the same date (declination) of the observations.

### 3.2.4 Spectrally scattered light

Spectrally scattered-light affects the polarization amplitudes. The effect of spectrally scattered-light can be modeled and determined by Stokes $I$ profiles recorded at the solar disk center with corresponding FTS spectra explained as in Sect. 3.2.1. Scattered light contributes not only to intensity but also to the fractional polarization signal. Therefore a spectrally scattered-light correction should be done both, to intensity and to the fractional polarization signal. The way of scattered light removal is explained in detail in Bianda (2003). Here, only the basic steps are explained.

What we observe is:

$$I_{\text{obs}} = I + s \times I_c \; , \tag{3.8}$$

where $I_{\text{obs}}$ is the observed intensity, $I$ is intensity, $I_c$ is continuum intensity, and $s$ is the scattered-light.

The corrected intensity can be calculated from

$$\left(\frac{I}{I_c}\right)_{\text{corr}} = (1 + s)\left(\frac{I}{I_c}\right)_{\text{obs}} - s \; . \tag{3.9}$$

Here $(I/I_c)_{\text{corr}}$ denotes the corrected $I/I_c$, and $(I/I_c)_{\text{obs}}$ is the observed $I/I_c$.

For Stokes $V/I$ similarly holds:

$$\left(\frac{V}{I}\right)_{\text{corr}} = \left(\frac{V_{\text{obs}}}{I_{\text{obs}}} - k\right)\frac{I_{\text{obs}}}{I_{\text{obs}} - sI_{\text{c,obs}}/(1 + s)} \; . \tag{3.10}$$

Here $(V/I)_{\text{corr}}$ denotes the corrected $V/I$, and $(V/I)_{\text{obs}}$ is the observed $V/I$. The corrected $V/I$ signals are then converted into $V/I_c$ signals in order to be used in the inversion code (see Sect. 4.4).

### 3.2.5 Spatial scale

In order to determine the spatial scale, observations are done while recording slit-jaw camera images. Observations without solar tracking are started when the west limb of

the Sun was visible on one and finished when the solar image reached the other end of the slit. With this method, we were able to relate the slit-jaw images to the ZIMPOL II images and determine their spatial scale.

From the motion of the solar image along the slit, the slit height is determined at the slit-jaw camera. The slit-jaw images were related with the ZIMPOL II images and then the spatial scale (arc-second per pixel) on the ZIMPOL II camera is calculated to 1".3/px.

### 3.2.6   Noise level

Noise level is calculated with the averaged standard deviation of the continuum parts of the Stokes $V/I_c$ signal. For determination, standard deviation of 4 parts in the continuum of Stokes $V/I_c$ signal is calculated from the data set, and an average value of the standard deviations are assumed to be the noise level of $1.8 \times 10^{-3}$ of the intensity.

### 3.2.7   Seeing

In order to determine the effective smearing due to seeing in the observations, Stokes $I$ images are used. In the spectral lines along the slit, the size of the smallest resolved structure is measured. From these calculations, the seeing value is adopted to be 3 ".

# 4 Analysis of observed data

The analysis of the observed data can be divided into two main parts: The statistical analysis of the observed region from the Stokes profiles based on techniques (Sect. 4.1) and inversions of the Stokes profiles (Sect. 4.4). In the statistical part, Stokes $V$ asymmetries (Sect. 4.1.1), Stokes $V$ ratios (Sect. 4.1.2), and velocities (Sect. 4.1.3) calculated from both Stokes $I$ and Stokes $V$ are investigated. Binned observed profiles are introduced in Sect. 4.2. Contribution and response functions of the observed spectral lines are presented in Sect. 4.3 for further use.

The usage of the Stokes $V$ ratios as a temperature diagnostic tool is the main purpose of this thesis study. To make use of this technique, we selected C I 5380.323 Å as proposed by Solanki and Brigljević (1992), 2 iron lines (Fe I 5379.574 Å, Fe I 5383.369 Å, and a Ti II 5380.015 Å line in the 5 Å neighborhood of the C I line.

The C I line shows weak Stokes $V/I_c$ signals (0.3% to 1.0% at the spatial locations selected for analysis) as compared to the other chosen spectral lines (Fe I 5379.574 Å and Ti II Stokes $V/I_c$ signals are $1.5\% - 5.5\%$, and Fe I 5383.369 Å signals are $2\% - 6\%$ at the same spatial locations). Since C I line is formed in the deep observable layer of the photosphere, it is a key ingredient of our study (see Sect. 4.1.2 for more details). The weak signals in C I require determining the Stokes $V/I_c$ amplitudes with great accuracy. To reduce the noise in the Stokes $V/I_c$ signal, a 3 pixel spectral smoothing is applied to all Stokes $V/I_c$ data. This corresponds roughly to the slit width, so that we do not significantly degrade the profiles in the process. Furthermore, we used only those spectra, in which the Stokes $V/I_c$ amplitudes in all spectral lines are larger than three times the noise level. This provides us with a data set of 102 individual spectra. For each profile, the amplitudes of the blue and the red lobe of the Stokes $V/I_c$ are determined, and the areas of the blue and red lobes are calculated to study Stokes $V$ amplitude and area asymmetries (Sect. 4.1.1). Later on, the amplitude and area ratios between different lines are constructed and used as a temperature diagnostic tool (Sect. 4.1.2). Velocities obtained from both, Stokes $I$ line cores (Sect. 4.1.3.1), and Stokes $V$ zero crossing wavelengths (Sect. 4.1.3.2) are measured, and the relations between zero crossing velocities and asymmetries are presented in Sect. 4.1.3.3.

To further improve the signal to noise ratio, the data set was divided into 5 classes, depending on the Stokes $V$ signal strength of the carbon line. Each class is then binned to a single profile (Sect. 4.2). We analyzed Stokes $V/I_c$ amplitude and area ratios of the 5 binned profiles by inverting them using SPINOR (Stokes-Profile-INversion-O-Routines, Frutiger et al. 2000) to obtain the temperature stratification along the line-of-sight (Sect. 4.4). The resulting Stokes $V$ amplitude and area ratio values of the synthetic profiles are then compared to the measured ones. This allowed us to construct the temperature structure of the small-scale magnetic elements down to deep photospheric layers, despite

Table 4.1: Spectral lines

| Element | $\lambda_0$ (Å) | Transition | $\chi_{\text{ex}}$ (eV) | $\chi_{\text{ion}}$ (eV) | $\log(gf)$ | $\epsilon_0$ | $\sigma$ | $\alpha_{\text{col}}$ | $g_{\text{eff}}$ |
|---|---|---|---|---|---|---|---|---|---|
| [†]Fe I | 5379.574 | $b^1G_4^2 - z^1H_5^0$ | 3.69 | 7.87 | -1.13 | 7.45 | 363.0 | 0.249 | 1.096 |
| C I | 5380.323 | $^1P_1^0 - ^1P_1$ | 7.68 | 11.26 | -1.52 | 8.39 | 1237.0 | 0.229 | 1.0 |
| Ti II | 5381.015 | $b^2D_{3/2} - z^2F_{5/2}^0$ | 1.80 | 13.58 | -1.80 | 4.90 | 272.0 | 0.314 | 0.922 |
| [‡]Fe I | 5383.369 | $z^5G_5^0 - e^5H_6$ | 4.31 | 7.87 | 0.64 | 7.45 | 836.0 | 0.278 | 1.123 |

[†]*Hereafter named as Fe I$_b$*
[‡]*Hereafter named as Fe I$_r$*

the low spatial resolution. Already existing model atmospheres are tested by synthesizing the spectral lines of interest, amplitude and area ratios are constructed and compared with the observations (Sect. 4.4.3).

Characteristics of the observed spectral lines are presented in Table 4.1. Here, $\lambda_0$ denotes the central wavelength in the quiet Sun, $\chi_{\text{ex}}$ is the excitation potential, $\chi_{\text{ion}}$ the ionization potential of the relevant ion, $\log(gf)$ is the logarithmic, statistically weighted oscillator strength, $g_{\text{eff}}$ is the effective Landé factor of the line, and $\epsilon_0$ is the elemental abundance on a log scale on which $\epsilon_0(H) = 12.0$. Solar chemical abundances are adopted from Grevesse et al. (2007), and atomic data are taken from NIST[1] (Ralchenko et al. 2008); $\log(gf)$ values were determined by the inversion of the mean flat field profile (see Sect. 4.4). Width cross-section for collisional broadening ($\sigma$) and corresponding velocity parameters ($\alpha_{\text{col}}$) were provided by P. S. Barklem (*private communication*).

# 4.1   Stokes V profiles based techniques

In this section Stokes $V$ line asymmetries (Sect. 4.1.1), line ratios (Sect. 4.1.2), and velocities calculated from Stokes $I$ (Sect. 4.1.3.1) and Stokes $V$ (Sect. 4.1.3.2) as a function of amplitude sums are presented for the statistical analysis of the observed region. Additionally, asymmetries and zero-crossing velocity relations are investigated (Sect. 4.1.3.3).

## 4.1.1   Stokes V amplitude and area asymmetries

In an atmosphere without velocity gradients along the line-of-sight (LOS), Stokes $Q$ and $U$ are symmetric with respect to the line center and Stokes $V$ is antisymmetric (Landi Degl'Innocenti and Landi Degl'Innocenti 1981). However asymmetric Stokes $V$ profiles were observed by Stenflo et al. (1984) in faculae and the network near the disk center. The breakdown of this symmetry in the presence of velocity gradients has been studied extensively for Stokes $V$ (Auer and Heasley 1978, Sánchez Almeida et al. 1988, Solanki and Pahlke 1988, Grossmann-Doerth et al. 1989, Solanki 1989, Bellot Rubio et al. 2000, López Ariste 2002). The results of these studies showed that the asymmetry of the shape of the Stokes $V$ blue and red lobes can be produced by vertical, horizontal, or temporal velocity gradients (more details in Solanki 1993).

We observed an active region plage (avoiding sunspots and pores) nearly at solar disk center with low spatial resolution (Sect. 3.1). We aim to have statistics of the Stokes $V$

---

[1]National Institute of Standards and Technology

amplitude and area asymmetries in this region, investigate their relation with the observed zero crossing velocities and compare our results with previous studies. Relations between asymmetry and the zero-crossing velocities will be discussed in Sect. 4.1.3.3 after defining the velocities obtained from both, Stokes $I$ and Stokes $V/I$ in Sect. 4.1.3.

A typical Stokes $V$ profile is presented in Fig. 4.1. This figure demonstrates the definition of the following parameters used in this study:
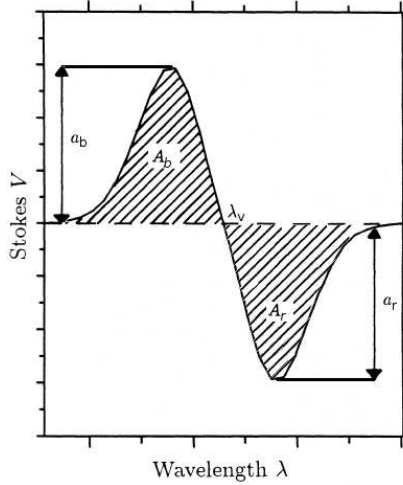


Figure 4.1: Schematic representation of a Stokes $V$ profile showing amplitude of blue ($a_b$) and red ($a_r$) and areas of blue ($A_b$) and red ($A_r$) lobes and zero crossing wavelength ($\lambda_v$) (*modified from* Keller et al. 1990).

- Sum of Stokes $V$ amplitudes: $|a_b| + |a_r|$

- Absolute amplitude asymmetry: $|a_b| - |a_r|$

- Relative Stokes $V$ amplitude asymmetry:

$$\delta a = \frac{|a_b| - |a_r|}{|a_b| + |a_r|} .$$
(4.1)

- Sum of Stokes $V$ areas: $|A_b| + |A_r|$

- Absolute area asymmetry: $|A_b| - |A_r|$

- Relative Stokes $V$ area asymmetry:

$$\delta A = \frac{|A_b| - |A_r|}{|A_b| + |A_r|} ,$$
(4.2)

where $|a_b|$ is the absolute amplitude of the blue wing, $|A_b|$ is the area of the blue wing, while $|a_r|$ and $|A_r|$ are the same quantities for the red wing of the Stokes $V$ profile. Hereafter we will omit the $'||'$ sign to present amplitudes and areas.

Areas of blue and red lobes of the Stokes $V$ signal are calculated as:

$$
\begin{aligned}
A_b &= \int_{\lambda_b}^{\lambda_v} V(\lambda)d\lambda \\
A_r &= \int_{\lambda_v}^{\lambda_r} V(\lambda)d\lambda
\end{aligned}
\tag{4.3}
$$

where $\lambda_v$ is the zero crossing wavelength, $\lambda_b$ is the wavelength at the beginning of $A_b$, $\lambda_r$ is the wavelength at the end of $A_r$ and $V(\lambda)$ is the Stokes $V$ signal at a given wavelength.

Noise in the Stokes $V$ signal has strong effect on amplitudes. To reduce the influence of the noise on the determination of the amplitudes, the blue and the red amplitudes of the Stokes $V/I_c$ of the individual observations are determined using a $2^{nd}$ order polynomial fit to the 5 pixels neighboring the tops of the Stokes $V$ lobes. Stokes $V$ areas are less affected by noise than the amplitudes but this quantity is strongly affected by blends. $\lambda_b$ and $\lambda_r$ were chosen to lie far in the wings, so that noise could be canceled out in the Stokes $V$ continuum. Thus, areas of the lobes could be determined more accurately.

In Fig. 4.2 and in Fig. 4.3 we present both, amplitude and area asymmetries for all 102 measured Stokes profiles as a function of amplitude sums of the spectral lines. These amplitude sums can be used as a proxy for magnetic filling (Sigwarth et al. 1999). To investigate the trends in the relations of the amplitude and area asymmetries with the strength of the Stokes $V$ signal, we performed a linear fit (solid lines in Fig. 4.2 and in Fig. 4.3) to the individual observations (stars in Fig. 4.2 and in Fig. 4.3). Standard deviations ($\sigma$) of the amplitude and areas are calculated and $1\sigma$ levels are presented with dashed lines in both Fig. 4.2 and Fig. 4.3 to see whether the linear fits are reliable or not.

In Fig. 4.2, amplitude asymmetries of the observed spectral lines are presented as a function of their Stokes $V$ signal sums. Amplitude asymmetries always have positive values in titanium and both of the iron lines, meaning that the blue lobes of Stokes $V$ have larger amplitudes than the amplitudes of the red lobe. Solanki and Stenflo (1984, 1985) were the first ones to report $a_b > a_r$ on network and plage regions at the disk center for Fe I and Fe II lines. The asymmetries in the carbon line shows both, positive and negative amplitude asymmetries. This can be because the weak signal in carbon causes the amplitude asymmetries to be more scattered than for the other lines, since it is more difficult to determine the amplitudes of this line very accurately. But on average the amplitude asymmetry of the carbon line remains positive, as seen from the linear fit.

If we compare amplitude asymmetries obtained from different spectral lines, we can interpret the amplitude asymmetry variation with height along the magnetic structure. We see more asymmetric profiles on the higher part of the magnetic structures and decreasing asymmetries with decreasing height (See Fig. 4.2). The profiles show larger asymmetries for the spectral lines formed in higher layers (Fe I$_r$).

Fig. 4.2 shows that the amplitude asymmetries for the observed spectral lines except the carbon line, decrease with increasing Stokes $V$ signal. This allows us to conclude that
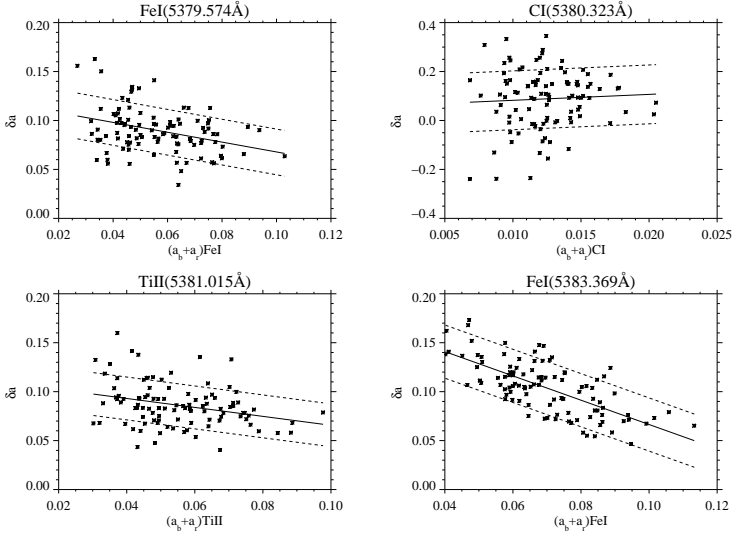
Figure 4.2: Amplitude asymmetries in Fe I$_b$ (top left), C I (top right), Ti II (bottom left) and Fe I$_r$ (bottom right). The solid line is a linear fit to the data points, and dashed lines indicate the $1\sigma$ levels of the linear fit.

the asymmetries weaken with increasing magnetic filling. This is in good agreement with the model of Solanki (1989). This relation has also been reported by Zayer et al. (1990), Fleck (1991), Grossmann-Doerth et al. (1996), Martínez Pillet et al. (1997), Sigwarth et al. (1999), and many other authors. The most prominent asymmetry change is seen in Fe I$_r$, while there is almost no trend in the C I line possibly due to scatter. Fe I$_b$ and Ti II have a similar Stokes *V* signal, with similar asymmetries, therefore the trends are very similar, too.

Errors on the determination of amplitudes of the individual observations are calculated from the standard deviations of the Stokes *V* signal in the continuum and propagated for the sum, substraction and division processes. The errors on the amplitude sums are 0.18% and 3% for the amplitude asymmetries except for the C I line, for which the error in amplitude asymmetry is 15%.

In Fig. 4.3, area asymmetries of the observed spectral lines are presented as a function of their amplitude sums. In all observed lines we see both positive and negative area asymmetries with almost zero value on average, which means that the areas calculated from blue and red lobes are equal on average. This can be due to the blends, which affect the line wings, in other words the areas. Additionally, in all observed lines there is no evidence for a relation of the area asymmetries with magnetic filling. This is a confirmation of the results of Zayer et al. (1990), Martínez Pillet et al. (1997). In their studies they also concluded that the Stokes *V* area asymmetries are almost independent of
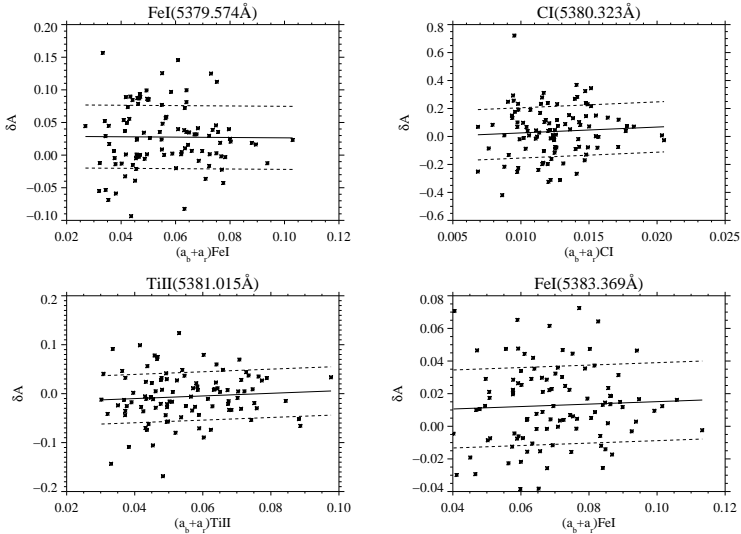
Figure 4.3: Area asymmetries in Fe I$_b$ (top left), C I (top right), Ti II (bottom left) and Fe I$_r$ (bottom right). The solid line is the linear fit to the data points and dashed lines are the $1\sigma$ level of the linear fit.

magnetic filling factor.

The typical errors are 0.5% for the area asymmetries except for the C I line. In this line the error on area asymmetry is 13%. The errors in the area asymmetries are smaller than the errors on the amplitude asymmetries since the integration over many wavelength bins makes them less affected by the noise.

### 4.1.2   Amplitude and area ratios

The idea of using two spectral lines with different magnetic or temperature sensitivities, and comparing their ratios, has started with the technique called magnetic line ratios, which was introduced by Howard and Stenflo (1972) and revised by Stenflo (1973). Stenflo (1975) made use of line ratios as a temperature diagnostic tool. The concept of forming the Stokes $V$ amplitude ratios of different spectral lines, which have different temperature sensitivities, for the investigation of the temperature structures of flux tubes was explained by Landi Degl'Innocenti and Landolfi (1982) in a theoretical context. Later on, this method was used by many authors e.g. Solanki and Stenflo (1984, 1985, 1986), Solanki et al. (1987), Stenflo et al. (1987), Zayer et al. (1990), Keller et al. (1990). Stenflo et al. (1987) studied the Stokes $V$ ratios of two Fe I lines and introduced the term called "thermal line ratios". In their study, they concluded that the thermal line ratios can be used as a diagnostic tool for the determination of the temperature structure of the flux tubes.

In the study of Keller et al. (1990) Stokes $V$ area ratios of Fe I to Fe II are also used to determine the temperatures. Their conclusion was that the Stokes $V$ area ratios of Fe I to Fe II lines provide excellent diagnostic for the temperature stratification of magnetic flux tubes.

In our study, instead of using Stokes $V$ ratios of Fe I to Fe II lines, the ratios of C I to Ti II and to Fe I lines were used. The reason is that Solanki and Brigljević (1992) introduced a spatial-resolution independent technique to obtain the continuum contrast of small scale magnetic features relative to the quiet Sun. In their study they pointed out that the weak lines of C I provide an ideal extension to the deep layers and they used Stokes $V$ amplitude ratios of C I to Fe II lines as a temperature diagnostic tool. Here we use the amplitude and area ratios of C I to two Fe I lines and C I to Ti II line as a temperature diagnostic tool, not to construct temperatures of the structures. This choice of the spectral lines is done because of the observation of the carbon line and its 5 Å neighborhood. For this reason, no Fe II line could be selected for observations. This Stokes $V$ line ratio technique has the advantage of being independent on the unknown magnetic filling factor, i.e. the fraction of the magnetized area within the resolution element, and it is not affected by the atmosphere outside of the magnetic structure. Stokes $V$ line ratio technique constitutes the main analysis technique of this thesis work.

The advantage of using this set of lines (see Sect. 3.1) is that their Stokes $I$ and Stokes $V/I$ signals could be observed simultaneously. They form at different heights in photosphere (see Sect. 4.3.1), in other words, they provide height coverage on the temperature and on its gradient. Even though this is a disadvantage for the usage of the Stokes $V$ line ratio technique, their opposite response to temperature (see Sect. 4.3.2) shows that they still can be use as a temperature diagnostic tool. The ratios of C I to the other lines provide a good temperature indicator for photosphere. Definitions of amplitude and area ratios are given in the following.

- Amplitude ratios:

$$r_a = \frac{(|a_b| + |a_r|)_{C_I}}{(|a_b| + |a_r|)_v} \ , \qquad (4.4)$$

where $|a_b|$ is the absolute amplitude of the blue lobe and $|a_r|$ is the absolute amplitude of the red lobe of the Stokes $V/I_c$ signal, the index $v$ stands for the spectral lines Fe I$_b$, Ti II and Fe I$_r$.

- Area ratios:

$$r_A = \frac{(|A_b| + |A_r|)_{C_I}}{(|A_b| + |A_r|)_v} \ , \qquad (4.5)$$

where $|A_b|$ is the area of the blue lobe and $|A_r|$ is the area of the red lobe of the Stokes $V/I_c$ signal, the index $v$ stands for the spectral lines Fe I$_b$, Ti II and Fe I$_r$.

In order to improve the visibility of the relation between amplitude and area ratios, a power law fit is applied to the individual observations, which are presented by solid lines in Fig. 4.4 and Fig. 4.5. Power law fits are calculated by:

$$r = a + bV^{-\gamma} \ , \tag{4.6}$$

where, r is the amplitude or area ratio, $V$ is the Stokes $V$ amplitude or area and a,b,$\gamma$ are free parameters in the fitting process.

In Fig. 4.4 and in Fig. 4.5 amplitude and area ratios are presented respectively. Both Stokes $V/I_c$ amplitude and area ratios decrease with increasing Stokes V amplitude of the spectral line (i.e. with stronger Stokes $V/I_c$ signal). Like in Fig. 4.2, and in Fig. 4.3 the x-axis can be interpreted as magnetic filling factor. The y-axis is a measure for the temperature or its gradient. Fig. 4.4 shows that the magnetic structures in regions with less magnetic flux are on average hotter and brighter than those in regions with higher flux.

We investigate amplitude and area ratios with inversions and 3-D MHD simulations in Chapter 4.4 and Chapter 5.1 respectively. Given that the C I line strengthens with increasing temperature (Livingston et al. 1977, Elste 1987, Holweger and Müller 1974, Solanki and Brigljević 1992) while the other 3 lines weaken (i.e. their $V$ amplitudes drop or remain roughly the same). Further analysis shows that a decrease in the plotted line ratios implies a decrease in temperature (see Sect. 4.4.2). Typical errors in amplitude ratios are 3.5% while it is 0.2% in areas.

### 4.1.3   Velocities

Stokes $I$ signal is affected by both magnetic structures and their non-magnetic surroundings (Solanki 1990). Therefore, for spatially unresolved structures, Stokes $I$ contains information about velocities of both, magnetic and non-magnetic regions. In contrast, the velocities measured from the Stokes $V$ are the velocities, only within the magnetic features. With making use of both Stokes $I$ and Stokes $V/I$ signals, we can extract information about the velocities of the magnetic structures themselves and their non-magnetic environment.

In this section we present some statistics of the velocities measured from Stokes $I$ (Sect. 4.1.3.1) and Stokes $V/I$ (Sect. 4.1.3.2) signals; relations of the Stokes $V$ asymmetries with the velocities observed at Stokes $V$ signal are investigated (Sect. 4.1.3.3). Due to the absence of the absolute wavelength reference, for each spectral line the mean wavelength value of the Stokes $I$ line core is assumed to be the reference wavelength for the velocity calculations after correcting for granular blue-shifts given in Table 4.2 with the references. There were no available convective blue-shift value for Ti II line but since the features of this line is very similar to Fe I$_b$ line and their formation heights are almost the same, we assumed the same convective blue-shifts for both of the lines. Another reason for this assumption is that Brandt and Solanki (1990) studied this Ti II line together with many other iron lines which includes Fe I$_b$ line too. Therefore, we believe that this assumption of similar convective blue-shifts are reliable.

#### 4.1.3.1   Velocities measured from Stokes I

Wiggles in the Stokes $I$ spectrum presented in Fig. 3.8 are indicators of the upwards moving (shifts to more blue wavelengths) and downwards moving (shifts to more red wave-
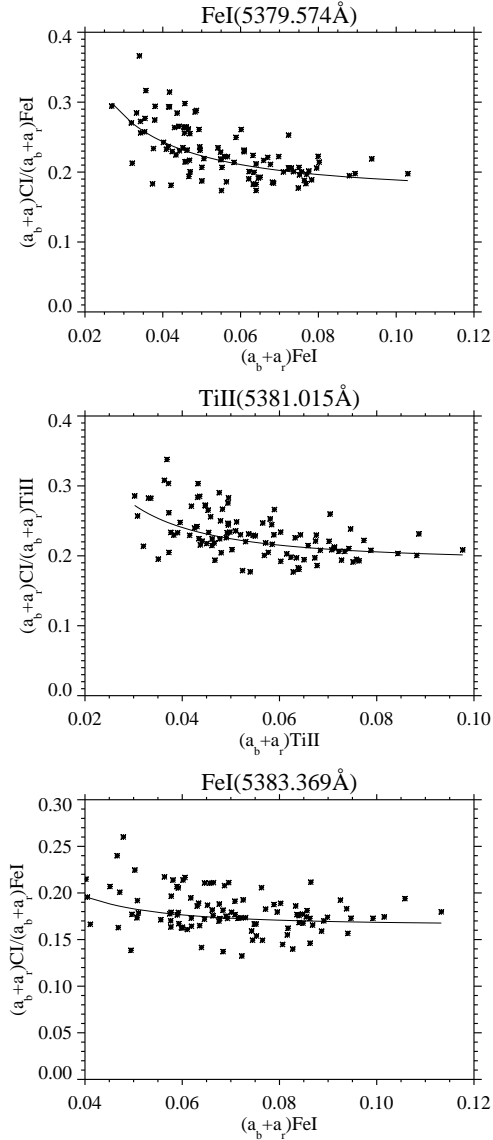
Figure 4.4: Amplitude ratios of C I to Fe I$_b$ (top), to Ti II (middle) and to the Fe I$_r$ (bottom) line. The solid lines show power law fits to the individual data points.
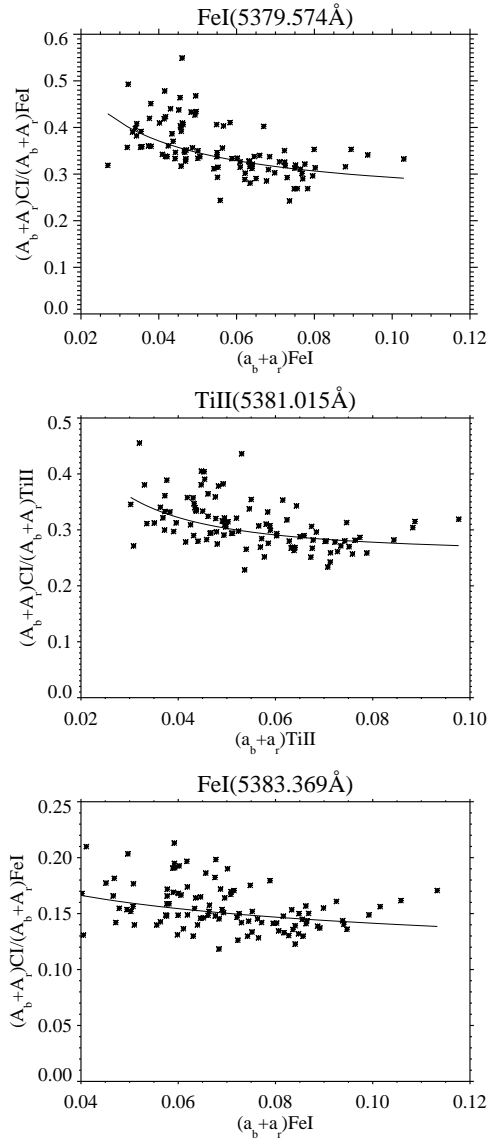
Figure 4.5: Area ratios of C I to Fe I$_b$ (top), to Ti II (middle) and to the Fe I$_r$ (bottom) line. The solid lines show power law fits to the individual data points.

Table 4.2: Convective blue-shifts of the observed spectral lines

| Element | $\lambda_0$ (Å) | Velocity (m/s) | reference |
|---------|-----------------|----------------|-----------|
| Fe I  | 5379.574 | -307 | Langangen et al. (2007) |
| C I   | 5380.323 | -864 | Langangen et al. (2007) |
| Ti II | 5381.015 | -307 | *assumed to be the same as Fe I$_b$* |
| Fe I  | 5383.369 | -152 | Dravins et al. (1981) |

lengths) material in the observed region. To investigate these velocities, line cores of the Stokes $I$ signals are determined with a 2$^{nd}$ order polynomial fit to the bottom of the profiles and corresponding wavelength positions are measured for each observed spectral line.

The velocities from Stokes $I$ are calculated as:

$$v_I = \frac{\lambda_{I\,obs} - \bar{\lambda}_{I\,obs}}{\bar{\lambda}_{I\,obs}} c \, , \tag{4.7}$$

where $\lambda_{I\,obs}$ is the observed wavelength in Stokes $I$, $\bar{\lambda}_{I\,obs}$ is the reference wavelength, c is the speed of light.
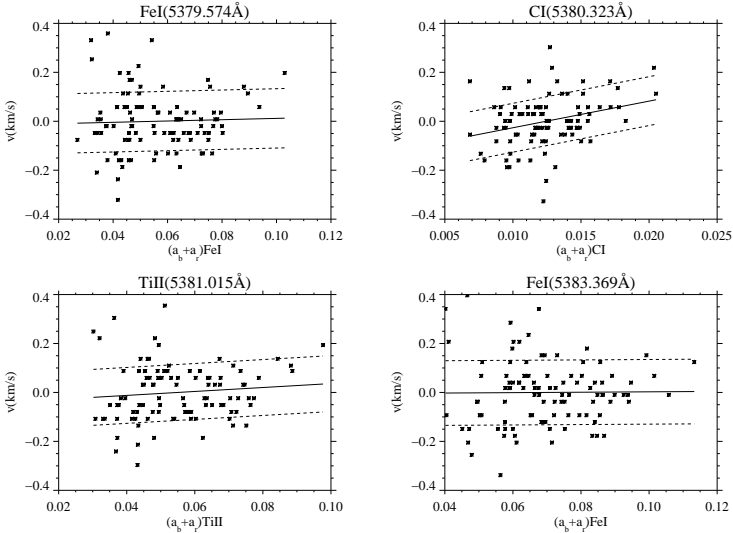


Figure 4.6: Up and down flows observed in Fe I$_b$ (top left), C I (top right), Ti II (bottom left) and Fe I$_r$ (bottom right). The line shows the linear fit to the data points and dashed lines are the 1$\sigma$ level of the linear fit.

In Fig. 4.6 measured velocities from Stokes $I$ in each spectral line are presented vs. amplitude sums of their Stokes $V$ signals. To investigate the relation between the velocities and the Stokes $V$ strength, linear fits are performed to the data set, which are presented with solid lines in Fig. 4.6 and the $1\sigma$ levels are presented with dashed lines. In all the spectral lines, we see velocities varying approximately between $\pm\,100\,$m/s. No clear trend is observed with increasing Stokes $V$ signal in the lines except the carbon line. In the carbon line, we see more red shifted profiles with increasing magnetic filling. But this trend doesn't seem to be real if we look at the data bulk.

### 4.1.3.2   Stokes V zero crossing velocities

Zero crossing wavelength of the Stokes $V$ profiles can be used as a diagnostic tool to investigate velocities, since these shifts are mainly caused by the gas motions in the magnetic element. Zero crossing velocities are defined as:

$$v_V = \frac{\lambda_v - \bar{\lambda}_{\mathrm{I\,obs}}}{\bar{\lambda}_{\mathrm{I\,obs}}} c \qquad (4.8)$$

where $\lambda_v$ is the zero crossing wavelength in Stokes $V$, $\bar{\lambda}_{\mathrm{I\,obs}}$ is the reference wavelength, c is the speed of light.

Since zero-crossing wavelengths are easily affected by noise, we determined zero crossing wavelengths in the Stokes $V$ signal with applying a linear fit between Stokes $V$ measurements in the close neighborhood of the expected zero crossing point.

In Fig. 4.7, measured zero crossing velocities are presented vs. Stokes $V$ amplitude sums of the spectral lines. Solid lines represent linear fits, while the dashed lines represent $1\sigma$ levels. Decreasing zero crossing velocities with increasing Stokes $V$ signal are observed in each spectral line, which indicates the motions are obstructed by the magnetic field strength. We see significantly different velocities for different spectral lines, which allows us to construct the velocities along the magnetic structures. This is a consequence of the fact that the spectral lines are formed at different heights in the atmosphere. In all spectral lines we see red-shifted Stokes $V$ profiles, which indicates that the structures we observed are located in the inter-granular lanes, where there are down-flows. This result is consistent with the results of Martínez Pillet et al. (1997), Sigwarth et al. (1999). In the magnetic structures we see velocities decreasing with height from C I to Fe I$_r$ . Since the C I line is formed in the deep atmosphere, i.e. in the hotter region, higher velocities can be observed. Velocities observed in the Ti II line is very similar to the ones observed in the Fe I$_b$ line, which are lower than the ones we measured in the C I line. In the Fe I$_r$ line we see the lowest velocities as compared to the other lines, with increasing Stokes $V$ signal.

### 4.1.3.3   Relations between Stokes $V$ asymmetries and zero crossing velocities

Velocity gradients are known to produce Stokes $V$ asymmetries. Therefore in this subsection we investigate the relations of the zero crossing velocities with amplitude and with area asymmetries.

Relations between zero crossing and amplitude asymmetries are presented in Fig. 4.8. Solid lines represent the linear fits, while the dashed lines represent the $1\sigma$ levels. No
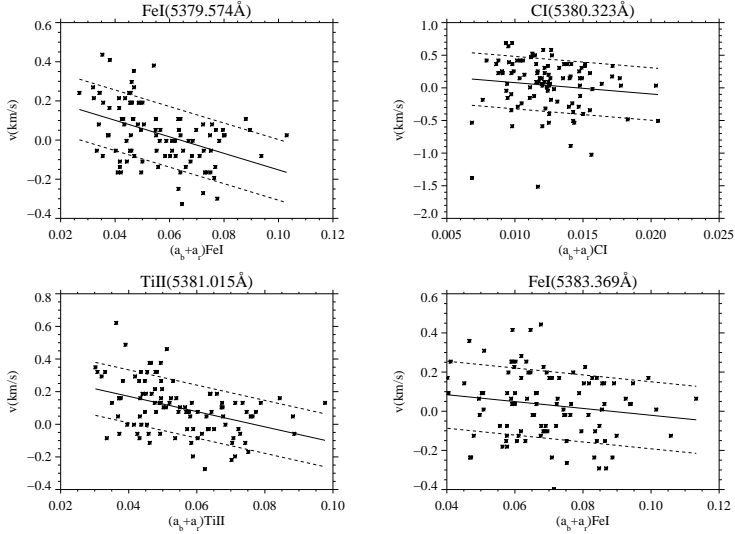
Figure 4.7: Zero crossing velocities observed in Fe I$_b$ (top left), C I (top right), Ti II (bottom left) and Fe I$_r$ (bottom right). The line shows the linear fit to the data points and dashed lines are the $1\sigma$ level of the linear fit.

correlation between $\delta a$ and zero crossing velocities are observed in the Fe I$_b$, the C I and the Ti II lines. Since the trend observed in the Fe I$_r$ line is not clear without the linear fit, this trend is not reliable. Our results are consistent with the results of Balasubramaniam et al. (1997).

Relations between zero crossing and area asymmetries are presented in Fig. 4.9. Solid lines represent the linear fits, while the dashed lines represent the $1\sigma$ levels. We observe clearly red-shifted and asymmetric profiles but no clear relation between zero crossing velocities and area asymmetries in Ti II and the Fe I$_r$ line. We see decreasing velocities with increasing area asymmetries in Fe I$_b$ line, while the observed trend is the opposite in carbon line. Since the scatter of the data points are huge these trends are not reliable. Therefore more statistics are needed to decide these trends.
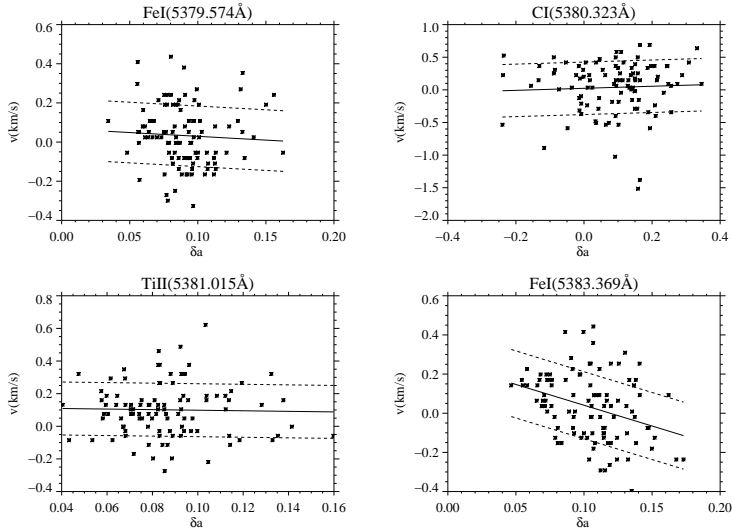
Figure 4.8: Zero crossing velocities observed in Fe I$_b$ (top left), C I (top right), Ti II (bottom left) and Fe I$_r$ (bottom right) as a function of amplitude asymmetries. The line shows the linear fit to the data points.

## 4.2  Binned observed profiles

To increase the signal-to-noise ratio, we divided our data set into 5 classes according to the Stokes $V/I_c$ amplitude sum of the C I profiles. The bins have been chosen such that the signals are homogeneously distributed in all classes (see Table 4.3). The average of the profiles are computed after reversing the sign of Stokes V of the negative polarity profiles to avoid cancelation effects. These 5 average profiles were labeled as weak, mid1, mid2, mid3 and strong (Table 4.3). Stokes $V/I_c$ signals of these profiles are presented in Fig. 4.10. The Stokes V amplitude varies roughly by a factor of 2 between the weakest and the strongest averaged profile. Without this averaging this ratio is slightly larger than 3. This binning reduced the typical noise level in the profiles to $2 \times 10^{-4}$ of the continuum intensity.
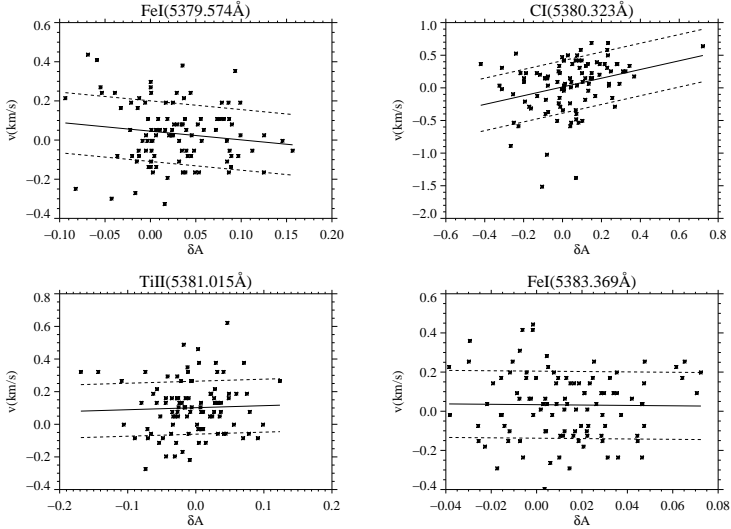
Figure 4.9: Zero crossing velocities observed in Fe I$_b$, C I (top right), Ti II (bottom left) and Fe I$_r$ (bottom right) as a function of area asymmetries. The line shows the linear fit to the data points.

Table 4.3: Binned data sets

| Data | Amplitude sum of the C I | # of averaged profiles |
|------|--------------------------|------------------------|
| weak | < 0.0100 | 20 |
| mid1 | 0.0100-0.0117 | 20 |
| mid2 | 0.0117-0.0126 | 20 |
| mid3 | 0.0126-0.0145 | 20 |
| strong | > 0.0145 | 22 |

## 4.3 Response and contribution functions

Contribution (Sect. 4.3.1) and response (Sect. 4.3.2) functions of the spectral lines are important to understand the formation height of the lines in the model atmosphere and to obtain diagnostic capabilities of the lines in intensity and in polarized light. Therefore, contribution and response functions are introduced and calculations are briefly explained in this section according to Frutiger (2000). More details about these functions can be found in Landi Degl'Innocenti and Landi Degl'Innocenti (1977), Grossmann-Doerth et al. (1988), Ruiz Cobo and del Toro Iniesta (1994), del Toro Iniesta (2003). Calculation of both, response and contribution functions of the spectral lines are done with STOPRO routines (Solanki 1987, modified by Jo Bruls) as explained in Frutiger (2000).
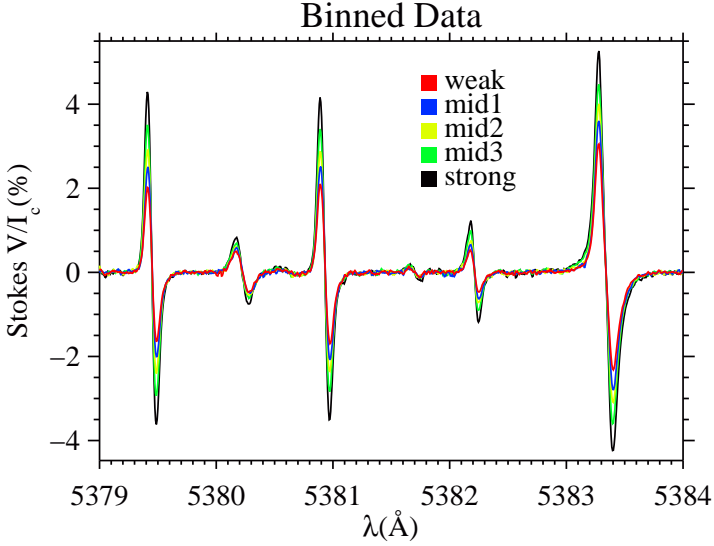
Figure 4.10: Binned Stokes *V* profiles for various strengths of the amplitude sum of C I.

In this section, we first introduce the formal solution of RTE in order to calculate contribution and response functions in order to define contribution (4.3.1) and response (4.3.2) functions. The formal solution of Eq. 2.4 (Landi Degl'Innocenti and Landi Degl'Innocenti 1985) relating the Stokes vectors at positions $s$ and $s'$ along the line-of-sight is:

$$I(s) = \mathbf{O}(s, s_0)\mathbf{I}(s_0) + \int_{s_0}^{s} \mathbf{O}(s, s')\mathbf{j}(s')ds' , \tag{4.9}$$

where $\mathbf{O}(s, s')$ is the Stokes-attenuation operator $4 \times 4$ matrix satisfying,

$$\frac{d}{ds}\mathbf{O}(s, s') = -\mathbf{K}(s)\mathbf{O}(s, s') ; \mathbf{O}(s, s) = \mathbf{1} . \tag{4.10}$$

### 4.3.1   Contribution functions and the formation heights of the spectral lines

Contribution functions (CFs) inform us how the different atmospheric layers contribute to the observed spectrum. Spectral lines are not formed at one height in the atmosphere. Therefore, it is a common mistake to talk about the formation heights of the spectral lines as if they are formed at one height in the atmosphere. But in reality, the contribution to the formation of the line cores are from the higher atmospheric layers, while the contribution to the formation of the line wings are from deeper layers of the atmosphere. Therefore,

one cannot speak about the formation height of the spectral line in a specific wavelength along the spectral line. With introducing optical depth ($\tau$) such that $d\tau = -\kappa_c(1 + \eta_l)ds$ and a discrete depth grid ($\tau_k, k = 1, 2, ..., N$) the emergent vector (Eq. 4.10) can be written as:

$$I(\tau_1) = \sum_{k=1}^{N} \boldsymbol{C_k} d\tau_k \ . \tag{4.11}$$

Here $\boldsymbol{C_k}$ is the contribution vector $\boldsymbol{C_k} = \boldsymbol{O}(1,k)\boldsymbol{j_k}$, where $\boldsymbol{j_k}$ is the source vector at depth $\tau_k$.

Contribution functions presented in Fig. 4.11 are calculated with existing HSRASP atmospheric model (explained in Sect. 4.4). CFs of the spectral lines are presented from line core (solid line) to the wings with 0.03 Å steps along the lines. Solid lines show which atmospheric layers contribute to the formation of the line cores. Dotted, dashed, dashed-dotted and dashed-dotted-dotted lines are similarly showing the contribution of the atmospheric layers starting with 0.03 Å steps away form the line core to the wings. Steps in wavelength from the lines cores are represented in the legends in Fig. 4.11. From Fig. 4.11, we can see that the line cores are formed in much higher atmosphere than the line wings i.e. contribution to the line cores are coming from higher layers of the atmosphere except the C I line. All the contribution to form C I line comes from deeper atmospheric layers.

As clearly seen from the top right panel of Fig. 4.11, C I is formed at the bottom layers of the model atmosphere. Fe I$_b$ line and Ti II lines cover similar heights in the atmosphere, while Fe I$_r$ line covers a much higher range. Especially, the contribution to the line core of this line comes from very high in the atmosphere.

Line core formation heights of the spectral lines are assumed to be the heights corresponding to maxima of the solid lines. These heights are presented in Table 4.4.

Table 4.4: Line core formation heights of the spectral lines for a HSRASP atmosphere

| Spectral Line (Å) | line core [$\log(\tau)$] | line core [z(km)] |
|---|---|---|
| Fe I 5379.574 | -1.08 | 153 |
| C I 5380.323 | 0.02 | 0 |
| Ti II 5381.015 | -0.78 | 108 |
| Fe I 5383.369 | -2.68 | 379 |

### 4.3.2 Response functions and temperature sensitivities of the spectral lines

To characterize the diagnostic capabilities of the different spectral lines for retrieving physical parameters like temperature, magnetic field strength or velocity, we need to know the response of the Stokes signal of the spectral line to small perturbations of the physical parameters of the model atmosphere. Perturbations are defined as:

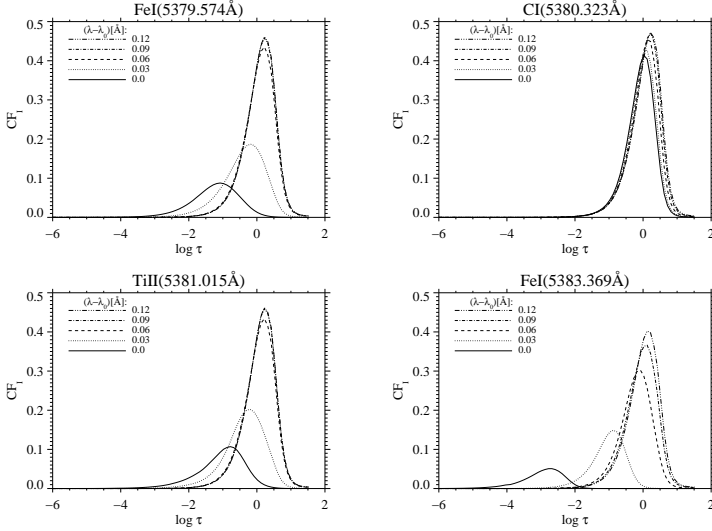$$\delta I = \int_{\tau}^{\infty} R_f(\tau) \delta f d\tau \tag{4.12}$$

Figure 4.11: Contribution functions of Stokes $I$ of the interested spectral lines for HSRASP atmosphere. Solid lines are the response functions in the line core, while other lines represent CFs away from the line core. Dotted is 0.03 Å, dashed 0.06 Å, dash-dot 0.09 Å and dash-dot-dot 0.12 Å from the line core.

where $\delta I$ is the modification on $I$ (Stokes vector) because of the perturbations, $f$ is the physical parameter, $R_f$ is the response function for the parameter $f$, $\delta f$ is the perturbation to the physical parameter and $\tau$ is the optical depth. Response functions (RFs) are defined as :

$$R_f(\tau) = \mathbf{O}(0,\tau)\left(\frac{\partial \boldsymbol{j}(\tau)}{\partial f} - \frac{\partial \boldsymbol{\eta}(\tau)}{\partial f}I(\tau)\right) \qquad (4.13)$$

Similar to Eq. 4.11, for a discrete grid modification on I can be written as,

$$\delta I(\tau_1) = \sum_{k=1}^{N} R_f(\tau_k)\delta f d\tau_k \,, \qquad (4.14)$$

where $R_k = \mathbf{O}(1,k)\boldsymbol{r_k}$, and $\boldsymbol{r_k} = \left(\frac{\partial \boldsymbol{j}(\tau_k)}{\partial \tau_k} - \frac{\partial \boldsymbol{\eta}(\tau_k)}{\partial \tau_k}I(\tau_k)\right)$.

In this study, the physical parameter of interest is the temperature. In Fig. 4.12 we present the RFs of Stokes $I$ (left panel) and Stokes $V$ (right panel) to perturbations of 50 K in temperature with respect to the HSRASP atmosphere with a height independent magnetic field strength of 1500 G. RFs of the spectral lines are presented from line core (solid line) to the wings in wavelength steps of 0.03 Å (coded in legends in Fig. 4.12).

Note that the Stokes *I* RFs are positive at $\log \tau \leq -0.5$ for all the lines except the C I line. This difference in sign reflects differences in temperature sensitivity. Whereas Fe I$_b$ strongly weakens in the core with increasing temperature (large positive RFs), Fe I$_r$ weakens mainly in wings & flanks (note the weak RF in the line core) and Ti II displays little weakening (indicated by the fact that the integral over the RF is close to zero). In contrast, C I displays a strengthening. It is this difference in behavior which makes ratios of the C I line to the other measured lines interesting temperature diagnostics.

RFs are helpful to determine the positions and number of temperature nodes needed for spectral line inversion (see Sect. 4.4) and to fix the upper boundary of the atmosphere for the radiative transfer computations. Figure 4.12 shows that the observed lines do not respond to temperature perturbations at $\log \tau < -5$. We therefore use this value as the upper boundary for the solution of the radiative transfer equation. Additionally, the placement of the temperature nodes is important, since we have four different spectral lines which are formed at different heights of the atmosphere. The response at $\log \tau = -3$ and $-4$ is low for all lines. As a result, test inversions that allow the temperature to vary at these nodes gave widely varying, unreliable results. Therefore we keep the atmospheric parameters of those nodes fixed in order to reduce the number of free parameters in the inversions described in the next section, as well as to enhance their stability.

In Fig. 4.12 we see that in Stokes *I* the perturbations in temperature have highest response at the line cores, while there is almost no response in Stokes *V*. This is because the line core positions are lying close to the zero crossing point in Stokes *V* signals. For *V*, the highest response is at around 0.03 Å further from the line core position which is almost the maximum of the Stokes *V* signals. For Fe I$_b$ and Ti II lines there is negligible response to temperature perturbations above $\log \tau = -3$, while it is $\log \tau = -2$ for C I line and $\log \tau = -5$ for the Fe I$_r$ line.
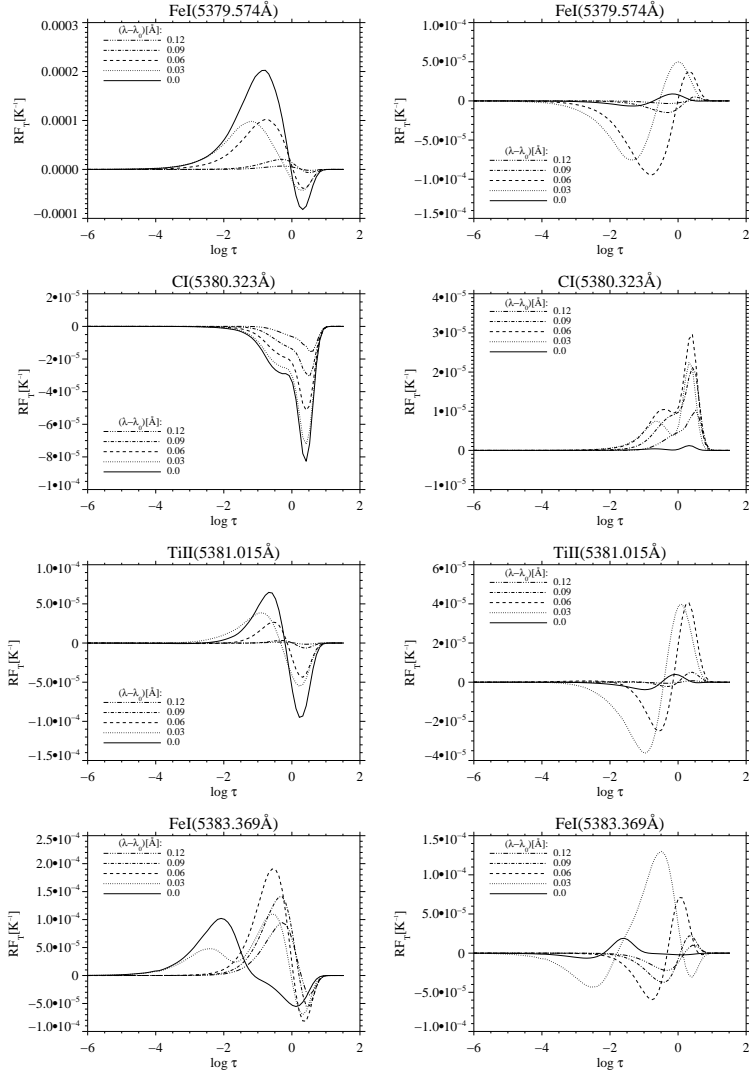
Figure 4.12: Response functions of Stokes *I* (panel on the left) and Stokes *V* (panel on the right) of the analyzed spectral lines to perturbations of temperature in an HSRASP atmosphere with a constant magnetic field of B=1500 G. Solid lines are the response functions in the line core, while other lines represent RFs away from the line core. Dotted is 0.03 Å, dashed 0.06 Å, dash-dot 0.09 Å and dash-dot-dot 0.12 Å from the line core.

## 4.4 Inversions

The idea behind the inversions is to solve the radiative transfer equation (RTE, Eq. 2.4) in order to calculate Stokes parameters starting from the initial guess atmosphere with modifying this atmosphere iteratively, until the best fit of the synthetic spectrum to the observed one is obtained. This is done by minimizing the $\chi^2$ merit function by non-linear least-squares fitting (Levenberg-Marquardt method, Press et al. 1992). In each iteration step, the spectra and all derivatives are calculated with various model parameters. The most convenient way to compute derivatives is by computing RFs since small changes in physical quantities have effect on the synthetic profiles and this effects can be seen by the RFs.

To obtain atmospheric stratifications of temperature from the observed line profiles, we use the inversion code SPINOR to solve the RTE. This code incorporates the STO-PRO routines, which compute synthetic Stokes profiles of one or more spectral lines upon input of their atomic data and one or more atmospheric models. Local thermodynamic equilibrium (LTE) conditions are assumed and the Unno-Rachkovsky radiative transfer equations (Unno 1956, Rachkovsky 1962) are solved using the Hermitian algorithm (Bellot Rubio et al. 1998). The synthetic profiles are normalized to the quiet Sun continuum intensity, which is computed using the HSRASP model (Chapman 1979). This model is an extended version of the HSRA model (Gingerich et al. 1971) atmosphere to greater depth by adding convection zone model of Spruit (1974). Additionally, this atmosphere was modified by Solanki (1989) in its chromospheric layers to be parallel to the Holweger and Müller (1974) model in order to avoid spurious emission cores in the stronger spectral lines due to the assumption of LTE. The temperature stratification of both HSRA and HSRASP are presented in Fig. 4.13. HSRASP is used because of its success in reproducing line profiles in the quiet Sun. From the initial atmospheres the synthetic profiles are iteratively fitted to the mean data sets using response functions and Levenberg-Marquardt algorithm by minimizing the merit function $\chi^2$ (Ruiz Cobo and del Toro Iniesta 1992, Frutiger et al. 2000). The code is described in greater detail by Frutiger et al. (2000) and Frutiger (2000).

Since we don't have high spatial resolution, we see both magnetic structures and non-magnetic environment in our pixels. Therefore, to represent the observations properly, a 1-D, plane parallel, two component model is used for the inversions of the binned profiles. The first component was chosen to represent the magnetic atmosphere, the second component was chosen to represent the non-magnetic environment.

We adopt the HSRASP (Spruit 1974, Chapman 1979) atmospheric model for both, the quiet Sun and the non-magnetic surroundings of the magnetic elements. At the relatively low resolution of our data (2.6 " at best; i.e. granules are not resolved) this dual role should be acceptable.

In order to obtain the $\log(gf)$ values of the employed lines (generally the most uncertain atomic parameter for an analysis such as this), the mean line profile produced by the flat fields is inverted using the HSRASP atmosphere. The free parameters of this inversion are: macroturbulent ($v_{\mathrm{mac}}$) and microturbulent velocity ($v_{\mathrm{mic}}$). The line-of-sight velocity ($v_{\mathrm{los}}$) of the mean flat field profiles was set to zero. No satisfactory fit to the mean flat field profile could be obtained with NIST $\log(gf)$ values. Assuming that the adopted
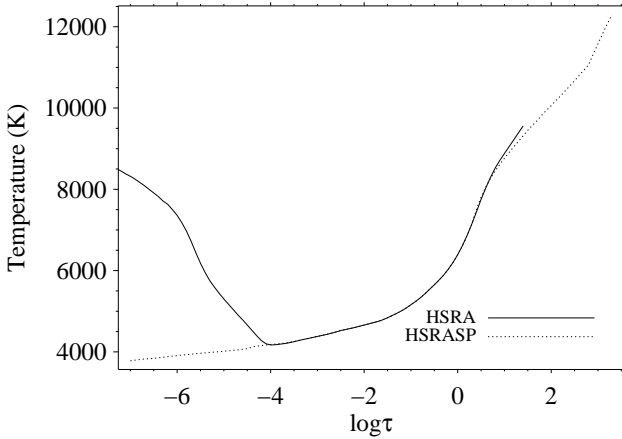
Figure 4.13: Comparison of HSRA (solid line) and HSRASP (dotted line) model atmospheres.

abundances are correct, we determined $\log(gf)$ values of the 4 selected spectral lines from the inversions (see Table 4.1).

The final best fit to the average quiet Sun (i.e. flat-field) profiles are displayed in Fig. 4.14. The fits to the Fe I$_b$ and C I are very satisfactory. The fits to the other two lines are also very good, but of somewhat lower quality. In the case of the Ti II 5381.015 Å line this is probably due to various weak atomic lines (Cr I, Ti I, Fe II) in its wings, which were neglected in our analysis but exist in the Vienna (VALD)[2] and Kurucz [3] data bases. For the subsequent analysis the $\log(gf)$ values retrieved from this inversion of the mean flat field profile are employed unchanged. The quiet Sun or field-free component in the subsequent inversions is described by the HSRASP and is assumed to have $v_{los} = 0$. $v_{mac}$ and $v_{mic}$ are allowed to vary.

An analysis of the RFs (Sect. 4.3.2) and a series of test inversions showed that temperature nodes of $\log \tau = 0$ (continuum), -0.5 and -1.0 are the optimum choice for the study presented here (i.e. the temperatures at these values for $\log \tau$ are free parameters). It is important to keep the number of free parameters in the inversions as low as possible in order not to crowd the $\chi^2$-hypersurface with local minima.

For the magnetic component, we used an atmosphere with 5 temperature nodes (2 fixed and 3 free, as explained in Sect. 4.3.2). The parameters for the magnetic atmosphere are: $v_{los}$ (at $\log \tau = 0$), velocity gradient (linear in $\log \tau$), $v_{mic}$, $v_{mac}$, magnetic field strength $B$ (at $\log \tau = 0$), magnetic field strength gradient (linear in $\log \tau$) and the magnetic filling

---

[2]Vienna Atomic Line Data-Base: http://vald.astro.univie.ac.at/ vald/php/vald.php
[3]Kurucz's atomic spectral line database: http://www.cfa.harvard.edu/amp/ampdata/kurucz23/sekur.html
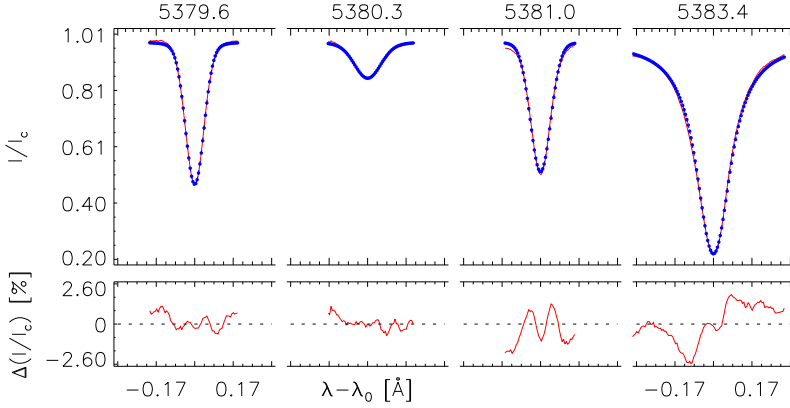
Figure 4.14: Stokes $I/I_c$ of the mean flat field profile and its best fit. Upper panel: thick dots (blue) represent the synthetic, the red solid lines represent the mean observed line profiles. Differences between synthetic and observed profiles are presented in the lower panel.

factor $\alpha$ determining the mixing ratio with the non-magnetic atmosphere derived from the inversion of the mean flat-field profile. The gradients in $v_{\text{los}}$ and $B$ are introduced to reproduce the asymmetries in the Stokes $V$ profiles (Solanki and Stenflo 1984, 1985). The magnetic field was assumed to be vertical to the solar surface, corresponding to an angle of $17°.5$ in the line-of-sight frame. In order to have good-fits to our small Stokes $V$ signals, 10 times more weights are applied to Stokes $V/I_c$ than Stokes $I/I_c$ signals.

To compute the Zeeman pattern atomic data are needed as an input for the inversions. An example of the input file to SPINOR is presented in Table. 4.5. The results of the inversions are presented in Sect. 4.4.1.

### 4.4.1 Inversion results

Combination of all 4 spectral lines allows us to retrieve temperature with the highest accuracy. The analysis of the RFs (see Fig. 4.12) and row of tests showed that we need to take into account all 4 spectral lines in order to obtain a reliable temperature stratification from the inversions independently of the initial conditions. Attempts to invert the spectra using only the Fe I 5379.6 Å C I 5380.3 Å and Ti II 5381.0 Å lines did not lead to a unique temperature stratification. Adding the Fe I 5383.4 Å line to inversions improved the determination of the temperature structure significantly. By inverting Stokes $I/I_c$ and Stokes $V/I_c$ of all 4 spectral lines simultaneously, a unique solution for the temperature stratification could be found for a given set of line profiles, within the limits of the model

Table 4.5: Description of atomic data required by STOPRO routines.

| N | Variable | Description | Unit |
|---|---|---|---|
| 1 | NLINES | Number of lines | [-] |
| 2 | WLREF | Reference wavelength (line center) | [Å] |
| 3 | WL1 WL2 NWL | WL-Grid : $\lambda_i = WLREF - WL1 + i\frac{WL2-WL1}{NWL}$ i=1,...,NWL | [Å] |
| 4 | NATOM | Atomic number, i.e. Fe=26 | [-] |
| 5 | ION | Ionization state, 1=neutral, 2=+, $ION \geq 3$ not allowed | [-] |
| 6 | ALOGGF | $\log_{10}(gf)$ | [-] |
| 7 | ABUND | Elemental abundance on a log scale on which A(H)=12.0 | [-] |
| 8 | EPOT | Energy of lower level | [ eV ] |
| 9 | IPOT1 | 1st Ionization potential $X \to X^+$ | [ eV ] |
| 10 | IPOT2 | 2nd Ionization potential $X^+ \to X^{++}$ | [ eV ] |
| 11 | RMASS | Atomic mass | [amu] |
| 12 | DMPEMP | Empirical damping enhancement factor | [-] |
| 13 | LANDEC | { =0 : gu and gl calculated from L,J,S  =1 : gl and gu provided as input (see below) | [-] |
| 14 | CFGL | Configuration/term description of lower level | [-] |
| 15 | 2SL+1 LL JL | Standard term description of lower level $^{2S_l+1}\mathbf{LL}_{J_l}$ | [-] |
| 16 | CFGU | Configuration/term description of upper level | [-] |
| 17 | 2SU+1 LU JU | Standard term description of lower level $^{2S_u+1}\mathbf{LU}_{J_u}$ | [-] |
| 18 | GL | Landé factors (only used if LANDEC=1, see above) | [-] |
| 19 | GU | Landé factors (only used if LANDEC=1, see above) | [-] |

(as explained in Sect. 4.4).

The Stokes $I/I_c$ and Stokes $V/I_c$ profiles of the 4 analyzed lines resulting from binned profiles, which are introduced in Sect. 4.2, are presented in Fig. 4.15 with solid red lines on the top parts of the plots along with the best fit synthetic profiles (blue dotted lines). The fits reproduce the observed profiles reasonably well, except for the Fe I 5379.6 Å line and for the wings of the Ti II line. The problem with Ti II, noticed already when fitting the quiet Sun profiles, is due to blends in the line wings (see Sect. 4.4). The somewhat poor fit to the flanks of Fe I (5379.6 Å) line is the due to the assumption of one $v_{mac}$ for all lines.

Amplitude and area ratios are calculated from synthetic profiles to compare with the results obtained from observations. Since our binned data have extremely low noise and the synthetic profiles are noise-free, it was precise enough to take the minimum and the maximum values in the Stokes $V/I_c$ signal to determine the amplitudes. Comparisons of synthetic data with the observations and with the binned data are presented in Fig. 4.16
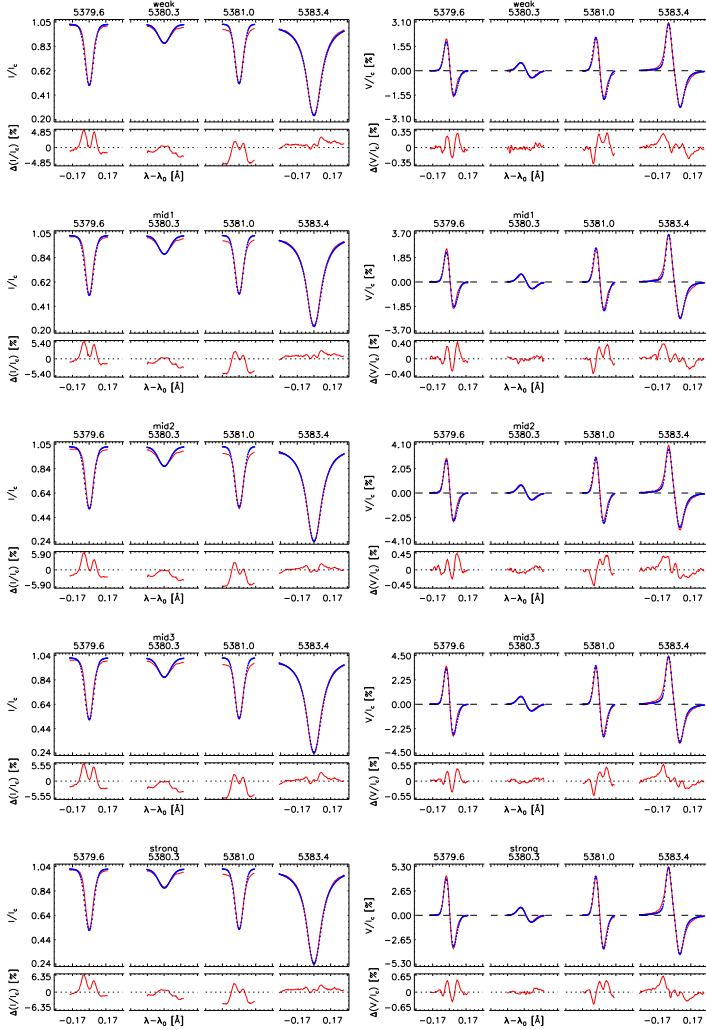
Figure 4.15: Binned profiles and best-fit synthetic profiles to weak, mid1, mid2, mid3 and strong data from top panel to the bottom panel. Stokes $I/I_c$ (left panel) and Stokes $V/I_c$ (right panel) of the data from weak (top panel) to strong (bottom panel). Solid lines represent the mean observed profile, dotted lines represent the synthetic profiles. Differences between synthetic and observed profiles ($\Delta(I/I_c)$ and $\Delta(V/I_c)$) are presented in the lower part of each plot.

and in Fig. 4.17. In Fig. 4.16, amplitude ratios of synthetic profiles (triangles) are presented with binned profiles (squares) and observations (stars). As seen in Fig. 4.16 amplitude ratios calculated from the synthetic data are representing well the observations since the power law fit obtained from the individual observations are also representative for the inversions. This is not surprising after presenting the obtained best fit profiles in Fig. 4.15. In Fig. 4.17 area ratios of synthetic profiles are presented with binned profiles and observations. Since the inversions were kept simple with few free parameters, we were not very successful to create the Stokes $V$ lobes of the strong iron line (Fe I$_r$). Therefore, even though the area ratios of the Fe I$_b$ and Ti II lines show good agreement with the observations, area ratios are excluded from further analysis.

Values of the free parameters except temperatures returned by the inversions are presented in Table 4.6. Here $\chi^2_{red}$ is the reduced $\chi^2$, i.e. value of the merit function characterizing the quality of the fit. Lower values imply a better fit. The listed values of obtained atmospheric parameters are given at $\log \tau = 0$. Positive values of $B_{grad}$ and $V_{grad}$ indicate increasing values with optical (and geometrical) depth. The values on Table 4.6 are given with the standard error estimates (Press et al. 1992).

Table 4.6: Parameters derived from the inversions

| Data | $\alpha$ | $B^{\star}$ (G) | $B_{grad}$ (G/$\log \tau$) | $V^{\star}_{los}$ (km/s) | $V_{grad}$ (kms$^{-1}$/$\log \tau$) | $V_{mic}$ (km/s) | $V_{mac}$ (km/s) | $\chi^2_{red}$ |
|---|---|---|---|---|---|---|---|---|
| Weak | 0.10 | $1495 \pm 230$ | $123 \pm 92$ | $2.46 \pm 0.30$ | $1.62 \pm 0.33$ | $1.40 \pm 0.06$ | $1.46 \pm 0.05$ | 2.94 |
| Mid1 | 0.12 | $1491 \pm 198$ | $132 \pm 78$ | $2.50 \pm 0.25$ | $1.56 \pm 0.26$ | $1.37 \pm 0.03$ | $1.35 \pm 0.04$ | 3.38 |
| Mid2 | 0.14 | $1531 \pm 204$ | $117 \pm 80$ | $2.43 \pm 0.25$ | $1.68 \pm 0.28$ | $1.35 \pm 0.05$ | $1.13 \pm 0.17$ | 3.43 |
| Mid3 | 0.14 | $1674 \pm 215$ | $118 \pm 88$ | $2.48 \pm 0.25$ | $2.00 \pm 0.33$ | $1.22 \pm 0.05$ | $1.02 \pm 0.21$ | 4.39 |
| Strong | 0.18 | $1681 \pm 188$ | $156 \pm 76$ | $2.24 \pm 0.22$ | $1.81 \pm 0.28$ | $1.22 \pm 0.04$ | $1.04 \pm 0.05$ | 4.31 |

$[\star]$(at $\log \tau = 0$)

It is interesting to note that the magnetic field strength increases only by 12.5% from weak to strong profiles. This means that the main difference between weak and strong profiles manifests itself in the magnetic filling factor $\alpha$, which changes by roughly a factor of 2, which is also roughly the range in Stokes $V$ amplitudes of the binned profiles. The relatively limited range of filling factors sampled by these data is due to the weakness of the 5380.3 Å Stokes $V$ profile and signal to noise value, which makes it a difficult diagnostic to apply to the magnetic regions in the quieter parts of the Sun, at least when observed with a relatively small telescope. Additionally, both, $v_{mic}$ and $v_{mac}$ are decreasing with increasing Stokes $V$ signal i.e. temperatures. Other parameters ($v_{los}$ and $v_{grad}$) do not show a clear dependence on the strength of the $V/I_c$ signal. The values in Table 4.6 indicate that $v_{los}$ becomes zero somewhat above $\log \tau = -1$. The model maintains $v_{los}$ at zero at all heights above that level. There is obviously some cross-talk between $\alpha$ and B (e.g. from Mid 2 to Mid 3, $\alpha$ does not increase, but B does). This is not surprising because of the fact that all the lines considered here have Landé factors around unity. Given that, it is actually surprising that B is obtained at the quoted accuracy ($\pm 200\,G$). The potential cross-talk between B and $B_{grad}$ (similarly between $v_{los}$ and $v_{grad}$) is held in check by the fact that the values of the gradients are constrained by the Stokes V asymmetry. Stratification
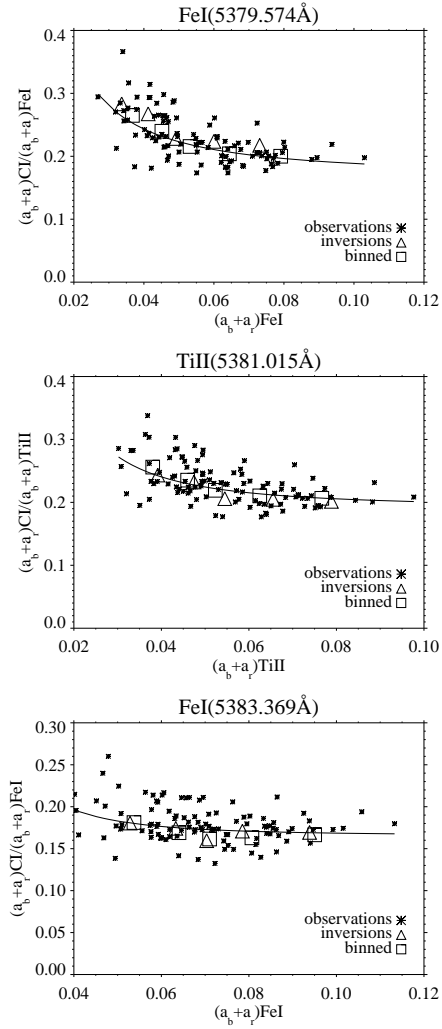
Figure 4.16: Stokes *V* amplitude ratios. The ratios of C I to Fe I$_b$, Ti II and to the Fe I$_r$ are presented on the top, middle and bottom panel respectively. Stars present the amplitude ratios of individual observed Stokes $V/I_c$ profiles, triangles represent the amplitude ratios of synthetic profiles and squares represent the amplitude ratios of the binned observed profiles. The solid lines are the power law fits to the individual observations (stars).
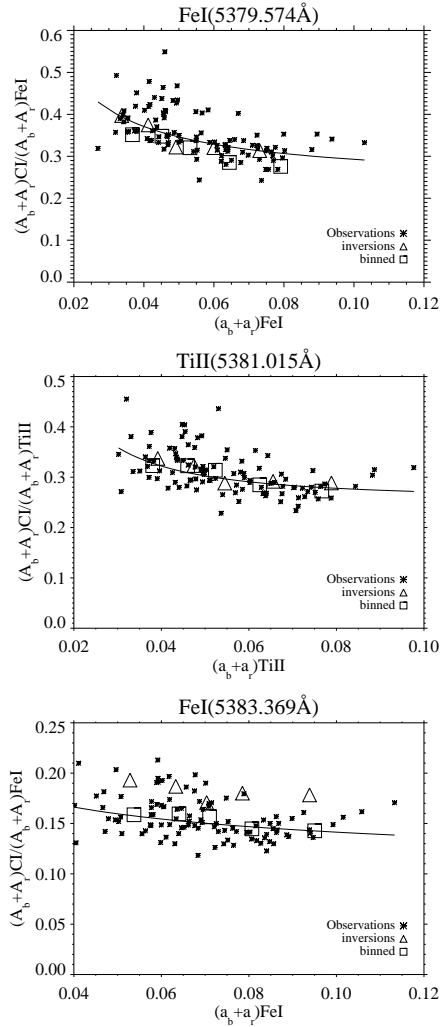
Figure 4.17: Stokes *V* area ratios. The ratios of C I to Fe I$_b$, Ti II and to the Fe I$_r$ are presented on the top, middle and bottom panel respectively. Stars present the area ratios of individual observed Stokes $V/I_c$ profiles, triangles represent the area ratios of synthetic profiles and squares represent the area ratios of the binned observed profiles. Solid lines represent the power law fits to the individual observations.

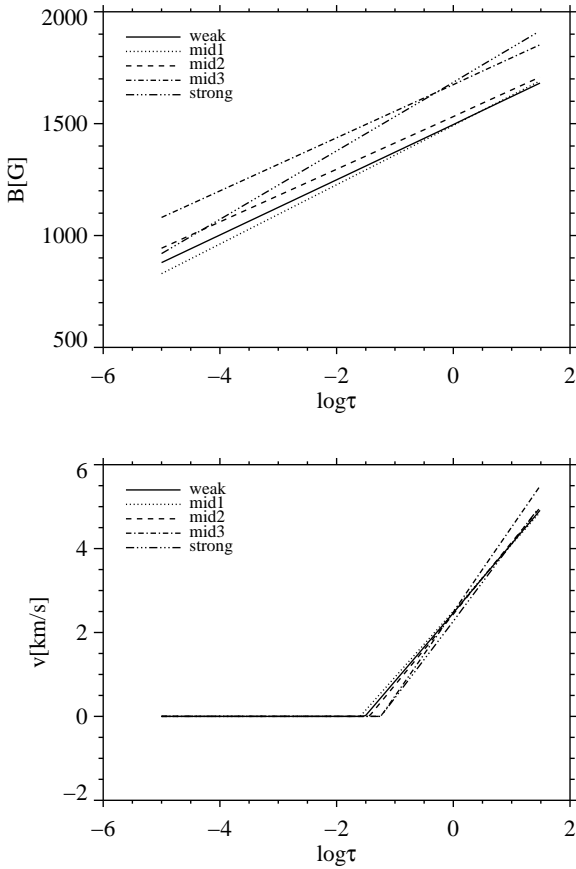of B and $v_{los}$ are presented in Fig. 4.18.



Figure 4.18: Magnetic field strength (top panel) and line-of-sight velocity ($v_{los}$) stratifications of the atmospheres in the magnetic component.

## 4.4.2  Temperature structure derived from inversions

The temperature stratification for the magnetized atmospheric component obtained from the inversion of the 5 binned profiles is presented in Table 4.7 and in the top panel of

Fig. 4.19. The values in Table 4.7 are given with the standard error estimates (Press et al. 1992). The temperature at $\log\tau = 0$ deduced from Stokes $V$ profiles drops from over 6800 K to under 6600 K from the weak Stokes $V$ signal to the strong one. These temperatures imply continuum intensity contrast values at 5380 Å in the magnetic elements of 0.07 and 0.05, respectively, which are significantly larger than the granulation contrast determined as the standard deviation of quiet Sun continuum intensity along the slit (=0.0125 for our data). A similar trend of decreasing temperature with increasing $V$ amplitude can also be observed at $\log\tau = -0.5$ and $-1.0$. The convergence of the temperature stratifications to a single value at $\log\tau = -3$ is due to the prescription of a single value for all inversions at that level. This is driven mainly by the Fe I 5383.4 Å line, which requires a low temperature in the upper photosphere, in order to maintain its depth also in the magnetic features. For the profiles representing the weak bin (small filling factor) in Fig. 4.15, all lines look similar to the flat-field profiles in Fig. 4.14). We believe that this low temperature of the magnetic features in the upper photosphere is not real, but is rather an artifact of modeling the 5383.4 Å line in LTE, although its core is expected to form in NLTE and its source function to be largely decoupled from temperature (Bruls and Solanki 1993). Figure 4.16 shows the Stokes $V$ amplitude ratios $r$ (Eq. 4.4) of the individual observed profiles, as well as the $r$ values obtained from binned profiles ($r$ of the binned profiles logically lie amidst the individual measurements). Ratios $r$ of the synthetic profiles are overplotted. Power law fits, applied to the individual observations, are represented by solid lines in Fig. 4.16. The good agreement seen in Fig. 4.16 is a confirmation that the best-fit synthetic profiles reproduce the Stokes $V$ amplitudes with significant accuracy. Note that these line ratios were not employed to constrain the inversions. Given the 10% relative accuracy of the fits to the $V$ profiles (see Fig. 4.15), this agreement is rather encouraging.

The Stokes $V/I_c$ amplitude ratios decrease with increasing Stokes $V$ amplitude of the spectral line (i.e. with stronger Stokes $V/I_c$ signal). Given that the C I line strengthens with increasing temperature (Livingston et al. 1977, Elste 1987, Holweger and Müller 1974, Solanki and Brigljević 1992, cf. Sect. 4.3.2) while the other 3 lines tend to weaken (i.e. their $V$ amplitudes drop or remain roughly the same, see Fig. 4.12), a decrease in the plotted Stokes $V$ line ratios implies a decrease in temperature in the lower layers of the magnetic elements with increasing $V$ amplitude (in agreement with the results of Solanki and Brigljević 1992).

The retrieved temperature stratification of the atmospheres for the binned data are presented in Fig. 4.19 with the reference atmosphere HSRASP (top panel) and with NET S86, PLA S86, PLA SB92 atmospheres (bottom) which will be explained later on in Sect. 4.4.3.

Top panel of Fig. 4.19, shows how much the temperature stratification of our magnetic atmosphere differs from the HSRASP atmosphere. The higher temperature stratification obtained from the magnetic structures show us that the observed magnetic structures are hotter with less steep temperature gradient than their environment. We also see that the magnetic structures with weak signal are formed in the hottest atmosphere, which means that the smaller structures with little Stokes $V$ signals are formed in the hotter regions than the structures with stronger Stokes $V$ signals.

To compare the temperatures retrieved from the inversions with the quantities defined in Sect. 4.1.2, we need to identify the height of maximum response of the individual spectral lines to temperature. Therefore RFs to perturbations in temperature are calculated at
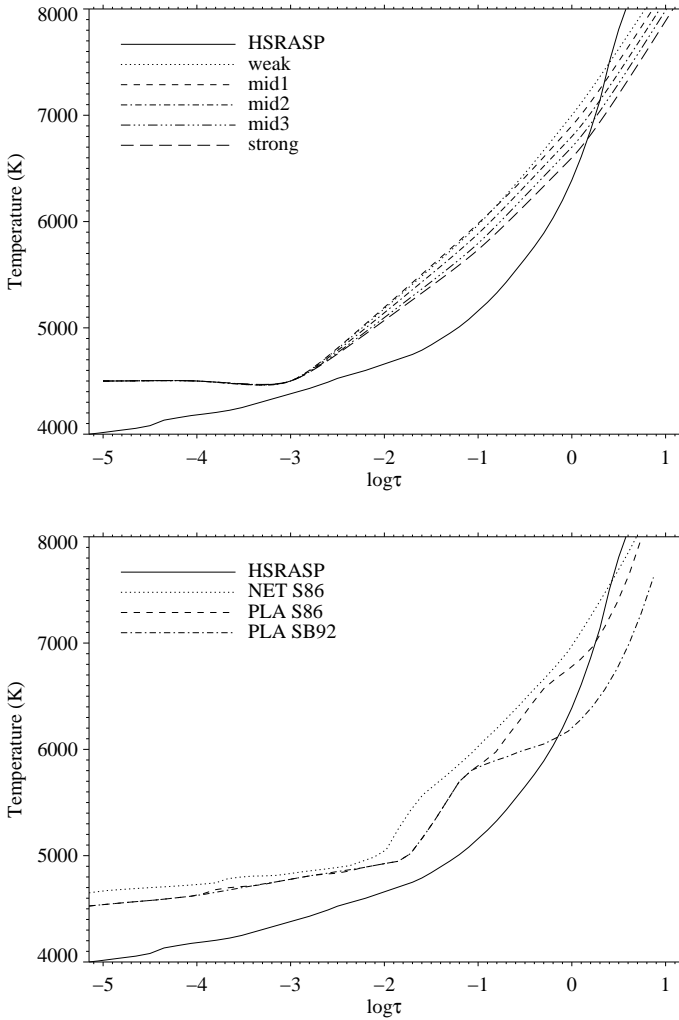
Figure 4.19: Temperature stratification of the atmospheres in the magnetic and the field-free (quiet Sun) components. The temperature stratifications of the atmospheres providing best fits to the 5 binned Stokes profiles of the analyzed data set are presented in the upper panel. Temperature stratification of 3 empirical flux-tube models in the literature are presented in the lower panel. The solid curve displays the temperature stratification of the quiet Sun (HSRASP) and is identical in both frames.

Table 4.7: Temperatures obtained from the inversion of 5 binned profiles. HSRASP temperatures are given as a reference.

| Mean Data | Temperature (K) | | | | |
|---|---|---|---|---|---|
| | $\log \tau = 0$ | $\log \tau = -0.5$ | $\log \tau = -1$ | $\log \tau = -3^*$ | $\log \tau = -4^*$ |
| Weak | $6826 \pm 132$ | $6434 \pm 82$ | $5969 \pm 45$ | 4500 | 4500 |
| Mid1 | $6746 \pm 114$ | $6383 \pm 73$ | $5926 \pm 40$ | 4500 | 4500 |
| Mid2 | $6575 \pm 108$ | $6239 \pm 69$ | $5814 \pm 14$ | 4500 | 4500 |
| Mid3 | $6657 \pm 110$ | $6266 \pm 65$ | $5782 \pm 34$ | 4500 | 4500 |
| Strong | $6580 \pm 93$ | $6206 \pm 56$ | $5752 \pm 29$ | 4500 | 4500 |
| HSRASP | 6390 | 5650 | 5160 | 4380 | 4175 |

$*$ *fixed*

the position of maximum Stokes $V$ amplitudes, using the atmospheres returned from the inversions. The center of gravity (COG, Semel 1970, Rees and Semel 1979) of these RFs are determined according to,

$$COG = \frac{\int RFz\,dz}{\int RF\,dz} \, , \qquad (4.15)$$

where z is the height in km. In Fig. 4.20, calculated RFs at the maximum Stokes $V$ signal of the spectral lines in the atmospheres obtained from weak and strong data are presented with the COG location for each spectral line. Obtained COG temperatures ($T_{COGs}$) are presented versus amplitude sums of the spectral lines in Fig. 4.21. The $T_{COGs}$ at the maximum of Stokes $V/I_c$ signal decrease with increasing signal from weak to the strong data. We see maximum change in temperature with Stokes $V$ signal in the carbon line, while the least change is seen in the Fe I$_r$ line. Surprisingly the temperature change in the Ti II line is as strong as in the carbon line. Therefore, the line ratio of these two lines cannot represent the temperatures, but the ratios of C I to the two iron lines will be sensitive to the temperatures. To see the relation between amplitude ratios and the temperature ratios, we calculated $T_{COG}$ ratios of carbon to the other lines. The relations are presented in Fig. 4.22. Here the gradients seen in the iron lines are increasing with increasing amplitude ratios, while there is no trend in the titanium line. The relations between temperature ratios and amplitude ratios are the consequence of our fixed temperature nodes.

The relation between amplitude ratios and temperatures are presented with $T_{COGs}$ of the carbon line in the left panel of Fig. 4.23 and with the $T_{COGs}$ of the lines at the right panel of Fig. 4.23. The linear relation between these two quantities proves the concept of using the amplitude ratios as a tool to determine the temperatures within the unresolved flux tubes directly from the Stokes $V$ profiles. Since the C I line is thermophile in this set of lines, the temperature changes are seen better in this line. Additionally, we have found that the Ti II line is temperature sensitive. Therefore, we see similar trend in the middle panels of Fig. 4.23. On the right panel of Fig. 4.23, it is clear that the observed temperature differences on the lines are very low for the Fe I$_b$ and Fe I$_r$ lines. If we compare Ti II and C I lines, in Ti II line we see lower $T_{COGs}$ than in the C I but the variation is as

high as seen in the carbon line. Therefore in this line we don't see any relation between temperature ratios and amplitude ratios. But in Fig. 4.16 we see decreasing amplitude ratios with increasing magnetic filling in the titanium line. The reason can be that the titanium line ratios are indicating magnetic flux variations instead of temperatures.
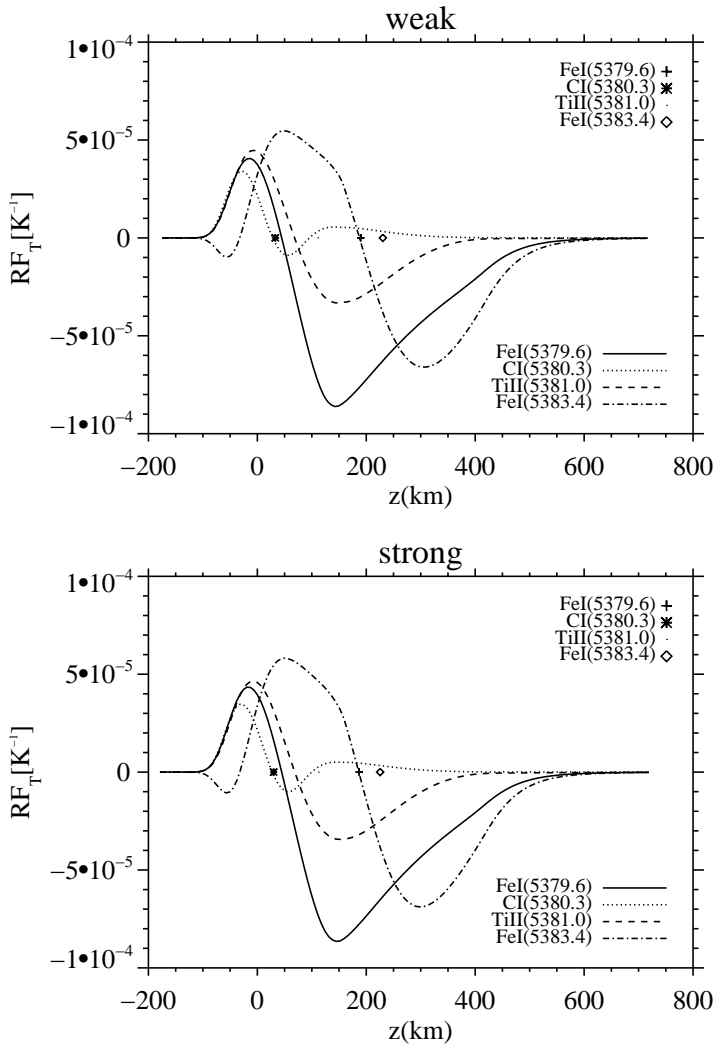
Figure 4.20: $RF_T$'s at maximum Stokes $V$ signal of the spectral lines of weak data and of strong data. $RF_T$'s are represented with lines coded to lower legend and COG locations are represented as symbols coded to upper legend.
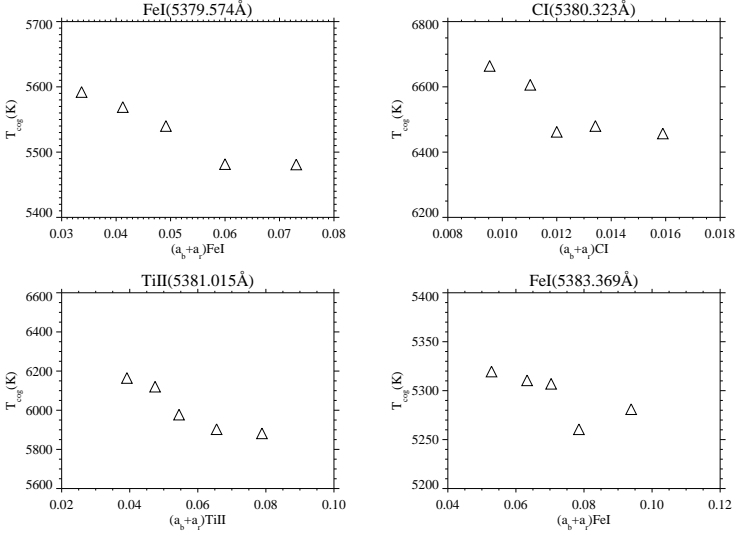
Figure 4.21: Obtained temperatures of the binned profiles. Temperatures returned from the inversions are presented as a function of Stokes V amplitude sums. Temperatures (at $\log \tau = 0$) of the binned profiles of Fe I (5379.5 Å), C I (5380.3 Å), Ti II (5381.0 Å) and Fe I (5383.4 Å) are presented from top left to bottom right panels respectively.

Figures 4.22 and 4.23 shows that the Stokes $V$ amplitude ratios can be used to study temperature ratios and temperatures of the unresolved magnetic structures in carefully selected lines. A factor of 2 difference in magnetic flux density implies a temperature difference of $\approx 250\,$K at the continuum forming layers (Table 4.7).
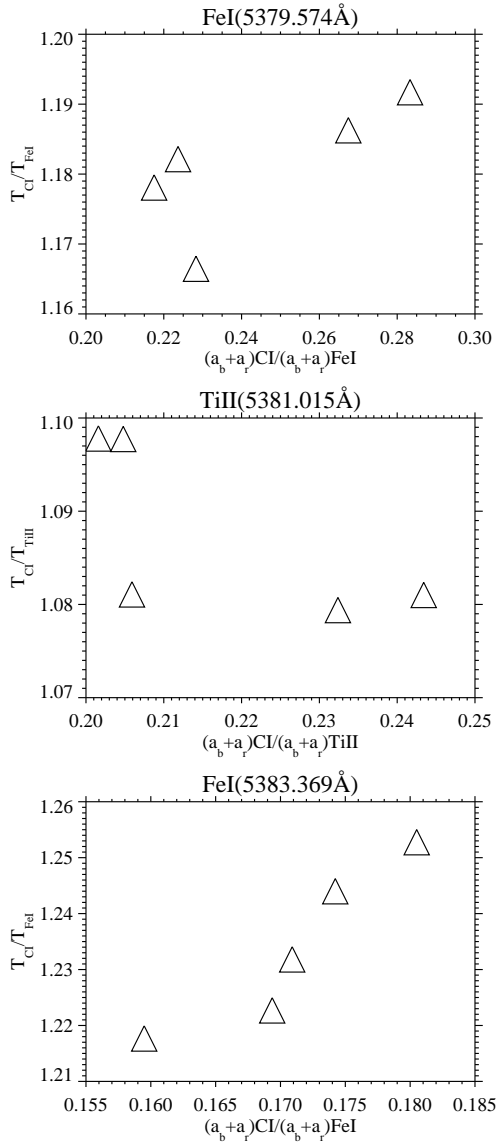
Figure 4.22: Temperature ratios as a function of amplitude ratios. Temperature ratios of C I to Fe I$_b$, to Ti II and to Fe I$_r$ are presented from top panel to the bottom panel, respectively.
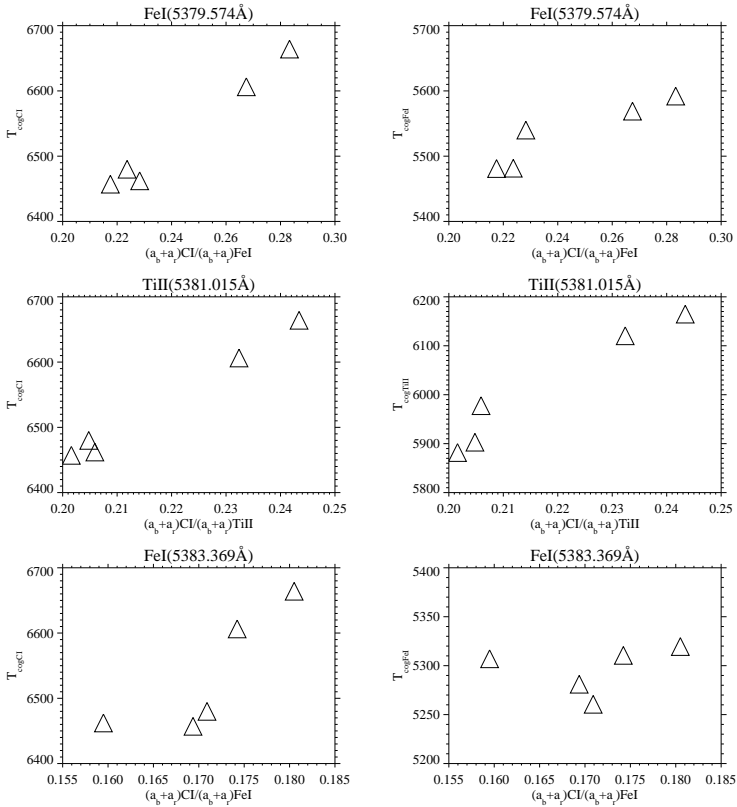
Figure 4.23: Temperatures as a function of amplitude ratios. Left panel represents $T_cog$ of C I line as a function of amplitude ratio of C I to Fe I$_b$, to Ti II and to Fe I$_r$ from top panel to the bottom panel respectively. Right panel represents $T_cog$ of spectral lines as a function of amplitude ratio of C I to Fe I$_b$, to Ti II and to Fe I$_r$ from top panel to the bottom panel respectively.

### 4.4.3   Tests using existing atmospheric models

In this section we partly repeat the analysis of the previous section, but now using 3 existing atmospheric models, one describing flux tubes in the network (in the following denoted NET S86, Solanki 1986), the corresponding plage flux-tube model (denoted PLA S86, Solanki 1986) and the revised plage flux-tube model (PLA SB92, Solanki and Brigljević 1992). The temperature stratifications of these existing atmospheres are presented in the lower panel of Fig. 4.19. The inversions for this comparison were set up in a similar way as the inversions described in Sect. 4.4, with the exception that the temperature in the magnetic component is prescribed. The HSRASP is again used as the non-magnetic component atmosphere with $\log(gf)$, $v_{mac}$ and $v_{mic}$ determined from the mean flat-field profile. For the magnetic component we used the models NET S86, PLA S86 and PLA SB92 to invert the mean data sets. We kept the temperature stratification of each of the atmospheres unchanged during the inversion. The other parameters ($B$, $B_{grad}$, $v_{los}(\tau = 1)$, $v_{grad}$, $v_{mic}$ and $v_{mac}$) were left free as in the inversions presented in Sect. 4.4. Profiles calculated with NET S86, PLA S86 and PLA SB92 are presented in Fig, 4.24. Obtained amplitude ratios are presented in Fig. 4.25.
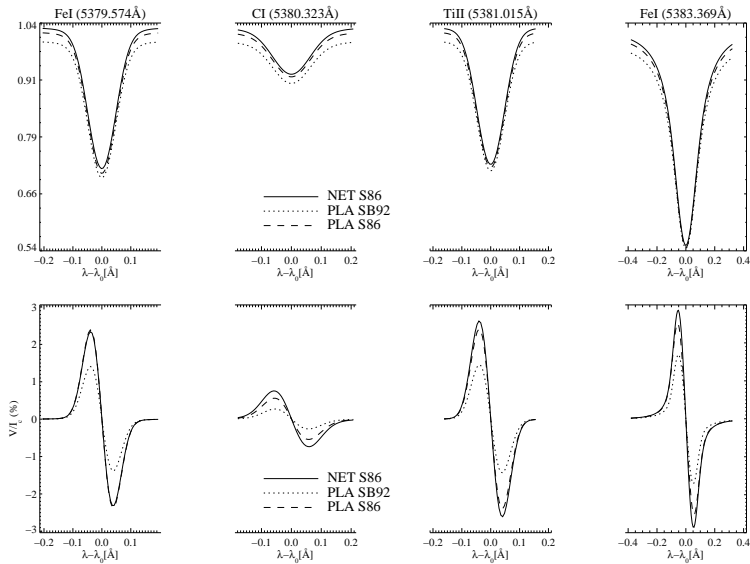


Figure 4.24: Synthetic profiles from forward calculations with existing atmospheric models. Top panel represents the Stokes $I/I_c$ and bottom panel represents the Stokes $V/I_c$ signals.

Figure 4.25 compares the line ratios obtained from these existing tabulated atmospheres with the observations. According to the test results, the PLA S86 model atmo-

sphere in general represents the observations better than the other model atmospheres, although it reproduces the ratios involving Fe I (5383.4 Å) relatively poorly except for the weakest binned profile. This result was expected since the temperature stratification of this model atmosphere is the closest one to the temperature stratifications obtained from the inversions (compare Fig. 4.19 upper and lower panels). With the coolest temperature stratification in the deep layers of the atmosphere, the PLA SB92 model comes closest to reproducing the line ratios of the mid3 and the strong binned profiles. With its hotter temperature stratification the NET S86 model atmosphere is most closely consistent with weak binned profiles, especially with regard to the ratios involving the Ti II line, but appears to be too hot even for these. This atmosphere was originally constructed to reproduce network, enhanced network data with a magnetic filling factor of $\approx 6\%$, which suggests that at lower filling factors than considered here the magnetic elements are hotter still in their deep layers.
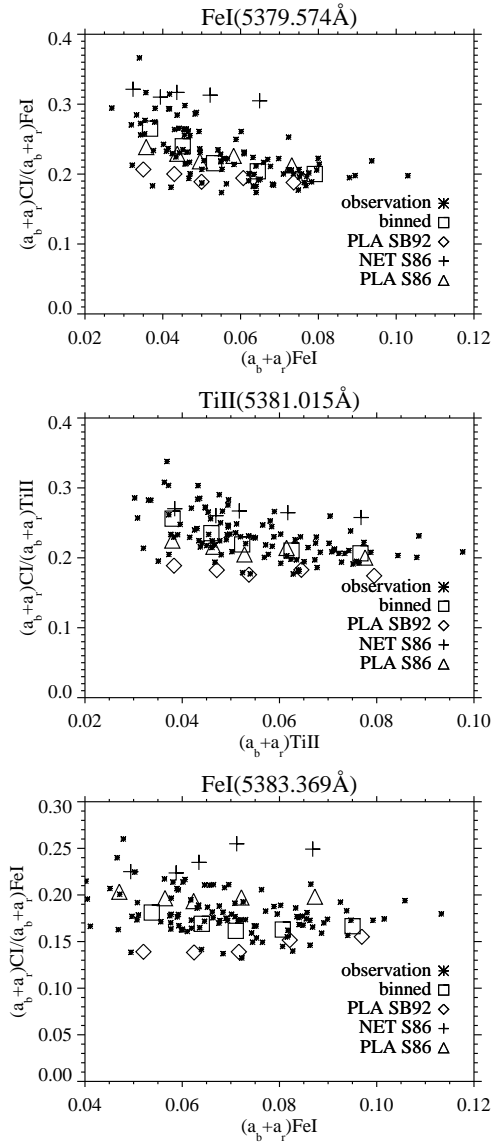
Figure 4.25: Stokes *V* amplitude ratios: comparisons of observations with model atmospheres. Top panel: C I to Fe I$_b$ ratio, middle panel: C I to Ti II ratio and bottom panel: C I to Fe I$_r$ ratio.

# 5 Analysis of radiative MHD snapshots

3-D magnetohydrodynamic (MHD) simulations with the necessary physics (compressibility, non-grey, LTE, radiative energy transport, partial ionization) to treat the uppermost part of the convection zone and the photosphere can be comparable with the observations. 3-D MHD snapshots calculated by the MURaM code (Sect. 5.1) are studied to validate and calibrate the diagnostic as well as to test our inversion results. Also, by comparing Stokes $V$ line ratios, as described in Sect. 5.3.1, from the simulations with the observations, the thermal structure of the magnetic features in the simulations can be tested. Synthetic data (Sect. 5.2) are calculated with the atmospheres provided by the MHD snapshots and then degraded to our observational conditions (Sect. 5.3.1). Amplitude ratios of both degraded and original resolution data are calculated and the temperatures at the center of gravity (Eq. 4.15) heights of RFs at maximum Stokes $V$ signals are extracted from the atmospheres as explained as in Sect. 4.4.2. A comparison of the results with the observations and the inversions is presented.

## 5.1 MURaM snapshots

The MURaM (MPS/University of Chicago Radiative MHD) code (Vögler 2003); Vögler and Schüssler (2003); Vögler et al. (2005) solves the time-dependent MHD equations for a compressible and partially ionized plasma including non-grey LTE radiative transfer based on multi-group frequency binning. Three of the computational boxes analyzed in this thesis correspond to a small part of a unipolar plage region on the Sun. The boxes extend 1400 km in the vertical direction (roughly covering the range between 800 km below to 600 km above the visible solar surface) and 6000 km in both horizontal directions corresponding to an area of 8.28×8.28 arcsec$^2$, with a grid spacing of 14 km and 21 km, respectively. The box is penetrated by a fixed amount of vertical magnetic flux corresponding to an average vertical magnetic field strength (magnetic flux) of 50 G, 200 G and 400 G respectively. A fourth simulation run represents the quiet Sun. This run is a mixed polarity run, extending 1680 km in the vertical direction and 6000 km in both horizontal directions, with a grid spacing of 14 km and 21 km, respectively. The mean unsigned vertical field in this case was 9 G. For each 3D position in the simulation, the quantities listed in Table. 5.1 can be extracted. Temperature, $V_z$ and $B_z$ at $\log \tau = 0$ of the studied data cubes are presented in Fig. 5.1.
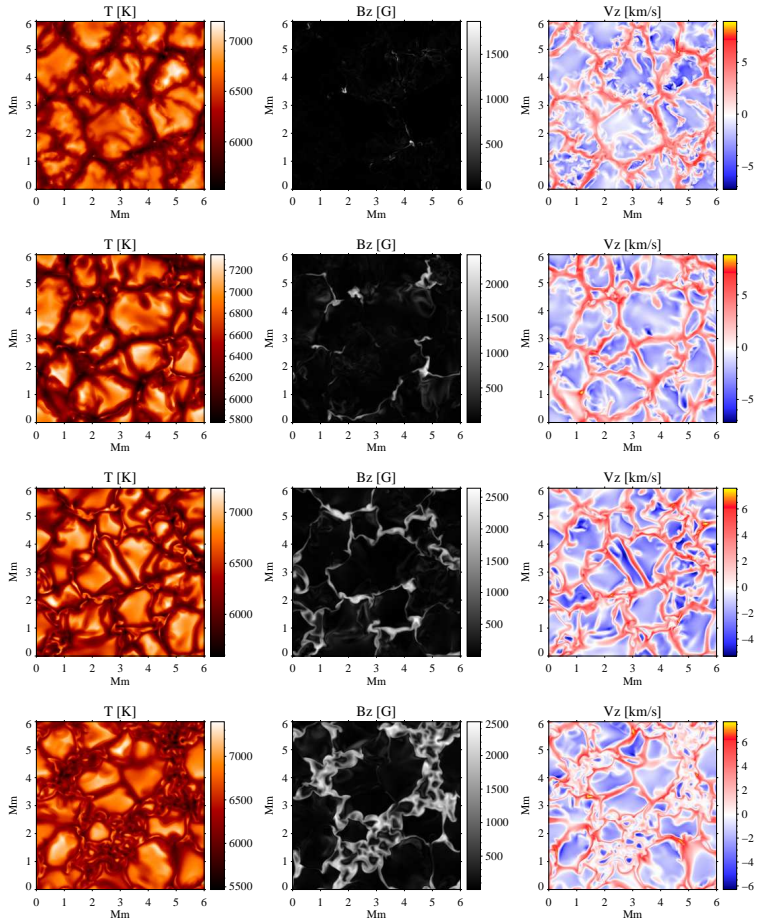
Figure 5.1: Temperature, $B_z$ and $V_z$ of the snapshots at $\log \tau_{5000\text{Å}} = 0$. From top to bottom $\langle |B| \rangle$=9 G, $\langle B \rangle$=50 G, $\langle B \rangle$=200 G, and $\langle B \rangle$=400 G.

Table 5.1: Output quantities of the MURaM code

| Parameter | Abbreviation and Unit |
|---|---|
| Temperature | $T$[K] |
| Pressure | $P$[g/cms$^2$] |
| Horizontal velocity components | $V_x$, $V_y$ [cm/s] |
| Vertical velocity component | $V_z$ [cm/s] |
| Internal energy per unit volume | [erg/cm$^3$] |
| Horizontal magnetic field components | $B_x$, $B_y$ [G] |
| Vertical magnetic field component | $B_z$ [G] |

Properties of the studied MHD snapshots are:

- $\langle | B | \rangle$=9 G (mixed polarity region with $576 \times 576$ grid points at horizontal directions and 120 grid points in depth)

- $\langle B \rangle$=50 G (unipolar region with $288 \times 288$ grid points in the horizontal directions and 100 grid points in depth)

- $\langle B \rangle$=200 G (unipolar region with $288 \times 288$ grid points in the horizontal directions and 100 grid points in depth)

- $\langle B \rangle$=400 G (unipolar region with $288 \times 288$ grid points in the horizontal directions and 100 grid points in depth)

## 5.2 Synthetic profiles

In order to compare the results obtained from observations and inversions with the MHD snapshots, STOPRO routines were used to synthesize Stokes $I/I_c$ and Stokes $V/I_c$ profiles of the spectral lines with the atmospheres calculated by the simulations. The necessary input quantities used by the STOPRO code to synthesize Stokes profiles are presented in Table. 5.2. In order to obtain physical quantities, which are not provided by the MURaM code (compare Table 5.1 and Table 5.2), the MODCON (Solanki 1987) subroutine was used. This code computes the ionization equilibrium for a given chemical composition, electron pressure $P_e$, continuum absorption coefficient $\kappa_\lambda$ and determining continuum optical depth $\tau_\lambda$. It employs routines due to Gustafsson (1973). As an example, the resulting continuum intensities at 5380 Å of different snapshots are presented in Fig. 5.2. Magnetograms are calculated from the maximum Stokes $V$ signals of each spectral line per snapshot and presented in Fig. 5.3. For further analysis, only snapshots with $\langle B \rangle = 50, 200, 400$ G are used, while the $\langle | B | \rangle$=9 G snapshot is only used for the determination of the spatial filter, which is explained in Sect. 5.3.1.

Average Stokes $I$ and Stokes $V$ profiles were calculated from the $\langle B \rangle = 50, 200, 400$ G snapshots in order to see if we will have similar Stokes $V$ signal as binned data (weak, mid1, mid2, mid3, strong) from the observations. These averaged profiles are presented in Fig. 5.4. Comparing these profiles with the observed profiles in Fig. 4.10, one can already see that the $\langle B \rangle$=200 G snapshot represents our observations best. The Stokes profiles from the observations agree reasonably well with the profiles computed from the MHD

Table 5.2: Input quantities required by STOPRO routine.

| Parameter | Abbreviation and Unit |
|---|---|
| Continuum optical depth | $log\tau$ |
| Height | $z$ [cm] |
| Temperature | $T$ [K] |
| Gas pressure | $P$ [g/cms$^2$] |
| Electron pressure | $P_e$ [g/cms$^2$] |
| Continuum absorption coefficient | $\kappa$ [g$^{-1}$] |
| Mass density | $\rho$ [gr/cm$^3$] |
| Magnetic field strength | $B$ [G] |
| Micro-turbulence velocity | $v_{mic}$ [cm/s] |
| Line-of-sight velocity | $v_{los}$ [cm/s] |
| Angle between $B$ and LOS | $\gamma$[deg] |
| Azimuthal angle of $B$ | $\chi$[deg] |

cubes, except for the Stokes V profile of Fe I r. There, the observed Stokes V signal is approximately 1.5% weaker than the synthesized signal. The reason for this discrepancy is investigated by performing the following test: RFs to temperature perturbations are calculated with the atmospheres of each snapshot. The RFs showed that almost all pixels of $\langle B \rangle$=50 G, many pixels of $\langle B \rangle$=200 G and some pixels of $\langle B \rangle$=400 G snapshots do not cover all the higher part of the photosphere, where this line has significant response (cf. Fig. 4.12). This situation makes this iron line not suitable for the analysis with the MURaM snapshots. For this reason, this line is excluded from our further analysis.

For further comparison with the observations, we compute the amplitude ratios for the synthetic data. Since the synthetic data are free of noise, we can compute amplitudes of the blue and the red lobe of the Stokes V profiles simply by taking the minimum and maximum of the profile. Later on, amplitude ratios of carbon to the other lines are calculated for the synthetic data of each snapshot, which are presented in Fig. 5.5. The scatter plots in Fig. 5.5 are dominated by the small Stokes V amplitude signals. To avoid quiet regions in the snapshots with low magnetic flux, the plotted relations are restricted to regions with $B > 1000$ G. This threshold is also consistent with the results obtained from the inversions (see Table. 4.6), since we also had a threshold on the observed Stokes V signals (see Sect. 4). This selection also makes the determination of the trends easier. The amplitude ratios with this selection are presented in Fig. 5.6. For the $\langle B \rangle$=50 G snapshot power law relation is reasonable between amplitude ratios and amplitude sums, which can be used as a proxy for the magnetic filling factor (see Sect. 4.1.1). In the $\langle B \rangle$=200 G snapshot for the iron line we see decreasing amplitude ratios with increasing magnetic filling, where we see opposite trend in titanium line. In the $\langle B \rangle$=400 G snapshot, there is no relation seen in the iron line but linear trend is present in the titanium line.
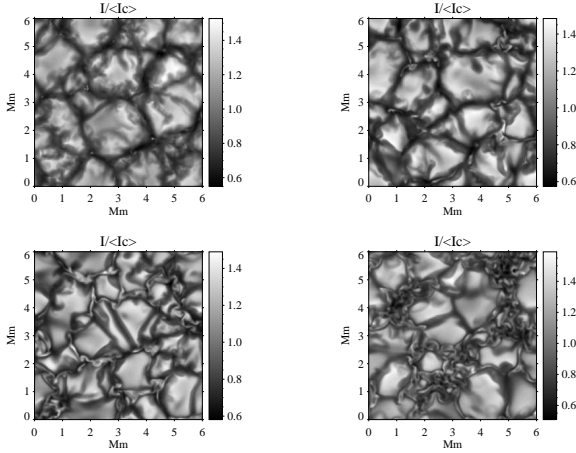
Figure 5.2: Continuum intensities st 5380 Å for the snapshots $\langle|B|\rangle$=9 G, $\langle B\rangle$=50 G, $\langle B\rangle$=200 G, $\langle B\rangle$=400 G, from left to right respectively.

## 5.3 Temperatures derived from the simulations

We determined $T_{COGs}$ (Sect. 4.4.2) and amplitude ratios (Sect. 4.1.2) of the spectral lines for each cube in order to retrieve the relations between amplitude ratios with both, temperature ratios and temperatures. These relations are presented in Fig. 5.7. The left panel of Fig. 5.7, shows that the plot is dominated by the features with low amplitude values, corresponding to low magnetic field strength. At low magnetic flux regions, the scatter is large since the structures are from quiet regions of the snapshots, which we exclude in the analysis of the observations (See Sect. 4). For the analysis of the observations we selected the data with a Stokes $V$ signal of carbon 3 times greater than the noise level. This means that no quiet Sun data was included in our previous analysis. Therefore it is difficult to compare the relations between amplitude ratios temperature and amplitude ratio temperature gradients from the whole snapshot with the observations. Additionally, the results obtained from the inversions indicate that the observed region has a magnetic field strength of 1500−1700 G. Therefore, we exclude the pixels with $B < 1000\,G$ regions at $\log \tau = 0$ from the investigation of the relations since they are not representative of the observations (Fig. 5.7, right panel). With this selection, the relation between amplitude ratios with temperatures and temperature gradients becomes more clear.

The relation between temperatures and amplitude ratios of the snapshots are presented in Fig. 5.8 in the regions with $B > 1000\,G$. In all snapshots, linear correlations are reasonable between temperatures and amplitude ratios of C I to Fe I$_b$ and to Ti II.

In Fig. 5.9, temperature ratios are presented as a function of amplitude ratios in the regions with $B > 1000\,G$. Power law relations are reasonable for all snapshots. For the
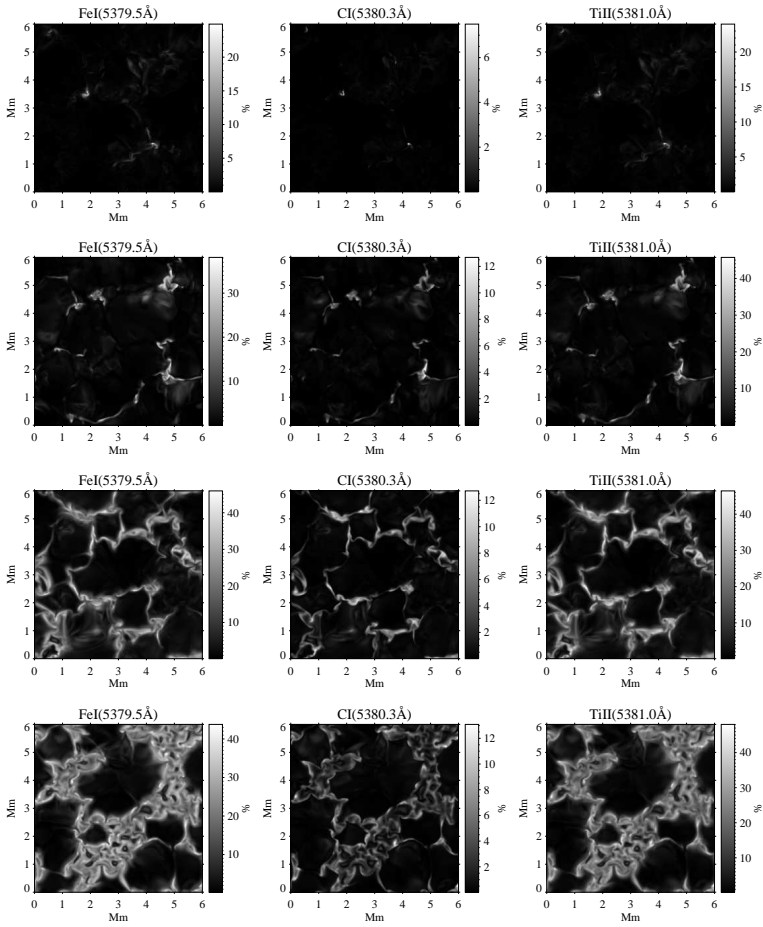
Figure 5.3: Magnetograms of the spectral lines at the snapshots $\langle|B|\rangle$=9 G (top panel), $\langle B\rangle$=50 G (second row from the top), $\langle B\rangle$=200 G (third row from the top), $\langle B\rangle$=400 G(bottom row).
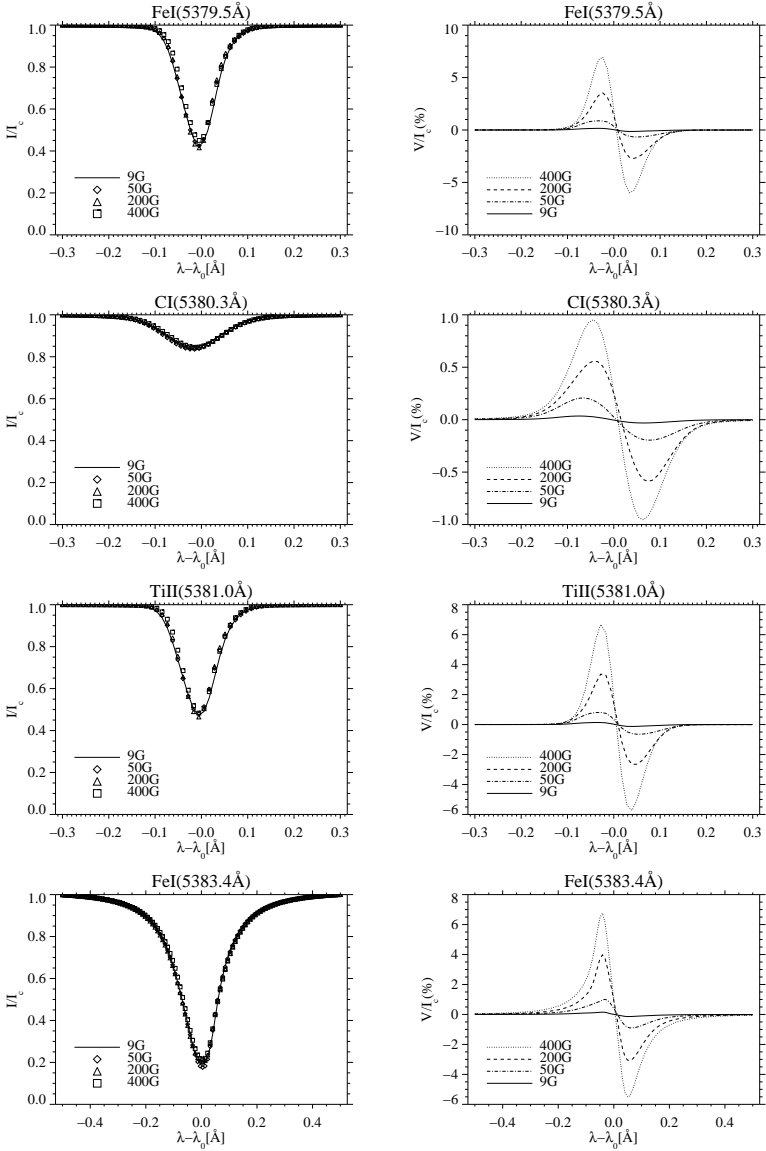
Figure 5.4: Average spectral line profiles in each snapshot. Intensities are presented on the left column and Stokes $V/I_c$ profiles are presented on the right column.
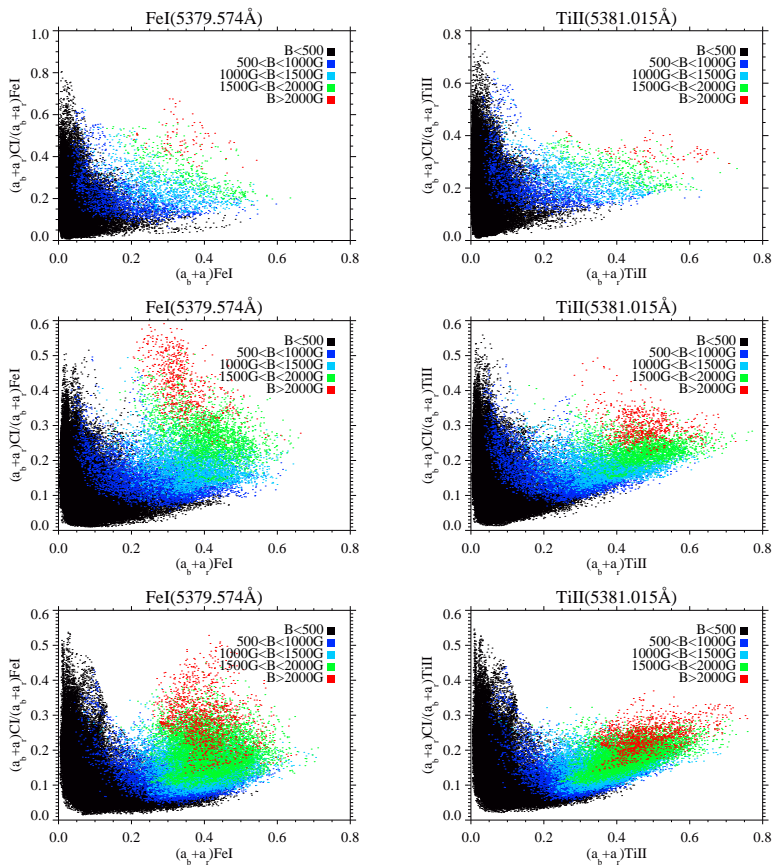
Figure 5.5: Amplitude ratios of carbon to the other lines at $\langle B \rangle = 50\,\mathrm{G}$ (upper row), $\langle B \rangle = 200\,\mathrm{G}$ (center row), and $\langle B \rangle = 400\,\mathrm{G}$ (lower row) the snapshots respectively.
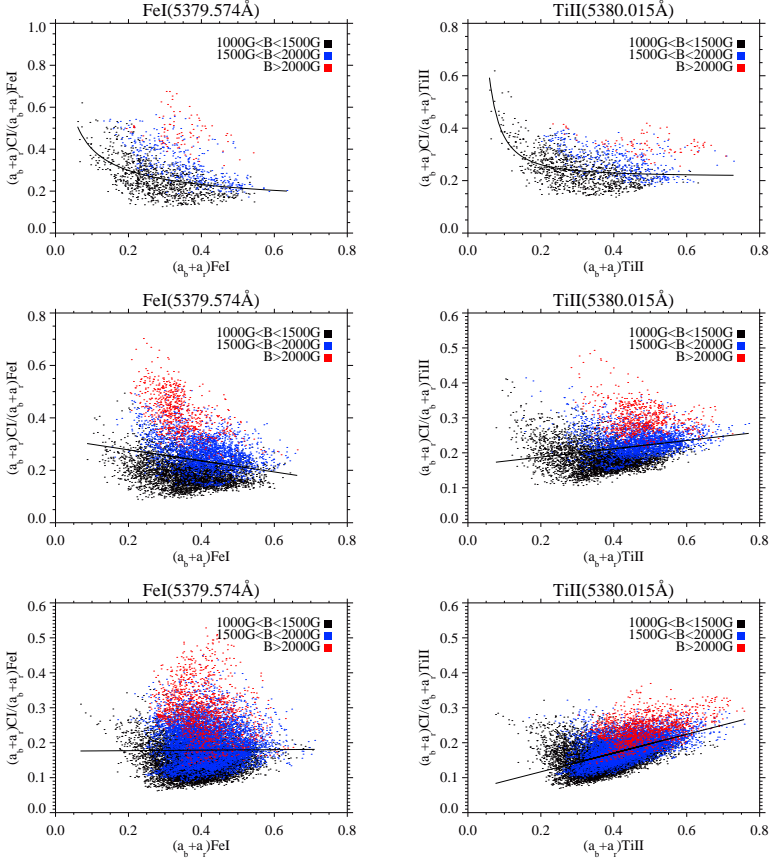
Figure 5.6: Amplitude ratios of carbon to the other lines at $\langle B \rangle = 50\,\mathrm{G}$ (upper), $\langle B \rangle = 200\,\mathrm{G}$ (center), and $\langle B \rangle = 400\,\mathrm{G}$ (lower) respectively excluding regions with $B > 1000\,\mathrm{G}$. Solid lines represent the power law fits for the $\langle B \rangle = 50\,\mathrm{G}$ snapshot and linear fits for both the $\langle B \rangle = 200\,\mathrm{G}$ and $\langle B \rangle = 400\,\mathrm{G}$ snapshots.

$\langle B \rangle = 400$ G snapshot relation is more linear.

Amplitude ratios and temperature relations are presented in Fig. 5.10 from the results of 3 MHD snapshots for regions with $B > 1000$ G. Even though the $\langle B \rangle = 400$ G snapshot dominates the relation with its many more magnetic features with $B > 1000$ G than the other snapshots, plots from all 3 snapshots follow roughly the same relation. This supports the usage of the amplitude ratios as a proxy for temperature. As seen in Fig. 5.10, a linear relation is reasonable both between the $T_{\mathrm{COGs}}$ and the amplitude ratio of C I to Fe I$_{\mathrm{b}}$ line (top panel) and for titanium line (bottom panel). This confirms the fact that the amplitude ratios can be used as a temperature diagnostic tool. Values obtained from inversions of our binned observations are overplotted for illustrative purposes, showing the much broader dynamic range of the original simulations. The small offset of the inversion results, represented by stars in Fig. 5.10 above the mean value probably just reflects their 2 orders of magnitude lower resolution than the simulations. This could well lead to a small offset in a sufficiently inhomogeneous atmosphere, since the spectral lines react non-linearly to temperature changes. Additionally, inversions are not so accurate since a simplistic model is used (Sect. 4.4), and this may cause this offset too.

In Fig. 5.11, temperature ratios are presented as a function of amplitude ratios from the results of 3 original resolution MHD snapshots. Here as previously explained $B > 1000$ G threshold is used. Here again we can say that even though the $\langle B \rangle = 400$ G snapshot dominates the relation with its many more magnetic features in the regions with $B > 1000$ G than the other snapshots, they agree with each other. There is power law relation between the temperature ratios and the amplitude ratios. Here again it is good to emphasize the importance of better statistics with more data points to get a better comparison scheme of the temperature ratios and amplitude ratios.

We should keep in mind that in both cases presented in Fig. 5.10 and in Fig. 5.11 are obtained from the original resolution of the MHD snapshots, not from the degraded data. Therefore the synthetic data with original resolution cannot really represent the observations. Since we cannot degrade the atmospheres, the only way to compare the simulation results with the observation is this.
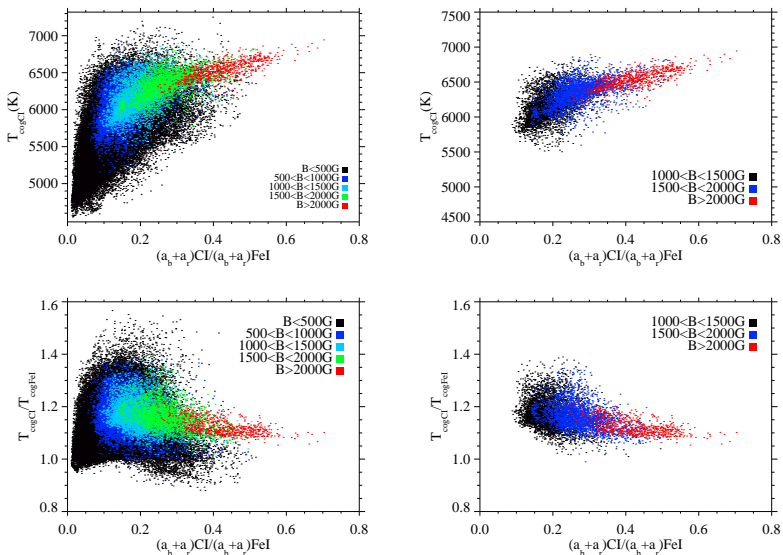
Figure 5.7: Temperatures (top panels) and temperature ratios (bottom panels) vs the amplitude ratios from the MHD snapshot of $\langle B \rangle = 200\,$G (plage region). Left panel represents the results from snapshot and the right panel represents the results in the regions with $B > 1000\,$G.

## 5.3.1   Degrading snapshots to the observational conditions

Since the MHD simulation boxes have high resolution and are not affected by atmospheric turbulence and other observational biases, we need to introduce all those effects to the synthetic profiles, in order to allow a better comparison of the results with our observations. Therefore, we degraded the snapshots both spatially and spectrally. Spatial convolution was done with a 2-D Gaussian filter which has the full width half maximum (FWHM) of the assumed seeing value of 3 " (smallest observed magnetic element) and a 2-D Lorentzian filter with a width determined from comparison of the standard deviation of the continuum intensity of $\langle |B| \rangle = 9\,$G simulations and the observations. This spatial convolution filter is presented in Fig. 5.12, together with the effects of degrading and binning to one of the continuum images in the lower panels of the figure. Spectral convolution was done with a Gaussian filter with a FWHM of the spectral resolution of the observations (Sect. 3.2.1). Finally, we binned the data to the pixel size of the observations.

These degraded data are binned to one average profile. The comparison of these average Stokes $V$ profiles with the ones obtained from the observations is presented in Fig. 5.13. From now on, those convolved and binned data are used for analysis since they are the most representative for the observations. From these data, amplitude ratios
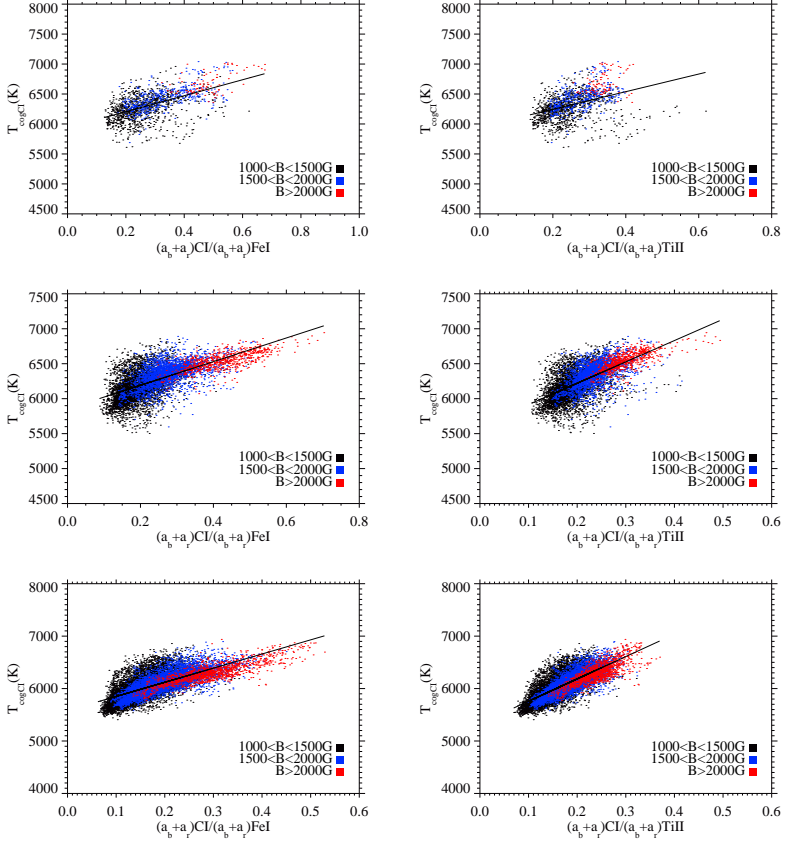
Figure 5.8: Temperatures vs the amplitude ratios in the regions with $B > 1000\,\mathrm{G}$. The left panel represents the results for the iron line, while the right panel represents the results for the titanium line. Top panel is the result from the $\langle B \rangle = 50\,\mathrm{G}$ snapshot, middle panel is the result from the $\langle B \rangle = 200\,\mathrm{G}$ snapshot, and bottom panel is the result from $\langle B \rangle = 400\,\mathrm{G}$ snapshot. Solid lines represent the linear fits.

(Sect. 4.1.2) are calculated for each MHD snapshot and they are presented together with the results of observations and inversions in Fig. 5.14. Here we see that MHD snapshots show the same trend as seen in Fig. 4.16, i.e. decreasing amplitude ratios with increasing magnetic filling.

We compare the results obtained from MHD simulations with the results obtained
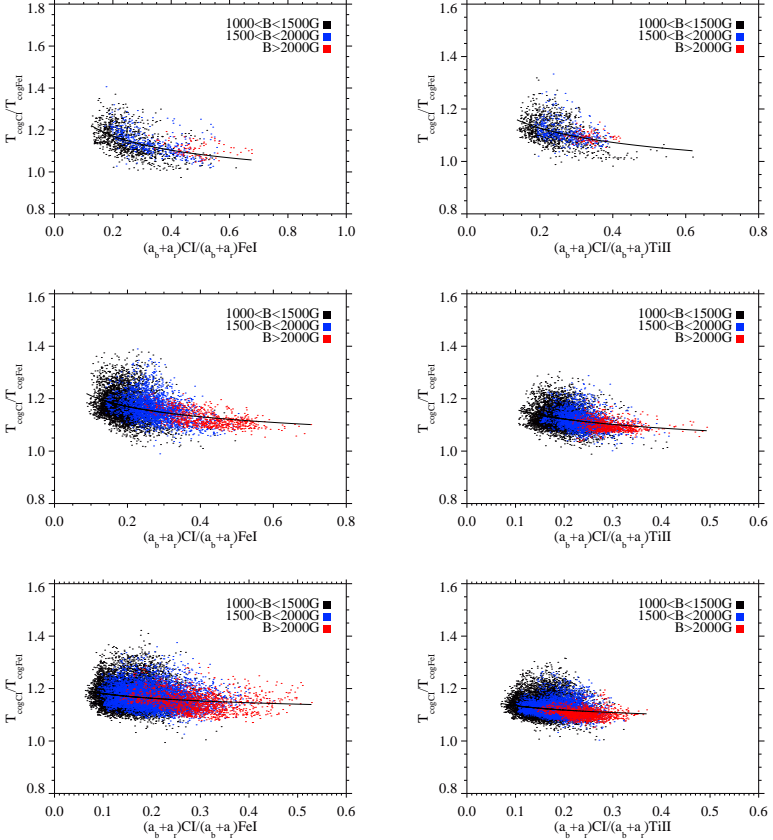
Figure 5.9: Temperatures vs the amplitude ratios in the regions with $B > 1000\,\text{G}$. Left panel represents the results for the iron line, while right panel represents the results for the titanium line. Top panel is the result from the $\langle B \rangle = 50\,\text{G}$ snapshot, middle panel is the result from the $\langle B \rangle = 200\,\text{G}$ snapshot, and bottom panel is the result from $\langle B \rangle = 400\,\text{G}$ snapshot. Solid lines represent the power law fits.

from the observations and from the inversions. In Fig. 5.14 we present the amplitude ratios of individual observations, binned data, and the degraded $\langle B \rangle$=50, 200, 400 G MHD snapshots for comparison. Here we see that the observations lie closest to the $\langle B \rangle$=200 G MURaM snapshot, which is typical of a weak plage region, consistent with Fig. 3.3 and the returned spatially averaged magnetic flux $\alpha B$, returned by the inversions (Table 4.6),

which ranges from 150 G to 305 G. Since we exclude the observed quiet sun data from the analysis, the results obtained from $\langle B \rangle$=50 G snapshot lays significantly below the extrapolation to lower Stokes $V$ amplitudes of both observation and inversion results (Fig. 5.14). The ratios obtained from the 400 G snapshot lie scattered around a curve that appears to be a reasonable extrapolation from the observed data, although the simulated ratios possibly tend to lie slightly ($\approx 0.02$) lower than the observed ones. The ratios from the 50 G snapshot appear to lie significantly below the extrapolation to lower Stokes $V$ amplitudes of the observations. New high S/N observations of quiet Sun regions are required to investigate this discrepancy.

Figure 5.10: Temperatures vs the amplitude ratios from the simulations in regions with $B > 1000\,\mathrm{G}$ at $\log \tau = 0$ from 3 snapshots. Snapshots are coded with colors and the stars represent the results from the inversions. Solid lines represent the linear fits.
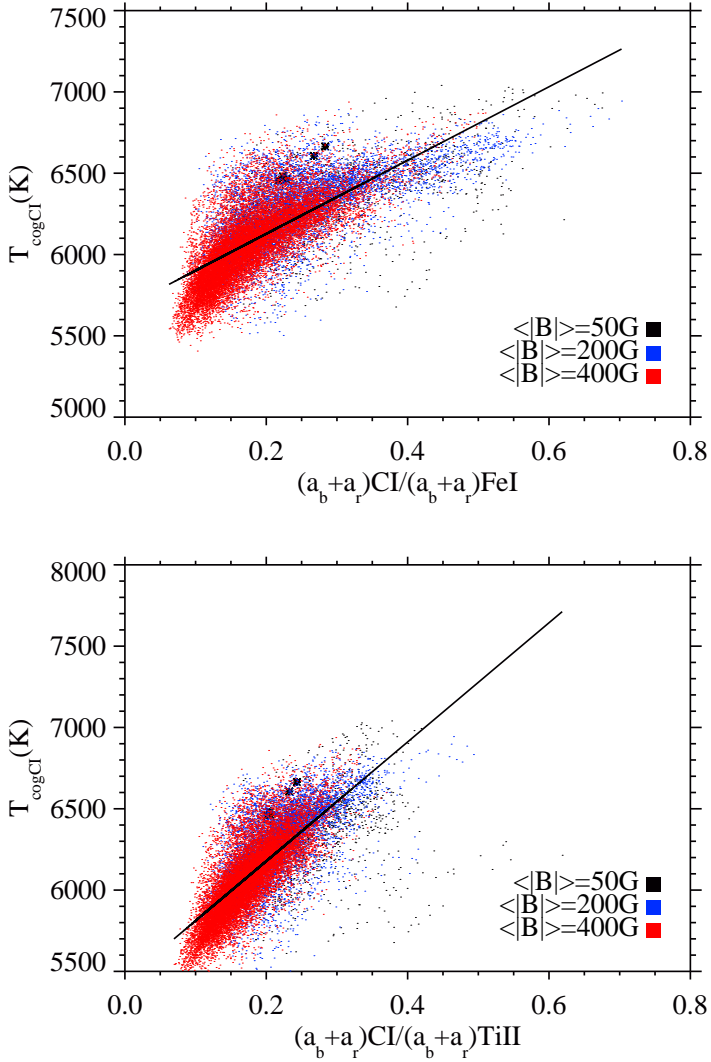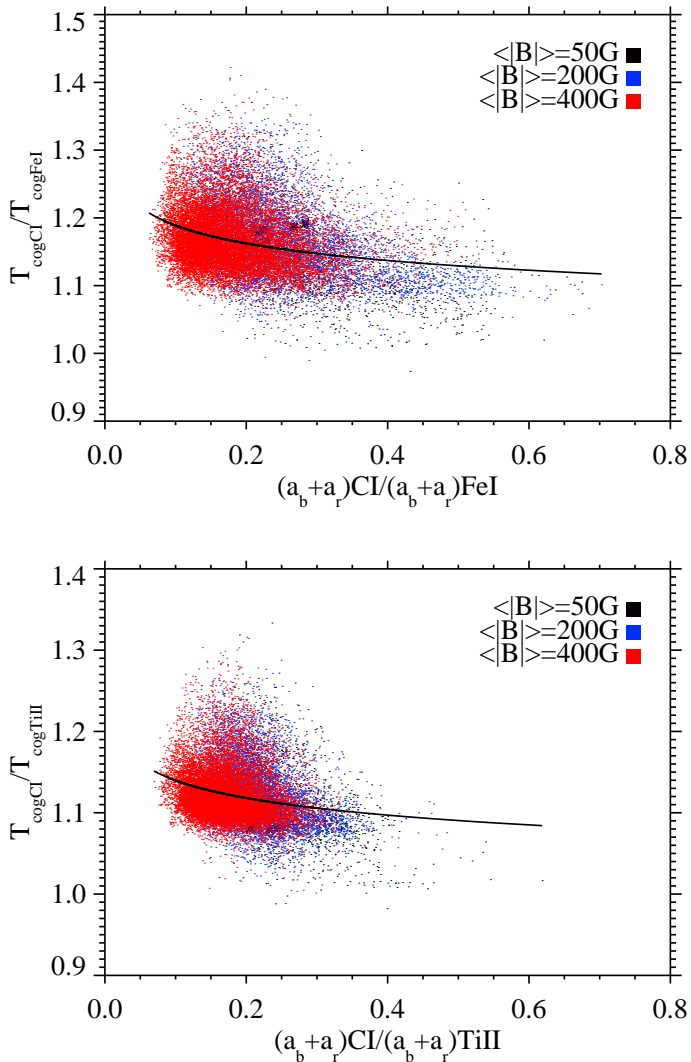
Figure 5.11: Temperature ratios vs the amplitude ratios from the simulations in the regions with $B > 1000\,\mathrm{G}$ from 3 snapshots. Snapshots are coded with colors and the stars represent the results from the inversions. Solid lines represent the power law fits.
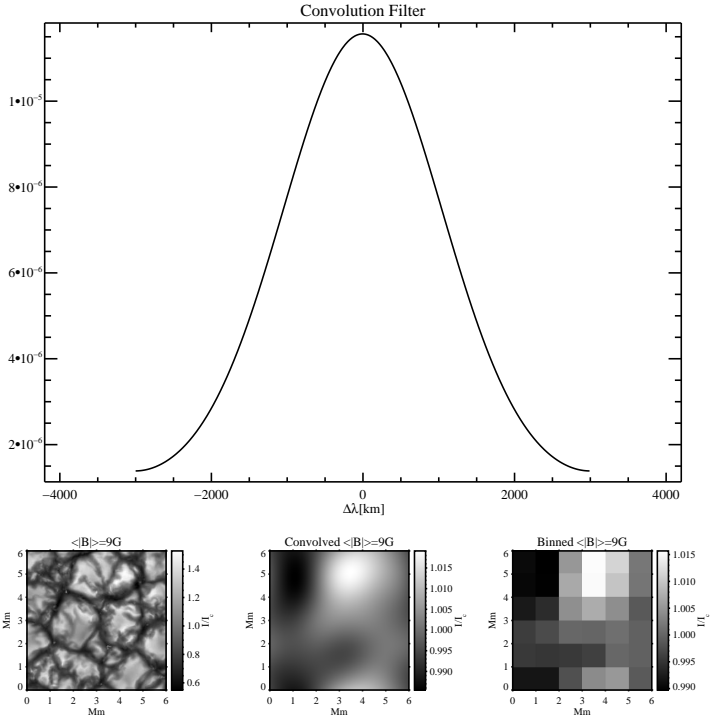
Figure 5.12: Convolution filter (top panel) and an example of a degraded snapshot. Left bottom panel represents the continuum intensity of the iron line at the $\langle |B| \rangle$=9 G snapshot with original resolution, bottom middle panel represents the convolved continuum intensity, while right bottom panel represents the binned continuum intensity.
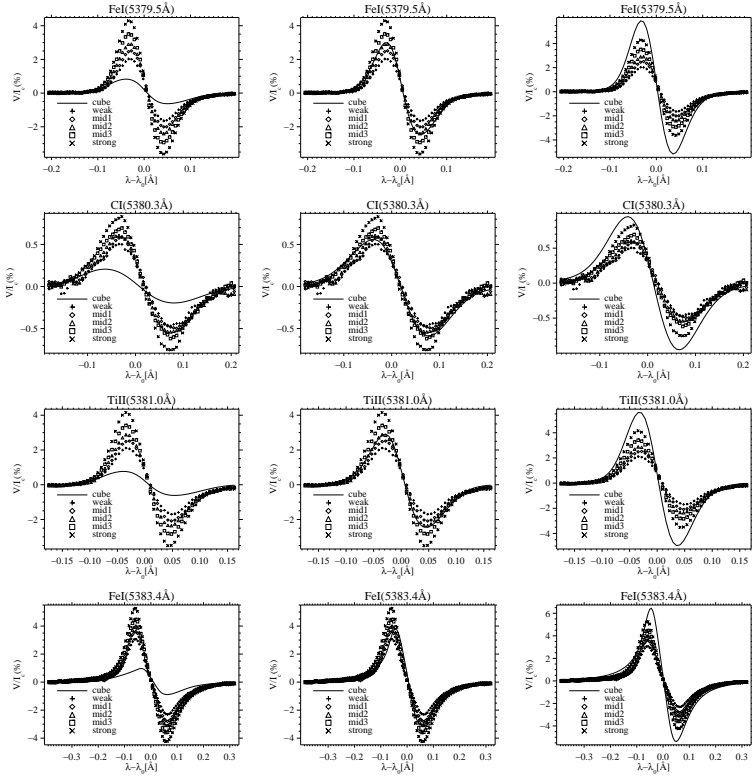
Figure 5.13: Comparison of the average Stokes *V* profiles of the snapshots with the binned profiles from the observations. Left panel represents the results of $\langle B \rangle$=50 G, mid panel represents the results of $\langle B \rangle$=200 G and the right panel represents the results of $\langle B \rangle$=400 G snapshot.
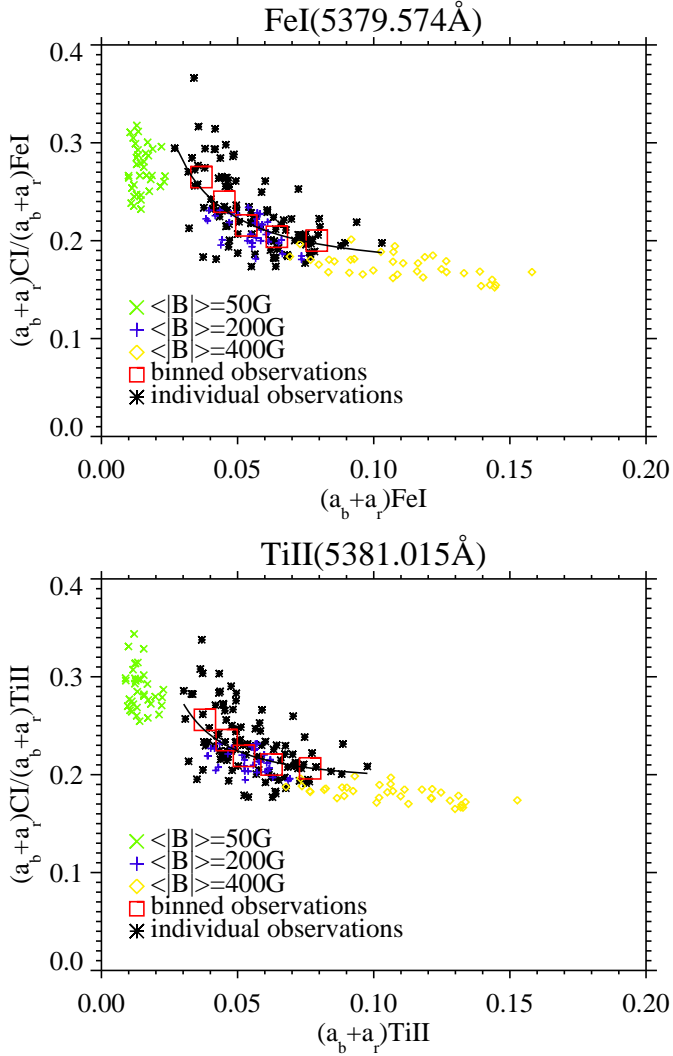
Figure 5.14: Comparison of observed Stokes *V* amplitude ratios with ratios obtained from MHD simulations. The ratio of C I to Fe I$_b$, and to Ti II is presented in the top and the bottom panel, respectively. Symbols are labeled in the frames. The solid line is a power-law fit to the individual observation data points.

# Conclusions

We present an exploratory study of Stokes $V$ amplitude ratios involving the C I 5380.3 Å line as a temperature diagnostic tool. We applied this technique to simultaneously observed Stokes $I/I_c$ and Stokes $V/I_c$ spectra of an active region. With this analysis we are able to constrain the temperature stratification around the continuum forming layers of the photospheric magnetic flux concentrations. From the inversions of the profiles binned to increase the S/N ratio, we find that the temperature of the magnetic structures at the continuum forming layers lie between roughly 6800 K for weak Stokes $V$ signals and 6600 K for signals stronger by a factor of roughly 2. These temperatures imply continuum intensity contrast values at 5380 Å in the magnetic elements of 0.07 and 0.05, respectively, which are significantly larger than the granulation contrast determined as the standard deviation of quiet Sun continuum intensity along the slit (=0.0125 for our data). The magnetic filling factor lies in the range 10-18% for these profiles.

We extended the analysis by Solanki and Brigljević (1992), who introduced the Stokes $V$ amplitude ratio involving C I Stokes $V$ profiles, by extending the technique with inversions and testing it and calibrating it using numerical simulations. We also applied it to a larger number of data points than just the 2 FTS spectra considered by them. Even with rather simple approximations in the inversions, we managed to represent our observations reasonably well. This study indicates that this temperature diagnostic tool can be used also in conjunction with spectral lines like Ti II that are not very sensitive to the temperature in the deep photosphere, although the temperature stratification cannot be reliably shown to be unique, since there may be some residual cross-talk between temperature and temperature gradient.

The decrease in ratio of the Stokes $V/I_c$ amplitude of C I 5380.3 Å relative to the other lines with increasing Stokes $V/I_c$ amplitude, i.e., increasing magnetic flux within the spatial resolution element (Fig. 4.16), confirms that the kG magnetic features in regions with lower magnetic flux are on average hotter than in regions with higher flux. Hence they are expected to appear brighter in images at continuum wavelengths or in white light. This confirms and extends the results of Solanki and Brigljević (1992) to a much larger number of data points, at somewhat higher spatial resolution.

For the first time, the amplitude ratios obtained from the MHD snapshots are compared with the results from observations and inversions. Good agreement is found (Fig. 5.14). MHD simulations also provide an independent calibration of the amplitude ratios in terms of temperature.

Bellot Rubio et al. (2000) studied a strong plage region around a sunspot with Fe I 6301.5 Å and Fe I 6302.5 Å lines with higher spatial resolution than our observations. Their results for the temperatures and velocities are similar to our results at the same heights in the atmosphere. In their model the magnetic field strength values are compa-

rable to our strong case. However, the magnetic flux in their model is significantly larger than in our models. This is not surprising since they have much higher magnetic flux (close to a sunspot) in their observed active region than the one we observed without any sunspot or pore. Even though we had lower spatial resolution then their observations and we used more simple inversions as compared to them, our results are in a good agreement.

We compared the amplitude ratios obtained from our observations with the amplitude ratios resulting from synthetic spectra computed from existing model atmospheres. We find that the PLA S86 atmosphere represents best our observations since it has a similar temperature stratification as our resulting atmospheres. The cooler PLA SB92 is representative of our mid3 and strong data sets, while the hotter NET S86 is likely to better represent regions with lower amount of magnetic flux than we have observed. This is not surprising given that it was developed to represent the network at much lower filling factor than the current data.

The work presented here makes us confident that the temperatures in the deep photospheric layers of the unresolved magnetic structures can be deduced with reasonable reliability via Stokes $V$ amplitude ratios of the selected spectral lines.

# Bibliography

Auer, L. H., Heasley, J. N., 1978, The origin of broad-band circular polarization in sunspots, A&A, 64, 67–71

Balasubramaniam, K. S., Keil, S. L., Tomczyk, S., 1997, Stokes Profile Asymmetries in Solar Active Regions, ApJ, 482, 1065–1075

Bellot Rubio, L. R., Ruiz Cobo, B., Collados, M., 1998, An Hermitian Method for the Solution of Polarized Radiative Transfer Problems, ApJ, 506, 805–817

Bellot Rubio, L. R., Ruiz Cobo, B., Collados, M., 2000, Structure of Plage Flux Tubes from the Inversion of Stokes Spectra. I. Spatially Averaged Stokes I and V Profiles, ApJ, 535, 489–500

Bianda, M., 2003, Observations of scattering polarization and the Hanle effect in the Sun's atmosphere, Ph.D. thesis, No. 15010, ETH, Zürich

Brandt, P. N., Solanki, S. K., 1990, Solar line asymmetries and the magnetic filling factor, A&A, 231, 221–234

Brault, J. W., Neckel, H., 1987, Spectral Atlas of Solar Absolute Disk Averaged and Disk Center Intensities From 3290 Å to 12510 Å

Briand, C., Solanki, S. K., 1995, Empirical models of solar magnetic elements: constraints imposed by MgI Stokes profiles., A&A, 299, 596–610

Bruls, J. H. M. J., Solanki, S. K., 1993, The chromospheric temperature rise in solar magnetic flux tubes, A&A, 273, 293–303

Chapman, G. A., 1977, Facular line profiles and facular models, ApJS, 33, 35–54

Chapman, G. A., 1979, New models of solar faculae, AJ, 232, 923–928

del Toro Iniesta, J. C., 2003, Introduction to Spectropolarimetry

Domínguez Cerdeña, I., Sánchez Almeida, J., Kneer, F., 2006, Quiet Sun Magnetic Fields from Simultaneous Inversions of Visible and Infrared Spectropolarimetric Observations, ApJ, 646, 1421–1435

Dravins, D., Lindegren, L., Nordlund, A., 1981, Solar granulation - Influence of convection on spectral line asymmetries and wavelength shifts, A&A, 96, 345–364

Elste, G., 1987, Manganese and carbon lines as temperature indicators, Sol. Phys., 107, 47–56

Fleck, B., 1991, Time-Resolved Stokes V Polarimetry of Small Scale Magnetic Structures on the Sun., in Reviews in Modern Astronomy, (Ed.) G. Klare, vol. 4 of Reviews in Modern Astronomy, pp. 90–103

Frazier, E. N., Stenflo, J. O., 1972, On the Small-Scale Structure of Solar Magnetic Fields, Sol. Phys., 27, 330–346

Fröhlich, C., 2000, Observations of Irradiance Variations, Space Science Reviews, 94, 15–24

Frutiger, C., 2000, Inversions of Zeeman Split Stokes Profiles, Ph.D. thesis, No. 13896, ETH, Zürich

Frutiger, C., Solanki, S. K., Fligge, M., Bruls, J. H. M. J., 2000, Properties of the solar granulation obtained from the inversion of low spatial resolution spectra, A&A, 358, 1109–1121

Gandorfer, A. M., Povel, H. P., 1997, First observations with a new imaging polarimeter, A&A, 328, 381–389

Gandorfer, A. M., Povel, H. P., Steiner, P., Aebersold, F., Egger, U., Feller, A., Gisler, D., Hagenbuch, S., Stenflo, J. O., 2004, Solar polarimetry in the near UV with the Zurich Imaging Polarimeter ZIMPOL II, A&A, 422, 703–708

Gingerich, O., Noyes, R. W., Kalkofen, W., Cuny, Y., 1971, The Harvard-Smithsonian reference atmosphere, Sol. Phys., 18, 347–365

Gisler, D., 2005, Instrumentierung für hochpräzise Vektorpolarimetrie in der Astronomie, Ph.D. thesis, No. 16110, ETH, Zürich

Grevesse, N., Asplund, M., Sauval, A. J., 2007, The Solar Chemical Composition, Space Science Reviews, 130, 105–114

Grossmann-Doerth, U., Larsson, B., Solanki, S. K., 1988, Contribution and response functions for Stokes line profiles formed in a magnetic field, A&A, 204, 266–274

Grossmann-Doerth, U., Schüssler, M., Solanki, S. K., 1989, Stokes V asymmetry and shift of spectral lines, A&A, 221, 338–341

Grossmann-Doerth, U., Keller, C. U., Schüssler, M., 1996, Observations of the quiet Sun's magnetic field., A&A, 315, 610–617

Gustafsson, B., 1973, Uppsala Astron. Obs. Ann., 5, 6

Hale, G. E., 1908, On the Probable Existence of a Magnetic Field in Sun-Spots, ApJ, 28, 315–343

Holweger, H., Müller, E. A., 1974, The photospheric barium spectrum - Solar abundance and collision broadening of BA II lines by hydrogen, Sol. Phys., 39, 19–30

Howard, R., Stenflo, J. O., 1972, On the Filamentary Nature of Solar Magnetic Fields, Sol. Phys., 22, 402–414

Keller, C. U., Steiner, O., Stenflo, J. O., Solanki, S. K., 1990, Structure of solar magnetic fluxtubes from the inversion of Stokes spectra at disk center, A&A, 233, 583–597

Lagg, A., Solanki, S. K., Riethmüller, T. L., Martínez Pillet, V., Schüssler, M., Hirzberger, J., Feller, A., Borrero, J. M., Schmidt, W., del Toro Iniesta, J. C., Bonet, J. A., Barthol, P., Berkefeld, T., Domingo, V., Gandorfer, A., Knölker, M., Title, A. M., 2010, Fully Resolved Quiet-Sun Magnetic flux Tube Observed with the SUNRISE/IMAX Instrument, ApJ, 723, L164–L168

Landi Degl'Innocenti, E., Landi Degl'Innocenti, M., 1977, Response functions for magnetic lines, A&A, 56, 111–115

Landi Degl'Innocenti, E., Landi Degl'Innocenti, M., 1981, Radiative transfer for polarized radiation - Symmetry properties and geometrical interpretation, Nuovo Cimento B Serie, 62, 1–16

Landi Degl'Innocenti, E., Landi Degl'Innocenti, M., 1985, On the solution of the radiative transfer equations for polarized radiation, Sol. Phys., 97, 239–250

Landi Degl'Innocenti, E., Landolfi, M., 1982, Thermodynamical properties of unresolved magnetic flux tubes. I - A diagnostic method based on circular polarization ratios in line pairs, Sol. Phys., 77, 13–26

Langangen, Ø., Carlsson, M., Rouppe van der Voort, L., Stein, R. F., 2007, Velocities Measured in Small-Scale Solar Magnetic Elements, ApJ, 655, 615–623

Lites, B. W., 2002, Characterization of Magnetic Flux in the Quiet Sun, ApJ, 573, 431–444

Livingston, W., Milkey, R., Slaughter, C., 1977, Solar luminosity variation. I - C I 5380 as a temperature indicator and a search for global oscillations, ApJ, 211, 281–287

Livingston, W., Harvey, J. W., Malanushenko, O. V., Webster, L., 2006, Sunspots with the Strongest Magnetic Fields, Sol. Phys., 239, 41–68

López Ariste, A., 2002, On the Asymmetry of Stokes Profiles, ApJ, 564, 379–384

Martínez Pillet, V., Lites, B. W., Skumanich, A., 1997, Active Region Magnetic Fields. I. Plage Fields, ApJ, 474, 810–842

Narain, U., Ulmschneider, P., 1996, Chromospheric and Coronal Heating Mechanisms II, Space Science Reviews, 75, 453–509

Povel, H., 1995, Imaging Stokes polarimetry with piezoelastic modulators and charge-coupled-device image sensors, Optical Engineering, 34, 1870–1878

Press, W. H., Teukolsky, S. A., Vetterling, W. T., Flannery, B. P., 1992, Numerical recipes in FORTRAN. The art of scientific computing

Rachkovsky, D. N., 1962, Title, Izvestiya Ordena Trudovogo Krasnogo Znameni Krymskoj Astrofizicheskoj Observatorii, 28, 259

Ralchenko, Y., Kramida, A., Reader, J., NIST ASD Team, 2008, Nist atomic spectra database (version 3.1.5), http://physics.nist.gov/asd3/

Rees, D. E., Semel, M. D., 1979, Line formation in an unresolved magnetic element - A test of the centre of gravity method, A&A, 74, 1–5

Ruiz Cobo, B., del Toro Iniesta, J. C., 1992, Inversion of Stokes profiles, AJ, 398, 375–385

Ruiz Cobo, B., del Toro Iniesta, J. C., 1994, On the sensitivity of Stokes profiles to physical quantities, A&A, 283, 129–143

Russell, H. N., Saunders, F. A., 1925, New Regularities in the Spectra of the Alkaline Earths, ApJ, 61, 38–69

Sánchez Almeida, J., Collados, M., del Toro Iniesta, J. C., 1988, An explanation for the Stokes V asymmetry in solar faculae, A&A, 201, L37–L40

Scherrer, P. H., Bogart, R. S., Bush, R. I., Hoeksema, J. T., Kosovichev, A. G., Schou, J., Rosenberg, W., Springer, L., Tarbell, T. D., Title, A., Wolfson, C. J., Zayer, I., MDI Engineering Team, 1995, The Solar Oscillations Investigation - Michelson Doppler Imager, Sol. Phys., 162, 129–188

Schüssler, M., 1983, Stellar dynamo theory, in Solar and Stellar Magnetic Fields: Origins and Coronal Effects, (Ed.) J. O. Stenflo, vol. 102 of IAU Symposium, pp. 213–234

Schüssler, M., 1986, MHD Models of Solar Photospheric Magnetic Flux Concentrations, in Small Scale Magnetic Flux Concentrations in the Solar Photosphere, (Ed.) W. Deinzer, M. Knölker, & H. H. Voigt, p. 103

Schüssler, M., 1992, Small-Scale Photospheric Magnetic Fields, in NATO ASIC Proc. 373: The Sun: A Laboratory for Astrophysics, (Ed.) J. T. Schmelz & J. C. Brown, pp. 191–220

Schwabe, M., 1844, Sonnenbeobachtungen im Jahre 1843. Von Herrn Hofrath Schwabe in Dessau, Astronomische Nachrichten, 21, 233–236

Semel, M., 1970, A Proposed Method of Calibrating Measurements of Linearly Polarized Light for the Obser- vation and Analysis of Zeeman Effects in Solar Spectral Lines, A&A, 9, 356–358

Sheeley, N. R., J., 1967, Observations of Small-Scale Solar Magnetic Fields, Sol. Phys., 1, 171–179

Sigwarth, M., Balasubramaniam, K. S., Knölker, M., Schmidt, W., 1999, Dynamics of solar magnetic elements, A&A, 349, 941–955

Solanki, S. K., 1986, Velocities in solar magnetic fluxtubes, A&A, 168, 311–329

Solanki, S. K., 1987, The Photospheric Layers of Solar Magnetic Flux Tubes, Ph.D. thesis, No. 8309, ETH, Zürich

Solanki, S. K., 1989, The origin and the diagnostic capabilities of the Stokes V asymmetry observed in solar faculae and the network, A&A, 224, 225–241

Solanki, S. K., 1990, Empirical Models of Photospheric Flux Tubes, in Solar Photosphere: Structure, Convection, and Magnetic Fields, (Ed.) J. O. Stenflo, vol. 138 of IAU Symposium, pp. 103–120

Solanki, S. K., 1993, Smallscale Solar Magnetic Fields - an Overview, Space Science Reviews, 63, 1–2

Solanki, S. K., Brigljević, V., 1992, Continuum brightness of solar magnetic elements, A&A, 262, L29–L32

Solanki, S. K., Pahlke, K. D., 1988, Can stationary velocity fields explain the Stokes V asymmetry observed in solar magnetic elements?, A&A, 201, 143–152

Solanki, S. K., Stenflo, J. O., 1984, Properties of solar magnetic fluxtubes as revealed by Fe I lines, A&A, 140, 185–198

Solanki, S. K., Stenflo, J. O., 1985, Models of solar magnetic fluxtubes - Constraints imposed by Fe I and II lines, A&A, 148, 123–132

Solanki, S. K., Stenflo, J. O., 1986, Some effects of finite spectral resolution on the Stokes V profile, A&A, 170, 120–125

Solanki, S. K., Unruh, Y. C., 1998, A model of the wavelength dependence of solar irradiance variations, A&A, 329

Solanki, S. K., Keller, C., Stenflo, J. O., 1987, Properties of solar magnetic fluxtubes from only two spectral lines, A&A, 188, 183–197

Spruit, H. C., 1974, A model of the solar convection zone, Sol. Phys., 34, 277–290

Spruit, H. C., 1976, Pressure equilibrium and energy balance of small photospheric fluxtubes, Sol. Phys., 50, 269–295

Spruit, H. C., 1979, Convective collapse of flux tubes, Sol. Phys., 61, 363–378

Spruit, H. C., Roberts, B., 1983, Magnetic flux tubes on the sun, Nature, 304, 401–406

Steiner, O., 2007, Photospheric processes and magnetic flux tubes, in Kodai School on Solar Physics, (Ed.) S. S. Hasan & D. Banerjee, vol. 919 of American Institute of Physics Conference Series, pp. 74–121

Steiner, O., Stenflo, J. O., 1990, Model Calculations of the Photospheric Layers of Solar Magnetic Fluxtubes, International Astronomical Union. Symposium no. 138, Kluwer Academic Publishers, Dordrecht, p.181

Stenflo, J. O., 1973, Magnetic-Field Structure of the Photospheric Network, Sol. Phys., 32, 41–63

Stenflo, J. O., 1975, A model of the supergranulation network and of active-region plages, Sol. Phys., 42, 79–105

Stenflo, J. O., Solanki, S., Harvey, J., Brault, J., 1984, Diagnostics of solar magnetic fluxtubes using a Fourier transform spectrometer, A&A, 131, 333–346

Stenflo, J. O., Solanki, S. K., Harvey, J. W., 1987, Center-to-limb variation of Stokes profiles and the diagnostics of solar magnetic fluxtubes, A&A, 171, 305–316

Stenflo, J. O., Keller, C. U., Povel, H. P., 1992, Demodulation of all four Stokes parameters with a single CCD - ZIMPOL II. Conceptual design., LEST Found., Tech. Rep., No. 54,, 54

Ulmschneider, P., Musielak, Z., 2003, Mechanisms of Chromospheric and Coronal Heating (Invited review), in Current Theoretical Models and Future High Resolution Solar Observations: Preparing for ATST, (Ed.) A. A. Pevtsov & H. Uitenbroek, vol. 286 of Astronomical Society of the Pacific Conference Series, pp. 363–376

Unno, W., 1956, Line Formation of a Normal Zeeman Triplet, PASJ, 8, 108–125

Unruh, Y. C., Solanki, S. K., Fligge, M., 1999, The spectral dependence of facular contrast and solar irradiance variations, A&A, 345, 635–642

Vögler, A., 2003, The Photospheric Layers of Solar Magnetic Flux Tubes, Ph.D. thesis, Universität Göttingen

Vögler, A., Schüssler, M., 2003, Studying magneto-convection by numerical simulation, Astronomische Nachrichten, 324, 399–404

Vögler, A., Shelyag, S., Schüssler, M., Cattaneo, F., Emonet, T., Linde, T., 2005, Simulations of magneto-convection in the solar photosphere. Equations, methods, and results of the MURaM code, A&A, 429, 335–351

Walton, S. R., 1987, Flux tube models of solar plages, ApJ, 312, 909–929

Willson, R. C., Hudson, H. S., 1991, The sun's luminosity over a complete solar cycle, Nature, 351, 42–44

Zakharov, V., 2006, Diagnostic of the solar photosphere with high spatial resolution using CH, CN and continuum spectral bands, Ph.D. thesis, Universität Göttingen

Zayer, I., Stenflo, J. O., Keller, C. U., Solanki, S. K., 1990, Dependence of the properties of solar magnetic flux tubes on filling factor. II - Results of an inversion approach, A&A, 239, 356–366

Zwaan, C., 1968, The structure of sunspots, ARA&A, 6, 135

# Publications

**Refereed contribution related to this work**

Oklay, N., Solanki, S. K., Lagg A., Gandorfer, A., Ramelli, R., Bianda, M., 2010, Temperature of small scale magnetic features in the deep photospheric layers, submitted to A&A.

**Conference contributions related to this work**

Oklay, N., Gandorfer, A., Solanki, S. K., 2008, Spectropolarimetric Investigations of the Deep Photospheric Layers of Magnetic Elements, 12th European Solar Physics Meeting, Freiburg, Germany, held September, 8-12, 2008. Online at http://espm.kis.unifreiburg. de/, p.2.49, 12, 2-6

Oklay, N., Gandorfer, A., Solanki, S. K., Bianda, M., Ramelli, R., 2009, Spectropolarimetric Investigations of the Deep Photospheric Layers of Solar Magnetic Structures, in Astronomical Society of the Pacific Conference Series, (Ed.) S. V. Berdyugina, K. N. Nagendra, & R. Ramelli, vol. 405 of Astronomical Society of the Pacific Conference Series, pp. 233-236

Oklay, N., Gandorfer, A., Solanki, S. K., Bianda, M., Ramelli, R., 2010, Temperatures of small scale magnetic structures in deep solar photospheric layers, 38th COSPAR Scientific Assembly Bremen, Germany, 18-25 July 2010

# Acknowledgements

First of all many thanks to my family for their full support on the each level of my studies. Canım babam ve annem, şimdiye kadar yaptığınız herşey için ne kadar teşekkür etsem az!

I thank Dieter for the unique opportunity to be part of IMPRS and for the fellowship. Thanks to Sami for the project, for his supervision and for his comments, to Achim and to Andreas for their help, for all useful discussions but also the joyful time we had, to JuanMa for his precious help with the inversions, to Franz for being my father in Germany and supporting me whenever I needed, to Manfred Schüssler for providing MURaM snapshots, to Lotfi for his introduction on how to treat MHD snapshots and all the fun we had, and to Anna the best office mate ever, and to the normal one: Robert!

Special thanks to Michele, to Renzo and to Daniel: without you, there would be no observations.

I am thankful to the Max-Planck-Institut für Sonnensystemforschung, Katlenburg-Lindau for a stipend of the International Max Planck Research School on Physical Processes in the Solar System and Beyond. The observations at IRSOL are possible thanks to the financial support that has been provided by the canton of Ticino, the city of Locarno, together with the municipalities affiliated with CISL, ETH Zurich, the Fondazione Carlo e Albina Cavargna, and the Swiss National Science Foundation (SNSF) grant 200020-117821.

At last but not least, I thank to Jean-Baptiste for his full support, care and entertainment during my PhD!

# Lebenslauf

| | |
|---:|:---|
| Name: | Nilda Oklay |
| Geburtstag und Ort: | Am 28.03.1981 in Söke/Aydın, Türkei |
| Eltern: | Nevhis Oklay<br>Ali Gürkan Oklay |
| Staatsangehörigkeit: | Türkisch |
| Schulbildung: | 1992−1999, Söke Hilmi Fırat Anatolisches Gymnasium<br>Söke/Aydın, Türkei |
| Studium: | 1999−2003<br>B.Sc. in Astronomie und Weltraumwissenschaft<br>an der İstanbul Universität<br>İstanbul, Türkei<br>Bachelorarbeit: "Sun-Earth Connection"<br><br>2001−2004<br>B.Sc. in Physik (Doppelhauptfach)<br>an der İstanbul Universität<br>İstanbul, Türkei<br><br>2003−2006<br>M.Sc. in Astronomie und Weltraumwissenschaft<br>an der İstanbul Universität<br>İstanbul, Türkei<br>Masterarbeit: "Investigation of $23^{rd}$ Solar Cycle"<br><br>Dezember 2006−Januar 2011<br>Doktorandin der International Max Planck Research School<br>on Physical Process in the Solar System and Beyond,<br>am Max-Planck-Institut für Sonnensystemforschung<br>in Katlenburg-Lindau, Deutschland |